ISSN 2518-7198 (Print)
ISSN 2663-5089 (Online)

BULLETIN

OF THE KARAGANDA UNIVERSITY

PHYSICS

Series

№ 1(109)/2023

ISSN 2663-5089 (Online)
ISSN-L 2518-7198 (Print)
Индексі 74616
Индекс 74616

ҚАРАҒАНДЫ УНИВЕРСИТЕТІНІҢ ХАБАРШЫСЫ

ВЕСТНИК КАРАГАНДИНСКОГО УНИВЕРСИТЕТА

BULLETIN OF THE KARAGANDA UNIVERSITY

ФИЗИКА сериясы

Серия ФИЗИКА

PHYSICS Series

№ 1(109)/2023

Қаңтар–ақпан–наурыз
30 наурыз 2023 ж.

Январь–февраль–март
30 марта 2023 г.

January–February–March
March, 30th, 2023

1996 жылдан бастап шығады
Издается с 1996 года
Founded in 1996

Жылына 4 рет шығады
Выходит 4 раза в год
Published 4 times a year

Қарағанды, 2023
Караганда, 2023
Karaganda, 2023

Редакцияның мекенжайы: 100024, Қазақстан, Қарағанды қ., Университет к-сі, 28
Тел.: +7 701 531 4758; факс: (7212) 35-63-98.
E-mail: vestnikku@gmail.com; karabekova71@mail.ru
Сайты: physics-vestnik.ksu.kz

Қарағанды университетінің хабаршысы. «Физика» сериясы.

ISSN-L 2518-7198 (Print). ISSN 2663-5089 (Online).

Меншік иесі: «Академик Е.А. Бөкетов атындағы Қарағанды университеті» КЕАҚ.

Қазақстан Республикасы Ақпарат және қоғамдық даму министрлігімен тіркелген. 30.09.2020 ж. № KZ38VPY00027378 қайта есепке қою туралы куәлігі.

Басуға 29.03.2023 ж. қол қойылды. Пішімі 60×84 1/8. Қағазы офсеттік. Көлемі 11,25 б.т. Таралымы 200 дана. Бағасы келісім бойынша. Тапсырыс № 24.

«Акад. Е.А. Бөкетов ат. Қарағанды ун-ті» КЕАҚ баспасының баспаханасында басылып шықты.
100024, Қазақстан, Қарағанды қ., Университет к-сі, 28. Тел. (7212) 35-63-16. E-mail: izd_kargu@mail.ru

Адрес редакции: 100024, Казахстан, г. Караганда, ул. Университетская, 28
Тел.: +7 701 531 4758. Факс: (7212) 35–63–98.
E-mail: vestnikku@gmail.com; karabekova71@mail.ru
Сайт: physics-vestnik.ksu.kz

Вестник Карагандинского университета. Серия «Физика».
ISSN-L 2518-7198 (Print). ISSN 2663-5089 (Online).

Собственник: НАО «Карагандинский университет имени академика Е.А. Букетова».

Зарегистрирован Министерством информации и общественного развития Республики Казахстан. Свидетельство о постановке на переучет № KZ38VPY00027378 от 30.09.2020 г.

Подписано в печать 29.03.2023 г. Формат 60×84 1/8. Бумага офсетная. Объем 11,25 п.л. Тираж 200 экз. Цена договорная. Заказ № 24.

Отпечатано в типографии издательства НАО «Карагандинский университет им. акад. Е.А. Букетова». 100024, Казахстан, г. Караганда, ул. Университетская, 28. Тел. (7212) 35-63-16. E-mail: izd_kargu@mail.ru

Postal address: 28, Universitetskaya Str., 100024, Karaganda, Kazakhstan

Tel.: +7 701 531 4758; Fax: (7212) 35-63-98.
E-mail: vestnikku@gmail.com; karabekova71@mail.ru
Web-site: physics-vestnik.ksu.kz

Executive Editor

PhD **G.B. Sarzhanova**

Editors

Zh.T. Nurmukhanova, S.S. Balkeyeva, I.N. Murtazina

Computer layout

M.S. Babatayeva

Bulletin of the Karaganda University. "Physics" Series.

ISSN-L 2518-7198 (Print). ISSN 2663-5089 (Online).

Proprietary: NLC "Karagandy University of the name of academician E.A. Buketov".

Registered by the Ministry of Information and Social Development of the Republic of Kazakhstan. Rediscount certificate No. KZ38VPY00027378 dated 30.09.2020.

Signed in print 29.03.2023. Format 60×84 1/8. Offset paper. Volume 11,25 p.sh. Circulation 200 copies. Price upon request. Order № 24.

Printed in the Publishing house of NLC "Karagandy University of the name of acad. E.A. Buketov".
28, University Str., Karaganda, 100024, Kazakhstan. Tel. (7212) 35-63-16. E-mail: izd_kargu@mail.ru

МАЗМҰНЫ — СОДЕРЖАНИЕ — CONTENT

КОНДЕНСАЦИЯЛАНҒАН КҮЙДІҢ ФИЗИКАСЫ
ФИЗИКА КОНДЕНСИРОВАННОГО СОСТОЯНИЯ
PHYSICS OF THE CONDENSED MATTER

Alikhaidarova E., Seliverstova E., Ibrayev N. Effect of Silver Nanoparticles on the Optoelectronic Properties of Graphene Oxide Films 6

Rozhkova X.S., Aimukhanov A.K., Ilyassov B.R., Tussupbekova A.K., Zeinidenov A.K., Alexeev A.M., Zhakanova A.M. Effect of WS_2 nanoparticles on the current-voltage characteristics of a polymer solar cell 13

ТЕХНИКАЛЫҚ ФИЗИКА
ТЕХНИЧЕСКАЯ ФИЗИКА
TECHNICAL PHYSICS

Tleukenov S.K., Suierkulova Zh.N., Nurkenov S.A. Indicatrix of TE and TM-polarized wave velocities in crystal of classes 4mm, 3m, 6mm with magneto-electric effect 23

Katsyv S., Kukharchuk V., Kucheruk V., Kulakov P., Gribov M. Nonstandard analysis in electrical engineering. The analysis of the direct current circles with ideal reactive elements.................................. 31

Tleubergenova A.Zh., Tanasheva N.K., Shaimerdenova K.M., Botpaev N.K., Minkov L.L., Kassiyev S.B. Investigation of aerodynamic characteristics of a two-bladed sailing wind turbine 42

ЖЫЛУФИЗИКАСЫ ЖӘНЕ ТЕОРИЯЛЫҚ ЖЫЛУТЕХНИКАСЫ
ТЕПЛОФИЗИКА И ТЕОРЕТИЧЕСКАЯ ТЕПЛОТЕХНИКА
THERMOPHYSICS AND THEORETICAL THERMOENGINEERING

Kossov V.N., Krasikov S.A., Belov S.M., Fedorenko O.V., Zhaneli M. Comparative study of evolution of structured flows at boundary of the regime change “diffusion – concentration convection” in isothermal multicomponent mixing in gases by techniques of visual and numerical analysis..................... 49

Kurmanova D.Y., Jaichibekov N.Zh., Karpenko A.G., Volkov K.N. Numerical modeling and calculation of heat transfer between heat carriers in heat exchangers.. 59

Goldsteyn A.E., Abakumov Kh.Kh. Mitigation of the effect of variations in the electrical conductivity of the material via two-frequency eddy current testing of the thickness of the electrically conductive wall under significantly varying influence parameters.. 71

Kissabekova P.A., Karabekova D.Zh., Khassenov A.K., Kucheruk V.Yu., Kudussov A.S., Kyzdarbekova Sh.S. Theoretical foundations of the construction of the operation of heat flow devices..... 80

АВТОРЛАР ТУРАЛЫ МӘЛІМЕТТЕР — СВЕДЕНИЯ ОБ АВТОРАХ — INFORMATION ABOUT AUTHORS 88

DOI 10.31489/2023PH1/6-12

UDC 538.958, 541.143

E. Alikhaidarova*, E. Seliverstova, N. Ibrayev

Institute of Molecular Nanophotonics, Karaganda University of the name of academician E.A. Buketov, Karaganda, Kazakhstan
*(*E-mail: alikhaidarova@mail.ru)*

Effect of Silver Nanoparticles on the Optoelectronic Properties of Graphene Oxide Films

The effect of Ag nanoparticles (NPs) on the optical and optoelectronic properties of films based on graphene oxide has been studied. In the presence of Ag NPs, the morphology, as well as the thickness of graphene oxide films, were not changed. When Ag NPs were added, a change in the shape and position of the absorption bands and Raman spectra of graphene oxide was observed. It is shown that with the addition of Ag NPs, the G band of graphene oxide shifts to low frequencies, which may be the result of the absence of separate double bonds, while the I_D/I_G ratio was not changed, as did the number of Gr layers. In the absorption spectrum of the films, along with the absorption band of graphene oxide, a shoulder was registered, which can be associated with the absorption of Ag NPs. The optical density of Gr films with plasmonic NPs is higher than without them. Measurements of the optoelectronic characteristics showed that, in the presence of Ag NPs, an increase in the values of the photocurrent of graphene oxide is observed. The sensitivity of graphene oxide films was increased by almost 20 times when plasmonic NPs were added to them, and the detection ability increased by 25 times. The results obtained can be used in the development of new photosensitive devices for optoelectronic and photocatalytic applications.

Keywords: graphene oxide, silver nanoparticles, plasmon, properties, absorption, Raman spectra, optoelectronic properties, photodetectors.

Introduction

Graphene is one of the most widely used ultrathin two-dimensional materials that have had a huge impact on supercapacitors, biosensors [1] and is used in the development of optoelectronics [2], photovoltaics [3], and photocatalysis [4] devices. Graphene with surface oxygen-containing groups is called graphene oxide. Graphene oxide and its modifications, in contrast to graphene, are a more convenient material for researchers, since it is easy to obtain and use for practical purposes. Graphene oxide (GO) is rich in oxygen-containing functional groups such as carboxyl, hydroxyl, epoxy and carbonyl on its surface and edges compared to graphene, which improves solubility and provides many reactive sites for further functioning [5, 6]. Meanwhile, graphene oxide saves the characteristics of graphene. Thus, graphene oxide has great potential for applications [7].

In recent years, long-range photodetectors have attracted wide interest due to their large civilian and military applications, including biological and chemical analysis, environmental monitoring, remote control, and missile launch detection [8, 9]. Ultraviolet photodetectors are usually made from wide-gap semiconductor materials or from graphene nanostructures. Photodetectors based on graphene have a number of advantages, such as better efficiency of charge-transport processes and low cost [10, 11, 12]. However, photovoltaic devices based on graphene and graphene oxide has limitation lies in their low sensitivity.

The introduction of plasmonic silver nanoparticles into graphene layers will make it possible to overcome this limitation. It is known that the inclusion of metallic nanostructures in graphene enhances the light–substance interaction [13]. Recently, plasmonic nanostructures have been used for surface enhanced Raman spectroscopy (SERS), single molecule spectroscopy, improved photodetection, photovoltaics, and light emitting devices. Near-field enhancement of the photoconversion efficiency in graphene was demonstrated by placing Au nanostructures on the surface of a graphene sheet [13]. This approach has also been reported to provide better spectral sensitivity, which enables multicolor photodetection [14].

The amplification of the photocurrent in graphene-Ag hybrid devices is the result of the amplification of graphene electronic vibrations in the near field, as well as the scattering effect of Ag nanoparticles [15]. In addition, scattering from Ag NPs can also play a vital role in increasing the photocurrent, which is similar to the plasmon enhancement effect observed in a nanoantenna-based optical photodetector [16]. The results of the review clearly demonstrate that Ag nanoparticles embedded in graphene with several layers can be an active material to improve the interaction of light and matter. Thus, new hybrid 2D plasmonic nanostructures may be very attractive for future graphene-based optoelectronic devices.

In this work, the effect of silver nanoparticles on the optoelectronic properties of graphene oxide films prepared by the method of airbrush spraying was studied. This method makes it possible to obtain graphene films of a larger area with less time spent, which can be used in practical applications.

Experimental

To obtain films, single layer graphene oxide (SLGO, Cheaptubes) was dispersed in deionized water in an ultrasonic bath for 30 minutes. The Gr concentration in solutions was equal to 2 mg/mL. To remove large particles, the dispersions were centrifuged at 3000 rpm.

Ag nanoparticles (NPs) were synthesized by laser ablation using a Nd: YAG laser with λ_{gen}=532 nm, τ_{pulse}=10 ns, and E_{pulse}~16 J/cm^2 [17]. The ablation time was equal to 10 minutes. The height of the ablated liquid was equal to 0.8 cm. The average NPs diameter determined by dynamic light scattering (Nanosizer S90, Malvern) was equal to 18±5 nm. NPs were added to the prepared dispersion of graphene oxide at a concentration of 10^{-12} mol/L.

The films were deposited with a graphic airbrush with a nozzle diameter of 0.9 mm. The distance from the airbrush to the substrate surface was equal to 15.5 cm. The thickness of the films was 25 layers. The resulting films were dried at 80 °C in a drying oven for at least 3 hours to completely remove the solvent. In the study of optoelectronic properties, FTO coated glasses (fluorine-doped tin oxide, ~7 Ω/sq, Sigma-Aldrich) were used.

The structural and morphological properties of the prepared films were studied using a Mira 3 LMU (Tescan) scanning electron microscope (SEM).

Absorption spectra were measured using a Cary 300 spectrometer (Agilent). The Raman spectra were recorded using a Confotec MR520 microscope (Sol Instruments) with laser excitation at a wavelength of 632.8 nm.

Measurements of the current-voltage characteristics (CVC) of the prepared samples were carried out using an Elins P-20X (Elins) potentiostat-galvanostat when the samples were irradiated with Xe lamp with 35 mW/cm^2.

FTO glasses were used to assemble the photodetector. On the surface of the substrates, interdigitated tracks were cut out using a BLS0503MM (Bodor) laser scribing machine. The distance between the tracks is 1.5 mm, the length of the tracks is 10 mm. The view of the photodetector can be found in [18].

Results and Discussion

The study of the structure on SEM (Tescan Mira-3) showed that when Gr is deposited, an islet film is formed (Fig. 1).

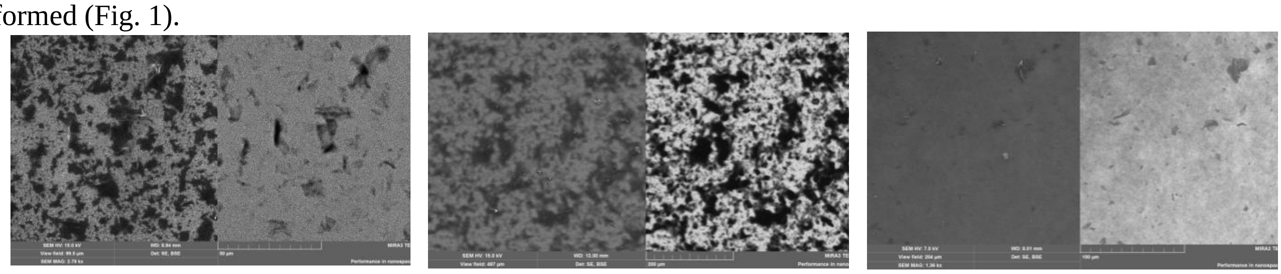

5 layers 10 layers 20 layers

Figure 1. SEM images of Gr films obtained by airbrushing

In this case, the image clearly shows multilayer particles located on the periphery of the sprayed film. With an increase in the number of sprayed layers, the film occupies a larger area and is more uniform. The SEM images (right) recorded with a reflected electron detector (BSE) show that as the number of layers increases the number of multilayer particles also grow. The structure of Gr+Ag NPs films does not differ from that for films with graphene oxide due to the fact that the concentration of plasmon NPs in them is too low.

To study the optical properties of the prepared films, the spectra shown in Figure 2 were obtained. A band with a maximum at about 230 nm is observed in the absorption spectrum of the films. It is known that the absorption band at 230 nm is formed by transitions between $\pi\pi^*$–nature orbitals in aromatic C–C bonds [18, 19]. The addition of silver NPs did not practically change the optical density at the maximum. A shoulder that is observed at 350 nm, can be associated with the absorption of Ag NPs. The maximum absorption spectrum of plasmonic NPs exhibits at 400 nm. In the wavelength range from 350 to 600 nm, the optical density of Gr films with plasmon NPs is higher than without them.

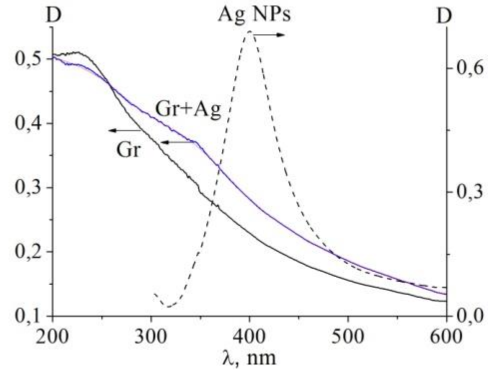

Figure 2. Absorption spectra of Gr films deposited by airbrushing with the addition of Ag NPs

The plasmonic effect of Ag NPs also leads to an increase in the intensity of Raman scattering of Gr films (Fig. 3). In the Raman spectra of Gr film, the G band exhibits at 1595–1605 cm^{-1} and it is shifted to higher frequencies compared to the position of this band (1581 cm^{-1}) in graphite [20].

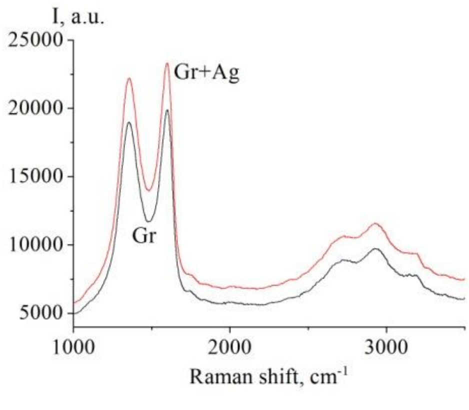

Figure 3. Raman spectra of Gr films deposited by airbrushing with the addition of Ag NPs

The Raman spectrum of Gr films also contains a D band at about 1360 cm^{-1}, which characterizes the degree of defectiveness, and a 2D band in the region of about 2700–2900 cm^{-1} is clearly distinguishable, which indicates the possible presence of disordered regions in the structure of the synthesized Gr films. As can be seen from the data (Table 1), with the addition of Ag NPs, the G-band of graphene oxide shifts to the low-frequency region, which may be the result of the absence of individual double bonds that resonate at higher frequencies [21]. At the same time, the I_D/I_G ratio did not change, as the number of Gr layers, which can be obtained from the I_{2D}/I_G value [21]. However, the value of this parameter indicates that the number of layers in Gr in the films under study varies from 4 to 8.

Table 1

Position and intensity of Raman bands of Gr films with Ag NPs

Sample	D, cm^{-1}	I, a.u.	G, cm^{-1}	I, a.u.	I_D/I_G	2D, cm^{-1}	I, a.u.	I_{2D}/I_G
Gr	1350	18940	1600	19923	0.95	2733	8910	0.45
Gr +Ag	1355	22203	1598	23346	0.95	2740	10588	0.45

The optoelectronic properties of graphene oxide films were studied by measuring the current-voltage characteristics (CVC) of the films under study, as well as by determining the photocurrent I_{ph}, sensitivity R, and detectivity D* of the obtained films according to the procedure of [18].

The current-voltage characteristics of the prepared samples were measured both at a positive voltage bias (up to +30 V) and at negative values — up to -30 V. The I(U) dependence curves have a non-linear shape. In this case, even in the absence of illumination of the samples, currents are recorded. The values of the generated photocurrent I_{ph} of the detector, shown in Table 2, were estimated from the difference between the dark and light values of I.

The maximum photocurrent value recorded for graphene oxide without plasmonic NPs is equal to 10 nA (at +25 V), while at a reverse polarity voltage it is only 0.048 nA. The I_{ph} values for films based on Gr+Ag NPs are almost 20 times higher. It can be seen that both dark and light currents increased almost proportionally (Fig. 4).

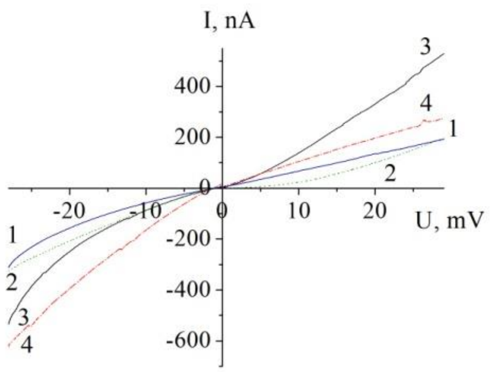

Figure 4. I — V characteristics of Gr films without (1, 2) and with Ag NPs (3, 4): 1.3 — light; 2.4 — dark curves

Table 2

Optoelectronic parameters of Gr-based films

Sample	I_{ph}, nA at + 25 V	I_{ph}, μA at –25 V	R, A/W	D*, Jones
Gr	10	0.048	$2.86·10^{-7}$	$0.12·10^{7}$
Gr+Ag	196	0.120	$56·10^{-7}$	$3.01·10^{7}$

When evaluating the responsivity R of the prepared films, the formula R = I_{ph}/P was used, where P is the power of the incident light. From Table 2, it can be seen that the responsivity of graphene oxide films increased significantly (almost 20 times) with the addition of plasmon NPs to them.

Further, the specific detectivity D* of the prepared samples was estimated, which determines the ability of the device to detect weak light signals and can be determined from expression (1) [22, 23]:

$$D^* = \frac{RA^{1/2}}{\sqrt{2*e*I_{dark}}}, \quad (1)$$

where R is the responsivity of the films, A is the illuminated area of the sample, e is the modulus of the electron charge, Idark is the value of the dark current at +25 V.

Calculations showed that the specific detectivity of Gr films is equal to $1.2·10^6$ Jones, while in the presence of silver NPs D* increased 25 times and is equal to $3.01·10^7$ Jones. It can be explained by the fact that, for pure Gr films, the value of the calculated sensitivity of the films is almost the same time smaller.

Comparing the results obtained with other authors, it can be noted that values of the R and D* parameters for pure Gr films are very small and differ by an order of magnitude from the values of [23, 24], where graphene oxide was used to prepare photodetectors. However, it can be noted that, in this work, graphene oxide films were deposited by dip-coating and were subjected to further high-temperature annealing, which, as is known from our studies [25], leads to partial reduction of graphene oxide and removal of oxygen-containing groups. As a result, the charge-transport characteristics of graphene oxide films also increase. However, the optoelectronic characteristics of graphene oxide films can be increased due to the plasmon effect of Ag NPs. Moreover, their value is comparable to the values obtained by other groups for both Gr and pure graphene [23]. The enhancement of the photocurrent can be explained both by the enhancement of the electric field near Ag NPs [26], [27] and by the scattering of light by silver NPs. This field can increase the absorption of the Gr films in the visible region of the spectrum [27].

Conclusions

Films based on graphene oxide and plasmonic NPs have been synthesized. It is shown that in the presence of Ag NPs, the morphology, as well as the thickness of graphene oxide films, does not change. When Ag NPs were added, a change in the shape and position of the absorption bands and Raman spectra of graphene oxide was observed. In particular, with the addition of Ag NPs, the G band of graphene oxide is shifted to low frequencies, which may be the result of the absence of individual double bonds. At the same time, the I_D/I_G ratio did not change, as did the number of Gr layers. In the absorption spectrum of the films, along with the absorption band of graphene oxide, a shoulder was registered, which can be associated with the absorption of Ag NPs. The optical density of Gr films with plasmonic NPs is higher than without them.

Measurements of the optoelectronic characteristics showed that, in the presence of Ag NPs, an increase in the values of the photocurrent of graphene oxide is observed. The sensitivity of graphene oxide films increased by almost 20 times when plasmonic NPs were added to them. The detectivity of Gr films is equal to $1.2 \cdot 10^6$ Jones, whereas in the presence of LPR silver NPs D* increased by 25 times and is equal to $3.01 \cdot 10^7$ Jones. The enhancement of the photocurrent can be explained both by the enhancement of the electric field near the Ag NPs and by the scattering of light by silver NPs.

The results obtained can be used in the development of new photosensitive devices for optoelectronic and photocatalytic applications.

Acknowledgements

This research is funded by the Science Committee of the Ministry of Education and Science of the Republic of Kazakhstan (Grant No. AP09259913).

References

1 Tan, C., Cao, X., Wu, X. -J., He, Q., Yang, J., Zhang, X., Chen, J., Zhao, W., Han, S., Nam, G.H. et al. (2017). Recent Advances in Ultrathin Two-Dimensional Nanomaterials. *Chem. Rev*. 117, 6225–6331. doi:10.1021/acs.chemrev.6b00558.

2 Mahmoudi, T., Wang, Y., & Hahn, Y.B. (2018). Graphene and its derivatives for solar cells application. *Nano Energy.* 47, 51–65.

3 Zhumabekov, A.Z., Ibrayev, N.K., & Seliverstova, E.V. (2020). Photoelectric properties of a nanocomposite derived from reduced graphene oxide and TiO_2. *Theor. Exp. Chem*. 55(6), 398–406.

4 Paredes, J.I., Villar, R.S., Solis, F.P., Martinez, A.A., & Tascon, J.M. (2009). Atomic force and scanning tunneling microscopy imaging of graphene nanosheets derived from graphite oxid. *Langmuir*. 25, 5957–5968.

5 Guo, S., Nishina, Y., Bianco, A., & Menard-Moyon, C. (2020). A Flexible Method for Covalent Double Functionalization of Graphene Oxide. *Angew. Chem.* Int. Ed. Engl. 59, 1542–1547. doi: 10.1002/anie.201913461.

6 Shu, D., Li, Y., Liu, A., Zhang, H., & Zhou, Y. (2020). Facile Route to Preparation of Positively Charged GO Using Poly (Diallyldimethylammoniumchloride). Fuller. Nanotub. Carbon Nanostruct. 28, 394–401. doi: 10.1080/1536383X.2019.1690471.

7 Wang, Y., Chen, Y., Lacey, S.D., Xu, L., Xie, H., Li, T., Danner, V.A., & Hu, L. (2018). Reduced Graphene Oxide Film with Record-High Conductivity and Mobility. Mater. Today. 21, 186–192. DOI: 10.1016/j.mattod.2017.10.008.

8 Yu, X., Zhao, Z., Zhang, J., Guo, W., Qiu, J., Li, D., Li, Z., Mou, X., Li, L., Li, A., & Liu, H. (2016). Rutile nanorod/anatase nanowire junction array as both sensor and power supplier for high-performance, self-Powered, wireless UV photodetector. *Small.* 12(20), 2759–2767.

9 Peng, M., Liu, Y., Yu, A., Zhang, Y., Liu, C., Liu, J., Wu, W., Zhang, K., Shi, X., Kou, J., Zhai, J., & Wang, Z.L. (2016). Flexible self-powered GaN ultraviolet photoswitch with piezo-phototronic effect enhanced on/off ratio. *ACS Nano.* 10(1), 1572–1579.

10 Cakmakyapan, S., Lu, P.K., Navabi, A. *et al.* (2018). Gold-patched graphene nano-stripes for high-responsivity and ultrafast photodetection from the visible to infrared regime. *Light Sci Appl*. **7**, 20. doi.org/10.1038/s41377-018-0020-2.

11 Schuler, S., Muench, J.E., Ruocco, A. *et al.* (2021). High-responsivity graphene photodetectors integrated on silicon microring resonators. *Nat Commun.* 12, 3733. doi.org/10.1038/s41467-021-23436-x.

12 Jiang, H., Wei, J., Sun, F., Nie, Ch., Fu, J., Shi, H., Sun, J., Wei, X., & Cheng-Wei Qiu, Ch.W. (2022). Enhanced Photogating Effect in Graphene Photodetectors via Potential Fluctuation Engineering. *ACS Nano.* 16, 3, 4458–4466. doi.org/10.1021/acsnano.1c10795.

13 Ozbay, E. (2006) Merging photonics and electronics at nanoscale dimensions. *Science.* 311(5758), 189.

14 Liu, W.L., Lin, F.C., Yang, Y.C., Huang, C.H., Gwo, S., Huang, M.H., & Huang, J. (2013). The influence of shell thickness of Au@TiO2 core–shell nanoparticles on the plasmonic enhancement effect in dyesensitized solar cells. *Nanoscale*. 5, 7953.

15 Liu, Y., Cheng, R., Liao, L., Zhou, H., Bai, J., Liu, G., Liu, L., Huang, Y., & Duan, X.F. (2011). Plasmon resonance enhanced multicolour photodetection by graphene. Nat Commun. 2, 579.

16 Lee, J.-H., Kim, I.K., Cho, D., You, J.I., Kim, Y.J., & Oh, H.-J. (2015). Photocatalytic performance of graphene/Ag/TiO_2 hybrid nanocomposites. *Carbon Letters*.16, 4, 247-254.

17 Ibrayev, N., Seliverstova, E., Temirbayeva, D., & Ishchenko, A. (2022). Plasmon effect on simultaneous singlet-singlet and triplet-singlet energy transfer. *Journal of Luminescence*. *251*, 119203. doi:10.1016/j.jlumin.2022.119203.

18 Seliverstova, E.V., Ibrayev, N.K., & Zhumabekov, A.Z. (2020). The effect of silver nanoparticles on the photodetecting properties of the TiO_2/graphene oxide nanocomposite. *Opt. Spectrosc*. 128, (9), 1449–1457.

19 Sutar, D.S., Narayanam, P.K., Singh, G., Botcha, V.D., Talwar, S.S., Srinivasa, R.S., & Major, S.S. (2012). Spectroscopic studies of large sheets of graphene oxide and reduced graphene oxide monolayers prepared by Langmuir–Blodgett technique. *Thin Solid Films*, 520(18), 5991–5996. doi:10.1016/j.tsf.2012.05.018.

20 Jorio, A., Dresselhans, M., Saito, R., & Dresselhaus, G.F. (2011). Raman spectroscopy in graphene related system. Verlag: Wiley–VCH, 356.

21 Paredes, J.I., Villar, R.S., Solis, F.P., Martinez, A.A., & Tascon, J.M. (2009). Atomic force and scanning tunneling microscopy imaging of graphene nanosheets derived from graphite oxid. *Langmuir.* 25, 5957–5968.

22 Li, Sh., Tao, D., Zhang, Ya., Yuning, L., Weijie, Y., Chen, Q., & Zewen, L. (2019). Solar–blind ultraviolet detection based on TiO_2 nanoparticles decorated graphene field–effect transistors. *Nanophotonics*. 8 (5), 899–908.

23 De, Sanctis A., Mehew, J.D., Craciun, M.F., & Russo, S. (2018). Graphene–based light sensing: fabrication, characterization, physical properties and performance. *Mater.* 11(9) 1762–1791.

24 Lai, S.K., Tang, L., Hui, Y.Y., Luk, C.M., & Lau, S.P. (2014). A deep ultraviolet to near–infrared photoresponse from glucose–derived graphene oxide. *J. Mater. Chem*. 2(34), 6971–6977.

25 Seliverstova, E., Ibrayev, N., Dzhanabekova, R., & Gladkova, V. (2017). The effect of temperature on the properties of grapheme oxide langmuir films. *IOP Conf. Ser.: Mat. Sc. and Engin*. 168(1), 012102.

26 Maiti, R., Sinha, T.K., Mukherjee, S., Adhikari, B., & Ray, S.K. (2016). Enhanced and selective photodetection using graphene–stabilized hybrid plasmonic silver nanoparticles. *Plasmonics*. 11(5), 1297–1304.

27 Liu, Y., Cheng, R., Liao, L., Zhou, H., Bai, J., Liu, G., & Duan, X. (2011). Plasmon resonance enhanced multicolour photodetection by grapheme. *Nat. Commun*. 2(1), 1–7.

Э. Алихайдарова, Е. Селиверстова, Н. Ибраев

Күміс нанобөлшектерінің графен оксиді пленкаларының оптоэлектрондық қасиеттеріне әсері

Ag нанобөлшектерінің (НБ) графен оксиді негізіндегі пленкаларының оптикалық және оптоэлектрондық қасиеттеріне әсері зерттелді. Графен оксиді құрамында Ag НБ бар пленкаларының морфологиясы мен қалыңдығы өзгермейді. Ag НБ қосқанда графен оксидінің Раман-спектрлерінің пішіні мен жұтылу жолақтарының өзгерісі байқалады. Ag НБ-нің қосылған кезде графен оксидінің G-жолағы төмен жиіліктерге ауысатыны көрсетілген, бұл жеке қос байланыстың болмауының нәтижесінде болуы мүмкін, ал Gr қабаттарының санымен қоса I_D/I_G қатынасы да өзгермеген. Пленкалардың жұтылу спектрінде графен оксидінің жұтылу спектрлерімен қатар, Ag НБ-нің жұтылуына байланысты болуы мүмкін иін тіркелді. Gr пленкаларының оптикалық тығыздығы плазмондық НБ қоспағанға қарағанда жоғары болды. Оптоэлектрондық сипаттамаларды өлшеу кезінде Ag НБ қосылған графен оксидінің фототок мәндерінің жоғарылауы байқалатынын көрсетті. Графен оксиді пленкаларының сезімталдығы оларға плазмондық НБ қосылған кезде 20 есе, ал детекторлық қабілеті 25 есе өсті. Алынған нәтижелерді оптоэлектронды және фотокаталитикалық қосымшалар үшін жаңа жарыққасезімтал жаңа құрылғыларды жасауда пайдалануға болады.

Кілт сөздер: графен оксиді, күміс нанобөлшектері, плазмон, қасиеттері, жұтылу, КШ спектрлері, оптоэлектрондық қасиеттер, фотодетекторлар.

Э. Алихайдарова, Е. Селиверстова, Н. Ибраев

Влияние наночастиц серебра на оптоэлектронные свойства пленок оксида графена

Изучено влияние наночастиц (НЧ) Ag на оптические и оптоэлектронные свойства пленок на основе оксида графена. В присутствии НЧ Ag морфология, как и толщина пленок оксида графена, не изменяется. При добавлении НЧ Ag наблюдается изменение формы и положения полос поглощения и Раман-спектров оксида графена. Показано, что с добавлением НЧ Ag G-полоса оксида графена сдвигается в область низких частот, что может быть результатом отсутствия отдельных двойных связей, при этом соотношение I_D/I_G не изменилось, как и количество слоев Gr. В спектре поглощения пленок, наряду с полосой поглощения оксида графена, зарегистрировано плечо, которое может быть ассоциировано с поглощением НЧ Ag. Оптическая плотность пленок Gr с плазмонными НЧ выше, чем без них. Измерения оптоэлектронных характеристик показали, что в присутствии НЧ Ag наблюдается рост значений фототока оксида графена. Чувствительность пленок оксида графена увеличилась почти в 20 раз при добавлении в них плазмонных НЧ, а детектирующая способность — в 25 раз. Полученные результаты могут быть использованы при разработке новых светочувствительных устройств для оптоэлектронных и фотокаталитических приложений.

Ключевые слова: оксид графена, наночастицы серебра, плазмон, свойства, поглощение, спектры КР, оптоэлектронные свойства, фотодетекторы.

DOI 10.31489/2023PH1/13-22

UDC 535.215; 535.3; 539.23

X.S. Rozhkova[1]*, A.K. Aimukhanov[1], B.R. Ilyassov[2], A.K. Tussupbekova[1], A.K. Zeinidenov[1], A.M. Alexeev[1,3], A.M. Zhakanova[1]

[1]*Buketov University, Scientific Center for Nanotechnology and Functional Nanomaterials, Karaganda, Kazakhstan;*
[2]*Astana IT University, Astana, Kazakhstan;*
[3]*Kazan Federal University, Kazan, Russia*
*(*E-mail: ksusharogovaya@mail.ru)*

Effect of WS_2 nanoparticles on the current-voltage characteristics of a polymer solar cell

The paper presents the results of studies of the effect of tungsten disulfide nanoparticles on the optical and electrotransport characteristics of PEDOT: PSS thin films in polymer solar cells. Tungsten disulfide (WS_2) nanoparticles were obtained by laser ablation in isopropyl alcohol. The average size of nanoparticles were determined by dynamic light scattering and is ~38 nm. The concentration of WS_2 nanoparticles in the solution was calculated based on the density of the WS_2 substance. The absorption spectrum of nanoparticles in isopropyl alcohol has been measured. Two bands are observed in 500-900 nm regions, which are associated with direct exciton transitions A1 and B1 in two-dimensional transition metal dichalcogenides with 2H phase. WS_2 nanoparticles were added in PEDOT: PSS solution and thin films were deposited from the prepared solution by spin-coating. PEDOT: PSS thin films doped with WS_2 were studied by atomic force microscopy (AFM). The arithmetic mean deviation of the surface roughness (R_a) was estimated. Doping with WS_2 nanoparticles leads to the increase in R_a of PEDOT: PSS thin films. The optical absorption spectra of doped films have been measured. Also, doping PEDOT: PSS with WS_2 nanoparticles results in a long-wavelength shift of the PEDOT absorption maximum. The optimal concentration of WS_2 nanoparticles for the preparation of doped PEDOT: PSS thin films is determined, at which the film resistance decreases by almost 2 times, the recombination resistance of charge carriers increases by 4.7 times, and the efficiency of the polymer solar cell increases to 1.94 %.

Keywords: PEDOT: PSS, WS_2 nanoparticles, hole-transport layer, surface morphology, absorption spectra, impedance spectroscopy, organic solar cell, volt-ampere characteristics.

Introduction

In the last decade, organic solar cells (OSCs) have been widely developed due to their low cost, ease of fabrication, technology flexibility, large-scale production, and wide choice of materials. The power conversion efficiency of OSCs has now exceeded 18 % [1-4]. The boost of OSCs performance is attributed to the development of new materials for photoactive layers and due to the optimization of the film morphology [5-9]. However, the characteristics of a hole-transport layer, which extracts holes from the photoactive layer and deliver them to external electrodes, plays an important role in improving the PCE of the OSC [10-15].

Among hole-transport materials, the conjugated polymer poly(3,4-ethylenedioxythiophene): poly(4-styrenesulfonate) (PEDOT: PSS) is the most widely used hole-transport layer (HTL) in OSCs due to its excellent water solubility and high conductivity [16]. The analysis of previous works has shown that the reason for the low performance of organic solar cells with a PEDOT: PSS HTL is the presence of defects at the interface with the photoactive layer. As results, poor hole injection and severe recombination processes occurs in OCSs. To solve this problem, researchers have proposed various methods for modifying and introducing additives into PEDOT: PSS [17-24].

Two-dimensional transition metal dichalcogenides are used as such additives. They have attracted the attention of researchers due to their adjustable band gap and high carrier mobility [25, 26]. Due to the special single layer structure of WS_2, unshared pairs of electrons of the S atom can carry out fast transport, thereby increasing the mobility of charge carriers [3, 27]. These advantages allow us to consider them as promising materials for composite photovoltaic cells [28-31].

In this work, we have developed a completely new highly efficient composite hole-transport layer: PEDOT: PSS: NP WS_2. doped with WS_2 nanoparticles, which increased the efficiency of the organic solar cell by 1.8 times.

Experimental

The following materials were used in this work: PEDOT: PSS (1 %, Ossila Al4083), WS_2 (pure > 99 %, Borun Chemicals), P3HT (pure 97.6 %, Ossila), PC61BM (pure > 99 %, Ossila). The structural formulas of the chemicals are shown in Figure 1. The cleaning of the substrates was carried out according to the procedure described in [32]. Nanoparticles were fabricated by laser ablation of the WS_2 in Isopropanol. Nd: YAG solid-state laser (SOLAR LQ 529, λ_{gen} =532 nm, E_{pulse} =180 mJ, τ=20 ns) was used for the ablation. Ablation time ranged from 15 to 30 minutes.

Before the film deposition, the PEDOT: PSS solution was filtered through a 0.45 micrometer filter. Then nanoparticles were added to the PEDOT: PSS solution at various concentrations: from 2 % to 10 %. PEDOT: PSS: NP WS_2 nanocomposite films were spin-coated on the surface of FTO substrates (by SPIN150i spin-coater manufactured by Semiconductor Production System) at a rotation speed of 5000 rpm. After, the films were annealed at a temperature of 120 °C for 10 minutes to complete the solvent evaporation and improve film crystallinity.

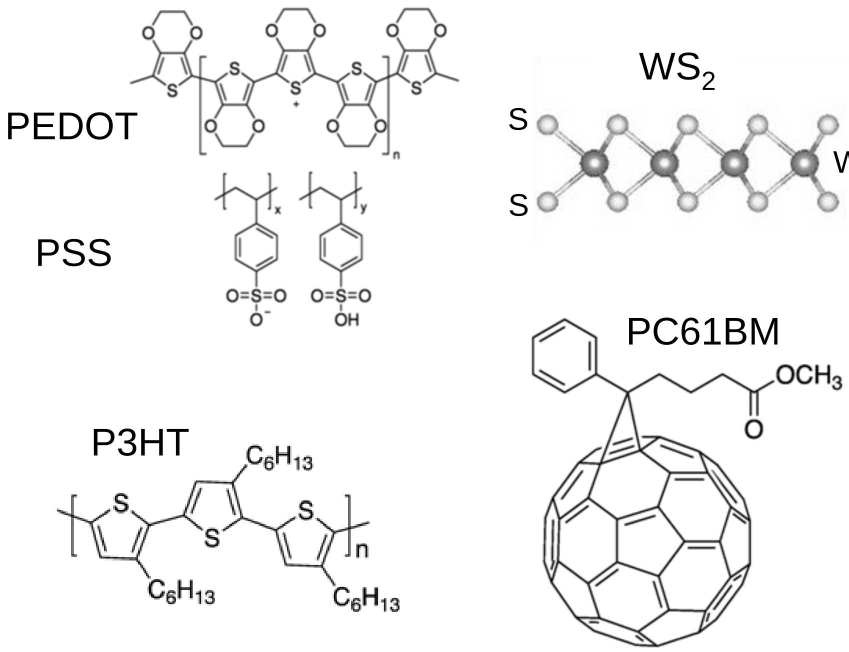

Figure 1. Structural formulas of PEDOT: PSS, WS_2, P3HT and PC61BM

As a photoactive layer of OSCs a mixture of P3HT: PC61BM with a ratio of 1:0.6 was used as a donor and acceptor material, respectively. The mixture was prepared as follows: P3HT (~15.6 mg) and PC61BM (~9.4 mg) were dissolved in 1 ml of chlorobenzene and the solution was stirred at 60 °C for 24 hours. The prepared solution was filtered through a 0.45 micrometer filter, and then deposited on the surface of PEDOT: PSS: NP WS_2/FTO/glass by spin-coating at a rotation speed of 2000 rpm. Next, the photoactive layer was subjected to thermal annealing at 120 °C for 10 minutes to improve the crystallinity of the film. Finally, aluminum electrodes with a thickness of 100 nm were deposited in a vacuum of 10^5 Torr by thermal evaporation using the CY-1700x-spc-2 evaporator (Zhengzhou CY Scientific Instruments Co., Ltd).

The surface topography of the samples was studied using the JSPM-5400 atomic force microscope (JEOL Ltd, Japan) and the Tescan Mira 3 electron microscope. The surface morphology parameters were calculated using the Winspm II Data Processing software package (JEOL Ltd). The size distribution of nanoparticles in isopropanol was determined by using the Zetasizer Nano ZS. The optical characteristics of the solution with nanoparticles and nanocomposite films were studied using the Avantes AvaSpec-ULS2048CL-EVO spectrometer. A combined deuterium-halogen AvaLight-DHc light source with an operating range of 200-2500nm was used as a radiation source. Measurements of the impedance spectra were carried out on a potentiostat-galvanostat P45X in the impedance mode. The spectra were fitted using the EIS-analyzer software package, and the experimental data were analyzed using diffusion-recombination models. The I-V characteristics of OCS cells were determined by the Sol3A Class AAA Solar Simulators (Newport) with PVIV-1A I-V Test Station.

Results and Discussion

Figure 2a shows the SEM image of WS_2 nanoparticles deposited on the surface of quartz glass. It can be seen from the Figure 2a that the nanoparticles have a round shape, their diameter varies from 10 to 50 nm. Figure 2b shows the absorption spectrum of WS_2 nanoparticles in isopropyl alcohol. The figure shows that two characteristic absorption peaks in the 500-900 nm region are clearly observed, which correspond to direct exciton transitions A1 and B1 in TMDC with the 2H phase [33-36].

The inset of Figure 2b shows the size distribution of WS_2 nanoparticles in an isopropyl alcohol solution. As can be seen from the diagram, the average size of nanoparticles in solution is 38 nm.

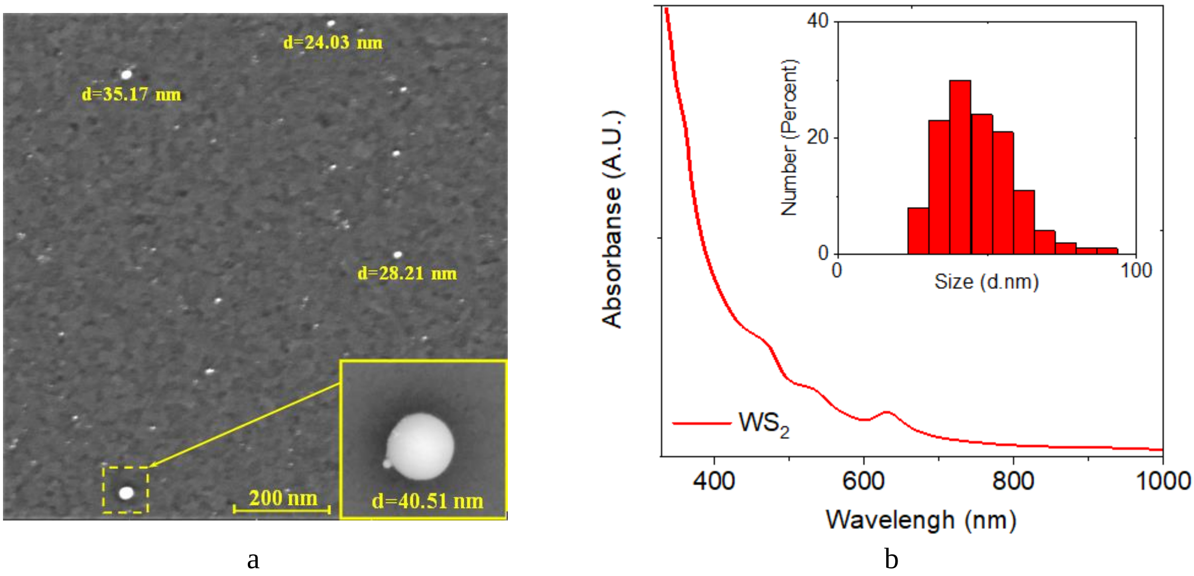

Figure 2. SEM image of WS_2 nanoparticles (a) and the absorption spectrum of WS_2 nanoparticles in isopropanol solution (b). In the insert, the size distribution of WS_2 nanoparticles in isopropanol solution

To fabricate nanocomposite films, WS_2 nanoparticles were added to a PEDOT: PSS solution. The concentration of WS_2 nanoparticles in the solution was calculated based on the density of WS_2 according to the formula:

$$C_{NP} = \frac{C_{WS_2}}{m_{NP} \cdot N_A} = \frac{C_{WS_2}}{\rho_{WS_2} \cdot V_{NP} \cdot N_A} = \frac{\frac{m_{WS_2}}{V_{sol} M_{WS_2}}}{\rho_{WS_2} \cdot \frac{4\pi r^3}{3} \cdot N_A} \left(\frac{mol}{L}\right),$$

where C_{NP} is the concentration of nanoparticles in solution;

C_{WS2} is the concentration of the substance in the solution before laser ablation of the WS_2;

m_{NP} is the weight of the average nanoparticle;

N_A is the Avogadro's number;

ρ_{WS2} is the density of WS_2 substance;

V_{NP} is the volume of the average nanoparticle;

m_{WS2} is the weight of the WS_2 substance;

V_{sol} is the volume of solvent used in laser ablation of the substance;

M_{WS2} is the molar mass of the WS_2 substance;

r is the average radius nanoparticle.

AFM images of the surface morphology of PEDOT: PSS nanocomposite films are shown in Figure 3. They shows that the pristine PEDOT: PSS has a fine-grained structure with the surface roughness (R_a) of 0.54 nm. Doping PEDOT: PSS with WS_2 nanoparticles affects R_a. The increase of the concentration from 0 to 6 % results in the slow growth of R_a from 0.54 nm to 0.58 nm, respectively (Table 1). Further increase of the concentration up to 10 % results to the sharp growth of Ra reaching a value of 0.75 nm. Table 1 and Figure 4 shows this surface roughness dependence on WS_2 nanoparticles concentration.

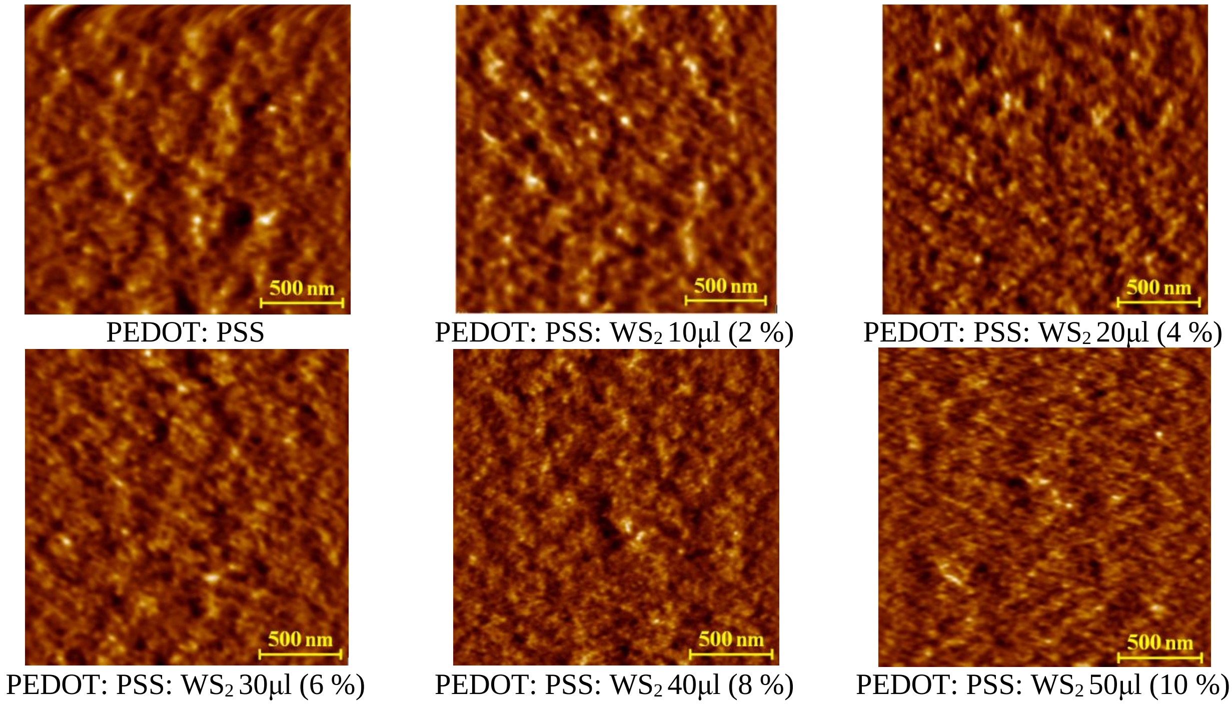

Figure 3. AFM images of PEDOT: PSS: WS_2 nanocomposite films with different concentrations of nanoparticles in solution

Table 1

The dependence of surface roughness WS_2 doped PEDOT: PSS thin films on WS_2 nanoparticles concentration

Sample	R_a, nm	C_{NP}, mol/L
PEDOT: PSS	0.54	0
PEDOT: PSS: WS_2 10μl (2 %)	0.56	$0.47 \cdot 10^{-13}$
PEDOT: PSS: WS_2 20μl (4 %)	0.57	$0.94 \cdot 10^{-13}$
PEDOT: PSS: WS_2 30μl (6 %)	0.58	$1.34 \cdot 10^{-13}$
PEDOT: PSS: WS_2 40μl (8 %)	0.74	$1.87 \cdot 10^{-13}$
PEDOT: PSS: WS_2 50μl (10 %)	0.75	$2.34 \cdot 10^{-13}$

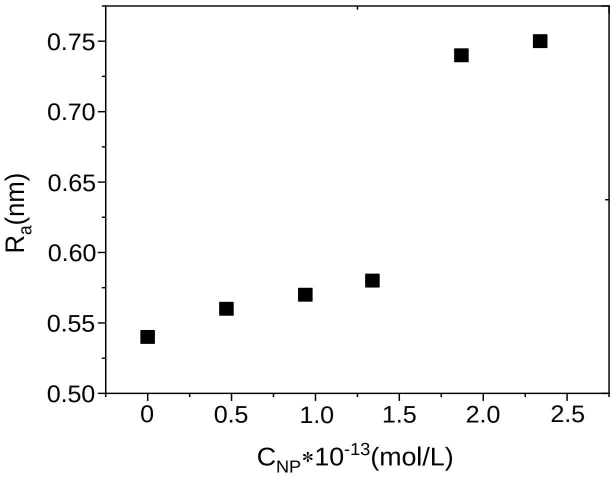

Figure 4. Diagram of dependence of film surface roughness on concentration of WS_2 nanoparticles in PEDOT: PSS polymer solution

Figure 5 shows the absorption spectra of PEDOT: PSS films. It can be seen from the Figure 5 that the PEDOT: PSS film has a maximum at a wavelength of λ_1 = 234.6 nm related to the absorption of PEDOT and a maximum at 278.2 nm associated with the absorption of the aromatic fragment of PSS [20, 21, 37]. When WS_2 nanoparticles are added to the PEDOT: PSS solution, the optical density decreases and a slight bathochromic shift of the PEDOT absorption maximum is observed. The observed long-wavelength shift of the PEDOT: PSS absorption maximum is associated with a change in the film structure due to the incorporation of WS_2 nanoparticles between the PEDOT and PSS chains [3, 21].

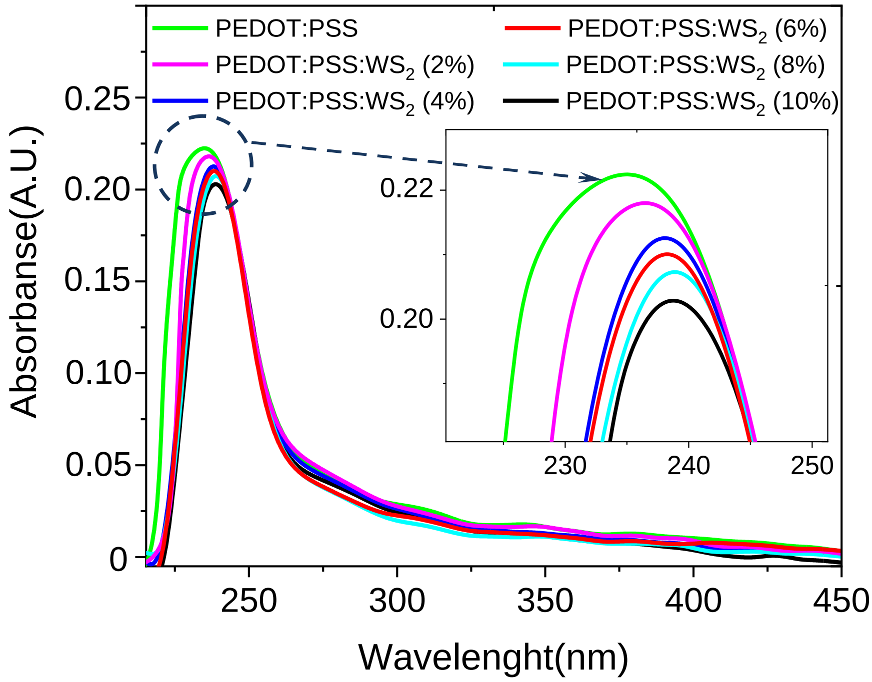

Figure 5. Absorption spectra of PEDOT: PSS: WS_2 nanocomposite films

Table 2

Spectral characteristics of PEDOT: PSS: WS_2 nanocomposite films

Sample	λ_1, nm	λ_2, nm
PEDOT: PSS	234.6	278.2
PEDOT: PSS: WS_2 (2 %)	236.5	278.2
PEDOT: PSS: WS_2 (4 %)	237.9	278.2
PEDOT: PSS: WS_2 (6 %)	238.0	278.2
PEDOT: PSS: WS_2 (8 %)	238.4	278.2
PEDOT: PSS: WS_2 (10 %)	238.9	278.2

The impedance spectra were measured to study the effect of WS_2 nanoparticles on electrotransport properties of the doped PEDOT: PSS film (Fig. 6). The fitting of the impedance spectra was carried out according to the diffusion-recombination model [38].

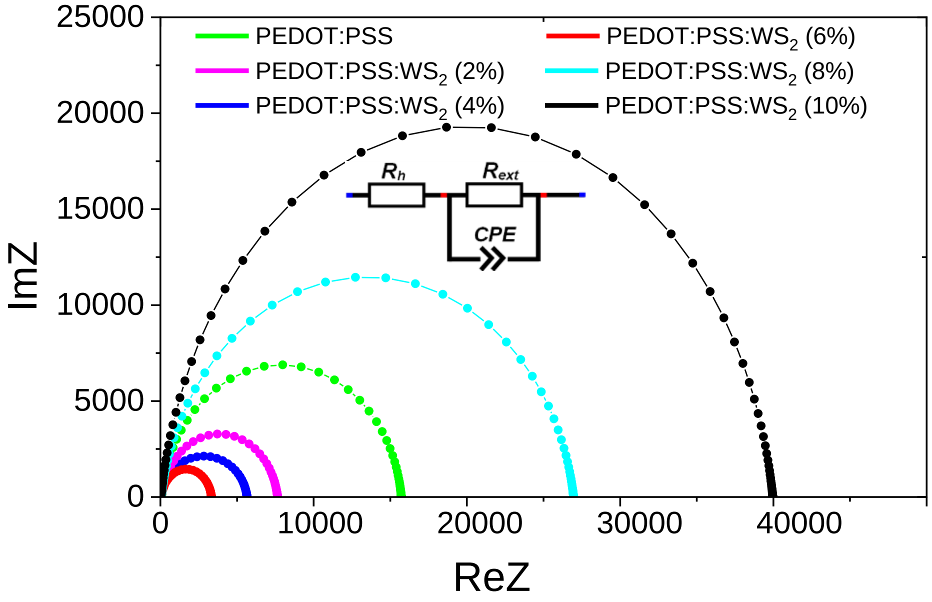

Figure 6. Effect of WS_2 nanoparticles on the impedance spectra of the PEDOT: PSS film

The electric transport characteristics were determined from the impedance spectra. The equivalent electrical circuit (Fig. 6) was used to fit impedance spectra. The Table 3 shows the main electrical transport characteristics of the PEDOT: PSS films, where: k_{eff} is the effective charge carrier extraction rate from PEDOT: PSS, τ_{eff} is the effective transit time through PEDOT: PSS layer, R_h is the PEDOT: PSS resistance film, R_{ext} is the transfer resistance of charge carriers at the PEDOT: PSS/electrode interface associated with the extraction of charge carriers from PEDOT: PSS.

Table 3

Effect of WS_2 nanoparticles on the electrotransport characteristics of a PEDOT: PSS film

Sample	R_h, Ω	R_{ext}, Ω	k_{eff}, s^{-1}	τ_{eff}, ms
PEDOT: PSS	71.923	15014	75.84	0.013
PEDOT: PSS: WS_2 (2 %)	61.51	7322.2	159.09	0.006
PEDOT: PSS: WS_2 (4 %)	59.33	5490.4	190.51	0.005
PEDOT: PSS: WS_2 (6 %)	45.3	3210.1	398.43	0.003
PEDOT: PSS: WS_2 (8 %)	69.547	25856	36.31	0.027
PEDOT: PSS: WS_2 (10 %)	63.633	38709	17.15	0.058

Next, PEDOT: PSS: NP WS_2 nanocomposite films were used as hole selective electrodes for organic solar cells based on the P3HT: PC61BM photoactive layer (Fig. 7a). The current-voltage curves of the fabricated organic cells are shown in Figure 7b.

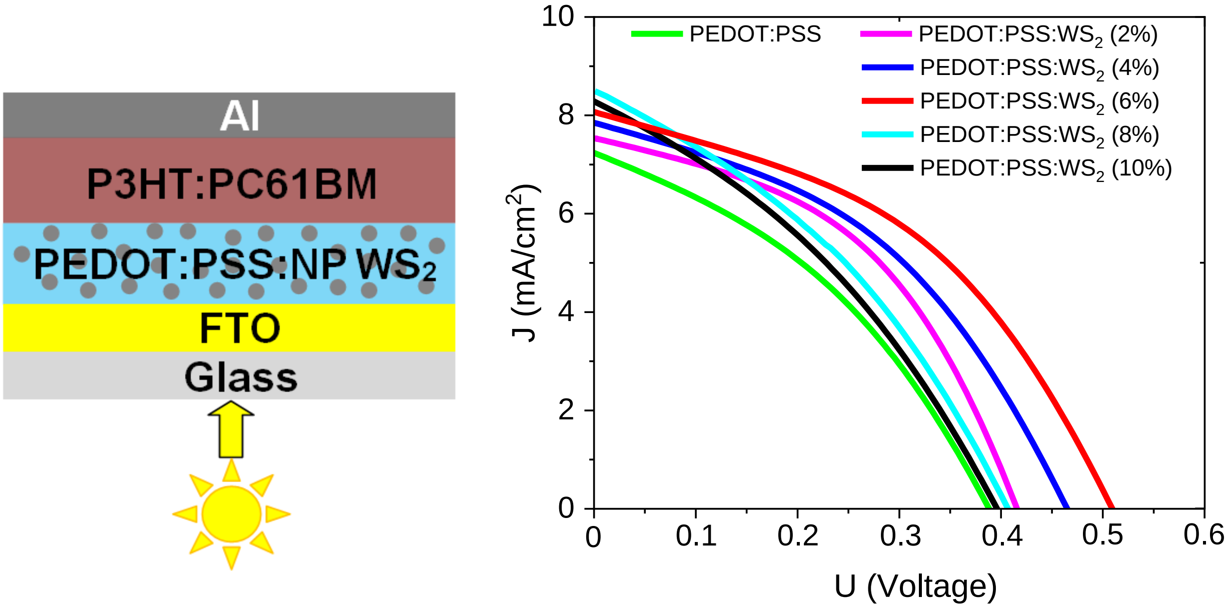

a b

Figure 7. Structure (a) and current-voltage characteristics (b) of an organic solar cell with FTO/PEDOT: PSS: NP WS_2/P3HT: PC61BM/Al architecture.

Table 4 shows the photovoltaic performance of organic solar cells. All OSCs based on PEDOT: PSS doped with WS_2 nanoparticles showed improved J_{sc} and PCE compared to the cell with pristine PEDOT: PSS. OSCs with 6 % WS_2 doped PEDOT: PSS revealed the best performance. In comparison with the device based on pristine PEDOT: PSS, $\boldsymbol{J_{sc}}$, V_{oc}, *FF*, and PCE of 6 % WS_2 doped PEDOT: PSS based device increased from 7.20 mA/cm^2 to 8.06 mA/cm^2, form 0.39 V to 0.49 V, from 0.37 to 0.49, and from 1.04 % to 1.94 %, respectively. This result indicates that the PEDOT: PSS hole-transport layer doped with WS_2 nanoparticles can block electrons more efficiently, which is an advantage for a higher *FF* value [3, 39, 40]. In addition, according to the impedance spectra, PEDOT: PSS with WS_2 nanoparticles provides faster injection and transport of holes to the external electrode (FTO), which reduces the probability of hole recombination with PC61BM and improve the efficiency of hole accumulation by the external electrode. However, at higher concentrations of WS_2 nanoparticles (8 % and 10 %) in PEDOT: PSS, a deterioration of the I-V parameters of the OCSs is observed, which is associated with high surface roughness of doped PEDOT: PSS.

Table 4

I-V characteristics of organic solar cells

Sample	J_{sc}, (mA/cm^2)	J_{max}, (mA/cm^2)	U_{oc}, (V)	U_{max}, (V)	Fill Factor	Efficiency, %
PEDOT: PSS	7.20	4.50	0.39	0.23	0.37	1.04
PEDOT: PSS: WS_2 (2 %)	7.56	5.31	0.42	0.27	0.45	1.43
PEDOT: PSS: WS_2 (4 %)	7.92	5.64	0.46	0.29	0.45	1.64
PEDOT: PSS: WS_2 (6 %)	8.06	6.25	0.49	0.31	0.49	1.94
PEDOT: PSS: WS_2 (8 %)	8.51	5.21	0.41	0.24	0.36	1.25
PEDOT: PSS: WS_2 (10 %)	8.24	4.96	0.40	0.23	0.35	1.14

Conclusion

As a result of study, it was found that moderate doping PEDOT: PSS with WS_2 nanoparticles leads to an increase in the efficiency of organic solar cells. WS_2 nanoparticles were obtained by laser ablation of the WS_2

in isopropyl alcohol. The average size of WS_2 nanoparticles was 38 nm. It has been shown that the addition of WS_2 nanoparticles to PEDOT: PSS affects the absorption spectra of nanocomposite films. It was found that when WS_2 nanoparticles are added to PEDOT: PSS, a bathochromic shift of the PEDOT absorption maximum is observed, which is associated with a change in the film structure due to the incorporation of WS_2 nanoparticles between the PEDOT and PSS chains. The optimal concentration of WS_2 nanoparticles in the PEDOT: PSS: NP WS_2 nanocomposite film was determined, which is 6 %. At this concentration, the resistance of the nanocomposite film decreases by almost 2 times, and the recombination resistance of charge carriers increases by 4.7 times. OSCs based on 6 % WS_2 doped PEDOT: PSS doped with showed the best performance with PCE of 1.94 %.

This research is funded by the Science Committee of the Ministry of Science and Higher Education of the Republic of Kazakhstan (Grant No. AP19174884).

References

1 Liu, Q., Jiang, Y., Jin, K., Qin, J., Xu, J., Li, W., Xiong, J., Liu, J., Xiao, Z., Sun, K., Yang, S., Zhang, X., & Ding, L. (2020). 18 % Efficiency organic solar cells, *Science Bulletin*, 65(4), 272-275. https://doi.org/10.1016/j.scib.2020.01.001.

2 Zhang, M., Zhu, L., Zhou, G., Hao, T., Qiu, C., Zhao, Z., Hu, Q., Larson, B.W., Zhu, H., Ma, Z., Tang, Z., Feng, W., Zhang, Y., Russell, T.P., & F. Liu. (2021). Single-layered organic photovoltaics with double cascading charge transport pathways: 18 % efficiencies, *Nature Communications*, 12, 309. https://doi.org/10.1038/s41467-020-20580-8.

3 Wang, Y., Li, N., Cui, M., Li, Y., Tian, X., Xu, X., Rong, Q., Yuan, D., Zhou, G., & Nian, L. (2021). High-performance hole transport layer based on WS_2 doped PEDOT: PSS for organic solar cells, *Organic Electronics*, 99, 106305. https://doi.org/10.1016/j.orgel.2021.106305.

4 Cui, Y., Yao, H., Zhang, J., Xian, K., Zhang, T., Hong, L., Wang, Y., Xu, Y., Ma, K., An, C., He, C., Wei, Z., Gao, F., & Hou, J. (2020). Single-junction organic photovoltaic cells with approaching 18 % efficiency, *Advanced Materials*, 32(19), 1908205. https://doi.org/10.1002/adma.201908205.

5 Nian, L., Kan, Y., Gao, K., Zhang, M., Li, N., Zhou, G., Jo, S.B., Shi, X., Lin, F., Rong, Q., Liu, F., Zhou, G., & Jen, A.K.Y. (2020). Approaching 16 % efficiency in all-small-molecule organic solar cells based on ternary strategy with a highly crystalline acceptor, *Joule*, 4(10), 2223-2236. https://doi.org/10.1016/j.joule.2020.08.011.

6 Gao, K., Kan, Y., Chen, X., Liu, F., Kan, B., Nian, L., Wan, X., Chen, Y., Peng, X., Russell, T.P., Cao, Y., & Jen, A.K. (2020). Low-bandgap porphyrins for highly efficient organic solar cells: materials, morphology, and applications, *Advanced Materials*, 32(32), 1906129. https://doi.org/10.1002/adma.201906129.

7 Gao, K., Jo, S.B., Shi, X., Nian, L., Zhang, M., Kan, Y., Lin, F., Kan, B., Xu, B., Rong, Q., Shui, L., Liu, F., Peng, X., Zhou, G., Cao, Y., & Jen, A.K. (2019). Over 12 % efficiency nonfullerene all-small-molecule organic solar cells with sequentially evolved multilength scale morphologies, *Advanced Materials*, 31(12), 1807842. https://doi.org/10.1002/adma.201807842.

8 Zhu, L., Zhang, M., Zhou, G., Hao, T., Xu, J., Wang, J., Qiu, C., Prine, N., Ali, J., Feng, W., Gu, X., Ma, Z., Tang, Z., Zhu, H., Ying, L., Zhang, Y., & Liu, F. (2020). Efficient organic solar cell with 16.88 % efficiency enabled by refined acceptor crystallization and morphology with improved charge transfer and transport properties, *Advanced Energy Materials*, 10(18), 1904234. https://doi.org/10.1002/aenm.201904234.

9 Yuan, J., Zhang, Y., Zhou, L., Zhang, G., Yip, H.-L., Lau, T.-K., Lu, X., Zhu, C., Peng, H., Johnson, P.A., Leclerc, M., Cao, Y., Ulanski, J., Li, Y., & Zou, Y. (2019). Single-junction organic solar cell with over 15 % efficiency using fused-ring acceptor with electron-deficient core, *Joule*, 3(4), 1140-1151. https://doi.org/10.1016/j.joule.2019.01.004.

10 Zheng, Z., Hu, Q., Zhang, S., Zhang, D., Wang, J., Xie, S., Wang, R., Qin, Y., Li, W., Hong, L., Liang, N., Liu, F., Zhang, Y., Wei, Z., Tang, Z., Russell, T.P., Hou, J., & Zhou, H. (2018). A highly efficient non-fullerene organic solar cell with a fill factor over 0.80 enabled by a fine-tuned hole-transporting layer, *Advanced Materials*, 30(34), 1801801. https://doi.org/10.1002/adma.201801801.

11 Duan, L., Sang, B., He, M., Zhang, Y., Hossain, M.A., Rahaman, M.H., Wei, Q., Zou, Y., Uddin, A., & Hoex, B. (2020). Interface modification enabled by atomic layer deposited ultra ultrathin titanium oxide for high-efficiency and semitransparent organic solar cells, *Solar RRL*, 4(12), 2000497. https://doi.org/10.1002/solr.202000497.

12 Song, X., Liu, G., Gao, W., Di, Y., Yang, Y., Li, F., Zhou, S., & Zhang, J. (2021). Manipulation of zinc oxide with zirconium doping for efficient inverted organic solar cells, *Small*, 17(7), 2006387. https://doi.org/10.1002/smll.202006387.

13 Zhou, H., Zhang, Y., Mai, C.K., Seifter, J., Nguyen, T.Q., Bazan, G.C., & Heeger, A.J. (2015). Solution-processed pH-neutral conjugated polyelectrolyte improves interfacial contact in organic solar cells, *ACS Nano*, 9(1), 371-377. https://doi.org/10.1021/nn505378m.

14 Zhou, H., Zhang, Y., Mai, C.K., Collins, S.D., Nguyen, T.Q., Bazan, G.C., & Heeger, A.J. (2014). Conductive conjugated polyelectrolyte as hole-transporting layer for organic bulk heterojunction solar cells, *Advanced Materials*, 26(5), 780-785. https://doi.org/10.1002/adma.201302845.

15 Zilberberg, K., Gharbi, H., Behrendt, A., Trost, S., & Riedl, T. (2012). Low-temperature, solution-processed MoO(x) for efficient and stable organic solar cells, *ACS Applied Materials & Interfaces*, 4(3), 1164-1168. https://doi.org/10.1021/am201825t.

16 Yin, B., Liu, Q., Yang, L., Wu, X., Liu, Z., Hua, Y., Yin, S., & Chen, Y. (2010). Buffer layer of PEDOT: PSS/graphene composite for polymer solar cells, *Journal of Nanoscience and Nanotechnology*, 10(3), 1934-1938. https://doi.org/10.1166/jnn.2010.2107.

17 Hu, L., Song, J., Yin, X., Su, Z., & Li, Z. (2020). Research progress on polymer solar cells based on PEDOT: PSS electrodes, *Polymers*, 12(1), 145. https://doi.org/10.3390/polym12010145.

18 Xia, Y., & Dai, S. (2021). Review on applications of PEDOTs and PEDOT: PSS in perovskite solar cells, *Journal of Materials Science: Materials in Electronics*, 32, 12746-12757. https://doi.org/10.1007/s10854-020-03473-w.

19 Yang, Y., Deng, H., & Fu, Q. (2020). Recent progress on PEDOT: PSS based polymer blends and composites for flexible electronics and thermoelectric devices, *Materials Chemistry Frontiers*, 4, 3130-3152. https://doi.org/10.1039/d0qm00308e.

20 Aimukhanov, A.K., Rozhkova, X.S., Ilyassov, B.R., Zeinidenov, A.K., & Nuraje, N. (2021). The influence of structural and charge transport properties of PEDOT: PSS layers on the photovoltaic properties of polymer solar cells, *Polymers for Advanced Technologies*, 32(2), 497-504. https://doi.org/10.1002/pat.5102.

21 Rozhkova, X.S., Aimukhanov, A.K., Ilyassov, B.R., & Zeinidenov, A.K. (2022). The role of alcoholic solvents in PEDOT: PSS modification as hole transport layers for polymer solar cells, *Optical Materials*, 131, 112708. https://doi.org/10.1016/j.optmat.2022.112708.

22 Aimukhanov, A.K., Rozhkova, X.S., Zeinidenov, A.K., & Seisembekova, T.E. (2021). Influence of surface structure and morphology of PEDOT: PSS on its optical and electrophysical characteristics, *Bulletin of the University of Karaganda-Physics*, 103(3), 93-100. https://doi.org/10.31489/2021ph3/93-100.

23 Aimukhanov, A., Rozhkova, X., Ilyassov, B., Omarbekova, G., & Seisembekova, T. (2022). Effect of alcohol solvents on the structural, optical and electrical characteristics of PEDOT: PSS polymer films annealed at low atmospheric pressure, *Eurasian Physical Technical Journal*, 19, 2(40), 35-41. https://doi.org/10.31489/2022No2/35-41.

24 Rozhkova, X.S., Aimukhanov, A.K., Zeinidenov, A.K., & Alexeev A.M. (2022). Influence of the environment on the morphology, optical and electrical characteristics of the PEDOT: PSS polymer, *Bulletin of the University of Karaganda-Physics,* 106(2), 117-126. https://doi.org/10.31489/2022Ph1/117-126.

25 Nguyen, E.P., Carey, B.J., Daeneke, T., Ou, J.Z., Latham, K., Zhuiykov, S., & Kalantar-Zadeh, K. (2015). Investigation of two-solvent grinding-assisted liquid phase exfoliation of layered MoS_2, *Chemistry of Materials*, 27(1), 53-59. https://doi.org/10.1021/cm502915f.

26 Chhowalla, M., Shin, H.S., Eda, G., Li, L.J., Loh, K.P., & Zhang, H. (2013). The chemistry of two dimensional layered transition metal dichalcogenide nanosheets, *Nature Chemistry*, 5, 263-275. https://doi.org/10.1038/nchem.1589.

27 Chang, J., Register, L.F., & Banerjee, S.K. (2013). Atomistic Full-band simulations of monolayer MoS_2 transistors, *Applied Physics Letters*, 103(22), 10451-10453. https://doi.org/10.1063/1.4837455.

28 Anrango-Camacho, C., Pavón-Ipiales, K., Frontana-Uribe, B.A., & Palma-Cando, A. (2022). Recent advances in hole-transporting layers for organic solar cells, *Nanomaterials*, 12(3), 443. https://doi.org/10.3390/nano12030443.

29 Cheng, R., Li, D., Zhou, H., Wang, C., Yin, A., Jiang, S., Liu, Y., Chen, Y., Huang, Y., & Duan, X. (2014). Electroluminescence and photocurrent generation from atomically sharp WSe_2/MoS_2 heterojunction p–n diodes, *Nano Letters*, 14(10), 5590-5597. https://doi.org/10.1021/nl502075n.

30 Lin, Y., Adilbekova, B., Firdaus, Y., Yengel, E., Faber, H., Sajjad, M., Zheng, X., Yarali, E., Seitkhan, A., Bakr, O.M., El-Labban, A., Schwingenschlogl, U., Tung, V., McCulloch, I., Laquai, F., & Anthopoulos, T.D. (2019). 17 % efficient organic solar cells based on liquid exfoliated WS_2 as a replacement for PEDOT: PSS, *Advanced Materials*, 31(46), 1902965. https://doi.org/10.1002/adma.201902965.

31 Chang, J., Register, L.F., & Banerjee, S.K. (2013). Atomistic Full-band simulations of monolayer MoS_2 transistors, *Applied Physics Letters*, 103, 223509. https://doi.org/10.1063/1.4837455.

32 Kim, K., Ihm, K. & Kim, B. (2015). Surface property of indium tin oxide (ITO) after various methods of cleaning, *Acta Physica Polonica A*, 127(4), 1176-1179. https://doi.org/10.12693/APhysPolA.127.1176.

33 Dong, N., Li, Y., Feng, Y., Zhang, S., Zhang, X., Chang, C., Fan, J., Zhang, L., & Wang, J. (2015). Optical limiting and theoretical modelling of layered transition metal dichalcogenide nanosheets, *Scientific Reports*, 5, 14646. https://doi.org/10.1038/srep14646.

34 Coleman, J.N., Lotya, M., O'neill, A., Bergin, S.D., King, P.J., Khan, U., Young, K., Gaucher, A., De, S., Smith, R.J., Shvets, I.V., Arora, S.K., Stanton, G., Kim, H.-Y., Lee, K., Kim, G.T., Duesberg, G.S., Hallam, T., Boland, J.J., Wang, J.J., Donegan, J.F., Grunlan, J.C., Moriarty, G., Shmeliov, A., Nicholls, R.J., Perkins, J.M., Grieveson, E.M., Theuwissen, K., Mccomb, D.W., Nellist, P.D., & Nicolosi, V. (2011). Two-dimensional nanosheets produced by liquid exfoliation of layered materials, *Science*, 331(6017), 568-571. https://doi.org/10.1126/science.119497.

35 Liu, H.-L., Shen, C.-C., Su, S.-H., Hsu, C.-L., Li, M.-Y., & Li, L.-J. (2014). Optical properties of monolayer transition metal dichalcogenides probed by spectroscopic ellipsometry. *Applied Physics Letters*, 105(20), 201905. https://doi.org/10.1063/1.4901836.

36 Eda, G., & Maier, S. A. (2013). Two-dimensional crystals: managing light for optoelectronics. *ACS Nano*, 7(7), 5660-5665. https://doi.org/10.1021/nn403159y.

37 Xia, Y., Sun, K., & Ouyang, J. (2012). Highly conductive poly(3,-4-ethylenedioxythiophene): poly(styrene sulfonate) films treated with an amphiphilic fluoro compound as the transparent electrode of polymer solar cells, *Energy & Environmental Science*, 5, 5325-5332. https://doi.org/10.1039/C1EE02475B.

38 Yuan, X., Song, C., Wang, H., & Zhang, J. (2010). EIS Equivalent Circuits in Electrochemical Impedance Spectroscopy in PEM Fuel Cells. *Springer-Verlag,* London, England, 420p. https://doi.org/10.1007/978-1-84882-846-9.

39 Khanam, J.J., & Foo, S.Y. (2019). Modeling of high-efficiency multi-junction polymer and hybrid solar cells to absorb infrared light, *Polymers*, 11(2), 383. https://doi.org/10.3390/polym11020383.

40 Xing, W., Chen, Y., Wu, X., Xu, X., Ye, P., Zhu, T., Guo, Q., Yang, L., Li, W., & Huang, H. (2017). PEDOT: PSS-assisted exfoliation and functionalization of 2D nanosheets for high-performance organic solar cells, *Advanced Functional Materials,* 27(32), 1701622. https://doi.org/10.1002/adfm.201701622.

К.С. Рожкова, А.К. Аймуханов, Б.Р. Ильясов, А.К. Тусупбекова,
А.К. Зейниденов, А.М. Алексеев, А.М. Жаканова

WS_2 нанобөлшектерінің полимерлі күн элементінің вольт-амперлік сипаттамаларына әсері

WS_2 нанобөлшектерінің PEDOT: PSS полимерлі күн элементінің оптикалық және электр тасымалдау сипаттамаларына әсері туралы зерттеу нәтижелері келтірілген. WS_2 нанобөлшектері изопропил спиртіндегі лазерлік абляция әдісімен алынды. Нанобөлшектердің орташа өлшемдері жарықтың динамикалық шашырау әдісімен анықталды және ~ 38 нм құрады. Ерітіндідегі WS_2 нанобөлшектерінің концентрациясын есептеу WS_2 затының тығыздығына негізделген. Изопропил спиртіндегі нанобөлшектердің жұтылу спектрі өлшенді. Жұтылу спектрінде 500-900 нм аймағында байқалған екі максимум 2H фазасындағы екі өлшемді өтпелі металл дихалькогенидтерінің A1 және B1 түзу экситондық ауысуларымен байланысты. WS_2 нанобөлшектері қабыршақтүзетін ерітінді дайындау сатысында PEDOT: PSS-ке легирленген. АКМ суреттері бойынша бағаланатын бетінің R_a орташа арифметикалық ауытқу параметрі анықталды. WS_2 нанобөлшектерін қосу қабыршақтың R_a параметрінің артуына алып келеді. Нанокомпозиттік қабыршақтардың оптикалық жұтылу спектрлері өлшенді. WS_2 нанобөлшектерін PEDOT: PSS-ке легирлеген кезде PEDOT жұтылу максимумының ұзын толқынды ығысуы байқалады. Қабыршақ кедергісі шамамен 2 есе азаятын, заряд тасушылардың рекомбинациялық кедергісі 4,7 есе артатын, ал полимерлі күн батареясының тиімділігі 1,94 % дейін артатын PEDOT: PSS: NP WS_2 нанокомпозиттік қабыршағының құрамындағы WS_2 нанобөлшектерінің критикалық концентрациясы анықталды.

Кілт сөздер: PEDOT: PSS, WS_2 нанобөлшектер, кемтікті-тасымалдаушы қабат, беттік морфология, жұтылу спектрлері, импеданс спектроскопиясы, органикалық күн ұяшығы, вольт-амперлік сипаттамалары.

К.С. Рожкова, А.К. Аймуханов, Б.Р. Ильясов, А.К. Тусупбекова,
А.К. Зейниденов, А.М. Алексеев, А.М. Жаканова

Влияние наночастиц WS_2 на вольт-амперные характеристики полимерного солнечного элемента

Представлены результаты исследований влияния наночастиц WS_2 на оптические и электротранспортные характеристики PEDOT: PSS полимерного солнечного элемента. Наночастицы WS_2 были получены методом лазерной абляции в изопропиловом спирте. Средние размеры наночастиц были определены методом динамического рассеяния света и составили ~ 38 нм. Расчет концентрации наночастиц WS_2 в растворе производился, исходя из плотности вещества WS_2. Измерен спектр поглощения наночастиц в изопропиловом спирте. Наблюдаемые два максимума в спектре поглощения в области 500–900 нм связаны с прямыми экситонными переходами A1 и B1 двумерных дихалькогенидов переходных металлов в 2H-фазе. Наночастицы WS2 были легированы в PEDOT: PSS на стадии приготовления пленкообразующего раствора. По АСМ снимкам был определен параметр среднеарифметического отклонения оцениваемой поверхности R_a. Допирование наночастицами WS_2 приводит к изменению R_a пленки в сторону возрастания. Измерены спектры оптического поглощения нанокомпозитных пленок. Показано, что при легировании наночастиц WS2 в PEDOT: PSS наблюдается длинноволновый сдвиг максимума поглощения PEDOT. Определена критическая концентрация наночастиц WS_2 в составе нанокомпозитной пленки PEDOT: PSS: NP WS_2, при которой сопротивление пленки уменьшается почти в 2 раза, рекомбинационное сопротивление носителей заряда возрастает в 4,7 раза, а эффективность полимерного солнечного элемента увеличивается до 1,94 %.

Ключевые слова: PEDOT: PSS, наночастицы WS_2, дырочно-транспортный слой, морфология поверхности, спектры поглощения, импедансная спектроскопия, органическая солнечная ячейка, вольт-амперные характеристики.

DOI 10.31489/2023PH1/23-30

UDC 534.2

S.K. Tleukenov[1], Zh.N. Suierkulova[1], S.A. Nurkenov[2]

[1]L.N. Gumilyov Eurasian National University, 2, Satpayev St., Astana, 010008, Republic of Kazakhstan
e-mail: zhamila_kudaibergen@mail.ru
[2]Astana International University Kabanbai Batyr Ave 8, 010000, Republic of Kazakhstan
e-mail: S.Nurkenov@gmail.com

Indicatrix of TE and TM- polarized wave velocities in crystal of classes 4mm, 3m, 6mm with magneto-electric effect

This work is devoted to the theoretical study of the laws of propagation of electromagnetic waves of TE and TM polarization in anisotropic media belonging to classes 4mm, 3m, 6mm, etc. having a magnetoelectric effect. The directions of the vectors of the phase and group velocities of the polarization waves TE and TM at the boundary of a uniaxial crystal with magnetoelectric properties are considered. In the analytical form, the values of the directions of the phase and group velocities of the TE and TM waves are indicated, depending on the direction of the wave vector of the incident wave. The consequences of the obtained results for uniaxial crystals in the absence of magnetoelectric properties are discussed. The solution of the tasks set in this paper is based on the use of the matrix method. On its basis, various problems of wave processes in an isotropic elastic medium, electromagnetic waves in crystals, the distribution of coupled elastic and electromagnetic waves in piezoelectric and piezomagnetic media with a magnetoelectric effect were previously considered. In the presence of a magnetoelectric effect for electromagnetic waves propagating through uniaxial crystals, the parameters of the wave vector, phase and group velocities are determined. The obtained results are analyzed for electromagnetic waves propagating through uniaxial crystals in the absence of a magnetoelectric effect.

The indicatrices of the wave vectors propagating in the plane and the phase velocities of the TM polarization waves are limited $(x0z)$. Based on the Rayleigh equation, the values of the group velocity are obtained. The density of electromagnetic energy fluxes and their components are determined for TE and TM waves. The energy transfer rate and its direction are determined. It is shown that the group velocities and directions obtained from the Rayleigh equation and the Umov-Poynting vector do not coincide.

Key words: anisotropy, electromagnetic waves, uniaxial crystals, magnetoelectric effect, phase and group velocities, TE and TM polarization waves, density vector.

Introduction

Active theoretical and experimental study of heterostructures and composite materials with piezoelectric, piezomagnetic, magnetostrictive and ferromagnetic properties are currently underway.

The aim of research is to create materials with magnetoelectric properties, for their practical application in instrument engineering, micro and nanoelectronics, information technologies [1-4].

The paper discusses the theoretical study of the patterns of TE and TM- polarized electromagnetic waves propagation in anisotropic medium related to classes 4mm, 3m, 6mm, etc., with magnetoelectric effect.

A tensor describing the magnetoelectric effect is adopted in the form [1]:

$$\hat{\alpha} = \begin{Bmatrix} 0 & \alpha_{xy} & 0 \\ -\alpha_{xy} & 0 & 0 \\ 0 & 0 & \alpha_z \end{Bmatrix}. \quad (1)$$

Wave processes are considered based on Maxwell's equations:

$$rot\vec{E} = -\frac{\partial \vec{B}}{\partial t}; \ rot\vec{H} = \frac{\partial \vec{D}}{\partial t} \quad (2)$$

$$div\vec{D} = 0; \quad div\vec{B} = 0; \quad (3)$$

The material ratio has the following form:

$$D_i = \varepsilon_0 \varepsilon_{ij} E_j - \alpha_{ij} H_j, \quad B_i = \mu_0 \mu_{ij} H_j - \alpha_{ij} E_j. \quad (4)$$

Dielectric and magnetic constant tensors correspond to their type for uniaxial crystals.

The ratios (6) taking into account (1) have the form:

$$\begin{aligned} &D_x = \varepsilon_x E_x - \alpha_{xy} H_y, \quad D_y = \varepsilon_y E_y + \alpha_{xy} H_x, \quad D_z = \varepsilon_z E_z \\ &B_x = \mu_x H_x - \alpha_{xy} E_y, \quad B_y = \mu_y H_y + \alpha_{xy} E_x, \quad B_z = \mu_z H_z \end{aligned} \quad (5)$$

For uniaxial crystals $\varepsilon_x = \varepsilon_y$; $\mu_x = \mu_y$ absolute permeability to vacuum ε_0 *u* μ_0 is contained in ε_{ij} *u* μ_{ij}.

1. Propagation of electromagnetic waves in the plane **(** $x0z$ **),** $k_y = 0$.

Solution and study in the form of flat waves. Presenting these solutions for electrical and magnetic field components as [5], [7-10]:

$$f(x, y, z, t) = f(x) e^{i\omega t - ik_z z}, \quad (1.1)$$

taking into account the absence of dependence, in this case, on the coordinate *y*, a system of equations was obtained from equations (2), (3) and relations (7):

$$\frac{dE_y}{dx} = -i\omega\mu_z E_z \quad (1.2)$$

$$\frac{dH_z}{dx} = i(\omega\varepsilon_y - \frac{k_z^2 - \omega^2\alpha_{xy}^2}{\omega\mu_x})H_z \quad (1.3)$$

$$\frac{dH_y}{dx} = i\omega\varepsilon_z E_z \quad (1.4)$$

$$\frac{dE_z}{dx} = i(\omega\mu_y - \frac{k_z^2 - \omega^2\alpha_{xy}^2}{\omega\varepsilon_x})H_y. \quad (1.5)$$

The systems of equations (1.2), (1.3) and (1.4), (1.5) are independent. Equations (1.2), (1.3) describe the propagation of TE-polarized waves. Equations (1.4), (1.5) — TM-polarized waves.

1.1 The equation of indicatrices of the TE- wave vector follows from the condition:

Within the framework of the matrix method of the matricant for homogeneous media, the wave vector indicatrix equation can be determined from the condition [12-14]:

$$\det\left[B^2+k_z^2 I\right]=0, \qquad (1.6)$$

$\det\left[T-Ie^{-i\tilde{k}h}\right]=0$, $\left(\tilde{k}=k_z\right)$. This follows from the relations $\vec{W}(h)=T(h)\vec{W}_0;\ \vec{W}(h)=\mathrm{e}^{-ik_zh}\vec{W}_0$ and is a consequence of the Floquet-Bloch theorem [13].

With periodic changes in parameters along the z axis:

$$\varepsilon_{ij}(z+h)=\varepsilon_{ij}(z),\quad \mu_{ij}(z+h)=\mu_{ij}(z),\quad \alpha_{ij}(z+h)=\alpha_{ij}(z).$$

Matrix $T(nh)=T^n(h);\ T(h)$ - the monodromy matrix. For $T^n(h)$ the representation based on Chebyshev-Gegenbauer polynomials is valid. The matrix is a monodromy matrix. A representation based on Chebyshev-Gegenbauer polynomials is valid for.

$$T^n(h)=P_n(\hat{p})T(h)-P_{n-1}(\hat{p}).$$

Calculation of matrix polynomials $P_n(\hat{p})$ is shown in the paper [14]. The dispersion equation, based on knowledge of the matrix structure, can be written in two equivalent forms:

$$\det\left[T(h)-Ie^{-ik_zh}\right]=0,\ \det\left[T^{-1}(h)-Ie^{ik_zh}\right]=0.$$

In view of their equivalence, a modified condition follows from them:

$$\det\left[\hat{p}-I\cos k_zh\right]=o. \qquad (1.6^*)$$

Under the condition $\lambda\succ\succ h$ (λ is the wavelength, h is the period of in homogeneity), analytical representations of matrices for homogeneous media are obtained from (1.6*). In particular, this is due to

where $p=\frac{1}{2}(T+T^{-1});\quad \cos k_z h=\frac{e^{-ik_zh}+e^{ik_zh}}{2}$

$\frac{d\vec{W}}{dz}=B(z)\vec{W};\quad B(z)=\begin{pmatrix}0 & b_{12}\\ b_{21} & 0\end{pmatrix}$. The matrix T has the form: $T^{\pm1}(z)=I\cos k_zz\pm\frac{1}{k_z}B\sin k_zz$,

$B=\frac{1}{h}\int\limits_0^h B(z)dz$. When decomposed by $k_z\sim\frac{1}{\lambda},\ \frac{h}{\lambda}\prec\prec1,\quad h$ not enough because: $\hat{p}=\frac{1}{2}(T+T^{-1});$ T and T^{-1} direct and inverse monodromy matrices.

Have representations [8]: $T=I+\int\limits_0^h B(z)dz+\int\limits_0^h\int\limits_0^z B(z)B(z_1)dzdz_1+.....$

Similarly: $T^{-1}=I-\int\limits_0^h B(z)dz+\int\limits_0^h\int\limits_0^z B(z_1)B(z)dz_1dz+.....$

then, provided $k_zh\prec\prec1$ and small h, while preserving the summands up to quadratic terms, we have, in the case of homogeneous media:

$$T=I+Bh+\frac{B^2h}{2};\quad T^{-1}=I-Bh+\frac{B^2h}{2};\quad B=\frac{1}{h}\int\limits_0^h B(z)dz$$

$p=\frac{1}{2}(T+T^{-1})=I+\frac{B^2h}{2}$. For $\cos k_zh=1-\frac{k_z^2h^2}{2}$. Then from (1.6*) should: $\det\left[B^2+Ik_z^2\right]=0$

$$B=\begin{pmatrix}0 & b_{12}\\ b_{21} & 0\end{pmatrix};\ b_{12}=-i\omega\mu_z,\ b_{21}=i\omega\varepsilon_y-i\frac{k_z^2-\omega^2\alpha_{xy}^2}{\omega\mu_x}, \qquad (1.7)$$

from (1.6) follows: ($k_y = k\cos\theta$, $k_z = k\sin\theta$)

$$k_{TE}^2 = \frac{\omega^2\mu_z(\varepsilon_y\mu_x + \alpha_{xy}^2)}{\mu_x\cos^2\theta + \mu_z\sin^2\theta}, \tag{1.8}$$

θ-angle between axis x and wave vector $\vec{k}$. The TE-wave phase velocity indicatrix based on (1.8) has the form:

$$\nu_{f_{TE}}^2 = \frac{\omega^2}{k^2} = \frac{\mu_x\cos^2\theta + \mu_z\sin^2\theta}{\mu_z(\varepsilon_y\mu_x + \alpha_{xy}^2)}, \tag{1.9}$$

the group velocity is from the Rayleigh equation [5-7]:

$$\vec{v}_g = \vec{n}v_f + \vec{n}_\theta\frac{\partial v_f}{\partial\theta}; \qquad \nu_\theta = \frac{\partial\nu_f}{\partial\theta}, \tag{1.10}$$

unit vector $\vec{n}$ determines direction of phase velocity, $\vec{n}_\theta$ - unit vector perpendicular to $\vec{n}$ vector $\vec{n}$

$$\nu_\theta = \frac{(\mu_z - \mu_x)\sin\theta\cos\theta}{a\nu_f}; \qquad a = \mu_z(\varepsilon_y\mu_x + \alpha_{xy}^2), \tag{1.11}$$

formula (1.9) — (1.11) for group velocity value:

$$v_g^2 = v_f^2 + v_\theta^2, \tag{1.12}$$

angle γ between phase group velocity vectors determines the relation:

$$\tan\gamma = \frac{v_\theta}{v_f} = \frac{(\mu_z - \mu_x)\sin\theta\cos\theta}{\mu_x^2\cos^2\theta + \mu_z\sin^2\theta}, \tag{1.13}$$

from (1.9) — (1.13) follows:

$$v_{g_{TE}}^2 = \frac{1}{a}\frac{\mu_x^2\cos^2\theta + \mu_z^2\sin^2\theta}{\mu_x\cos^2\theta + \mu_z\sin^2\theta}. \tag{1.14}$$

1.2. TM wave indicatrices

In this case:

$$b_{12} = i\omega\varepsilon_z, \quad b_{21} = i(\omega\mu_y - \frac{k_z^2 - \omega^2\alpha_{xy}^2}{\omega\varepsilon_x}), \tag{1.15}$$

condition (1.6) gives the indicatrix of the TM wave vector:

$$k_{TM}^2 = \frac{\omega^2\varepsilon_z(\mu_y\varepsilon_x + \alpha_{xy}^2)}{\varepsilon_x\cos^2\theta + \varepsilon_z\sin^2\theta}. \tag{1.16}$$

Calculations similar to those in paragraph 1.1 result in the following formulas:

$$\nu_{f_{TM}}^2 = \frac{\varepsilon_x\cos^2\theta + \varepsilon_z\sin^2\theta}{\varepsilon_z(\varepsilon_x\mu_y + \alpha_{xy}^2)} \tag{1.17}$$

$$\nu_\theta = \frac{(\varepsilon_z - \varepsilon_x)\sin\theta\cos\theta}{\nu_{f_{TM}}\varepsilon_z(\varepsilon_x\mu_y + \alpha_{xy}^2)} \tag{1.18}$$

$$v^2_{g_{TM}} = \frac{1}{a_{TM}} \frac{\varepsilon_x^2 \cos^2\theta + \varepsilon_z^2 \sin^2\theta}{\varepsilon_x \cos^2\theta + \varepsilon_z \sin^2\theta}, \quad (1.19)$$

angle β, defining direction v_g is from expression $\tan\beta = \frac{\mu_z}{\mu_x}\tan\theta$ (1.20).

2. Energy-flux density [10-12].

2.1. In the case of TE-polarized waves in (1.7), (1.8) as opposed to zero components:

$$E_y,\ H_z,\ H_x. \quad (2.1)$$

From Maxwell's equations for plane waves we have the following:

$$H_z = \frac{k_x}{\omega\mu_z} E_y \quad (2.2)$$

$$H_x = -\frac{k_z - \omega\alpha_{xy}}{\omega\mu_x} E_y. \quad (2.3)$$

The flux density of the electromagnetic energy of the wave is determined by the Umov-Poynting formula:

$$\vec{S} = \left[\vec{E} \times \vec{H}\right]. \quad (2.4)$$

Based on (2.4) we get the following:

$$S_x = \frac{k_x}{\omega\mu_z} E_y^2 = \frac{k_x}{\omega\mu_z\varepsilon_y} \varepsilon_y E_y^2 \quad (2.5)$$

$$S_z = \frac{k_z - \omega\alpha_{xy}}{\omega\mu_x} E_y^2 = \frac{k_z - \omega\alpha_{xy}}{\omega\mu_x\varepsilon_y} \varepsilon_y E_y^2. \quad (2.6)$$

From the relation S_z / S_x the direction of the energy flux density vector follows:

$$\tan\beta_e = \frac{S_z}{S_x} = \frac{\mu_z}{\mu_x} \frac{k_z - \omega\alpha_{xy}}{k_x}, \quad (2.7)$$

when $\alpha_{xy} = 0$, we get the $\tan\beta_e = \frac{k_z}{k_x}\frac{\mu_z}{\mu_x} = \frac{\mu_z}{\mu_x}\tan\theta$ transition rate, the group velocity is determined by the ratio:

$$v^2_{g_e} = \frac{S^2}{\varepsilon_y^2 E_y^4} = \frac{S_x^2 + S_z^2}{\varepsilon_y^2 E_y^4} = \frac{\mu_x^2 k_x^2 + (k_z - \omega\alpha_{xy})^2 \mu_z^2}{\omega^2 \mu_x^2 \varepsilon_y^2 \mu_z^2}. \quad (2.8)$$

The components of the wave vector k_x *u* k_z are determined on the basis of (1.8) for TE waves and on the basis of formula (1.16) for TM waves.

2.2. When the propagation of TM- polarized waves, the wave field has components:

$$H_y,\ E_z,\ E_x. \quad (2.9)$$

Dependencies are fair:

$$E_z = -\frac{k_x}{\omega\varepsilon_z} H_y \quad (2.10)$$

$$E_x = \frac{k_z + \omega\alpha_{xy}}{\omega\varepsilon_x} H_y \quad (2.11)$$

Based on the Umov-Poynting formula, the S_x *u* S_z components are:

$$S_x = -E_z H_y = \frac{k_x}{\omega\varepsilon_z\mu_y}\mu_y H_y^2 \quad (2.12)$$

$$S_z = E_x H_y = \frac{k_z + \omega\alpha_{xy}}{\omega\varepsilon_x\mu_y}\mu_y H_y^2 \quad (2.13)$$

Direction of energy flow: $\tan\beta_{TM} = \frac{S_z}{S_x} = \frac{\varepsilon_z}{\varepsilon_x}\frac{k_z + \omega\alpha_{xy}}{k_x}$, (2.14)

from (2.12), (2.13) follows the energy transfer rate

$$v_{g_{TM}}^2 = \frac{S_x^2 + S_z^2}{\mu_y^2 H_y^4} = \frac{\varepsilon_x^2 k_x^2 + (k_z + \omega\alpha_{xy})^2\varepsilon_z^2}{\omega^2\varepsilon_x^2\varepsilon_y^2\mu_y^2} \quad (2.15)$$

Results and discussion

The propagation of TE and TM-polarized electromagnetic waves in uniaxial crystals (classes 4 mm, 3m, 6mm) in the presence of the magneto-electric effect has been discussed. The indicatrices of the wave vectors and phase velocities of TE and TM waves propagating in the plane ($x0z$) have been determined. On the basis of the Rayleigh equation, the magnitude and direction of the group velocity and its indicatrix have been determined. The flux density and electromagnetic waves components transferred by TE and TM waves, their directions and transfer rates have been defined. Experience showed that the group velocity and direction obtained on the basis of the Rayleigh equations and angles transfer rate, following from the Umov-Poynting vector disagreed. The research is based on the matrix method [8-9].

References

1 Rivera J.P. A short review of the magnetoelectric effect and related experimental techniques on single phase ferroics / J.P. Rivera // The European Physical Journal B. — 2009. — No. 71. — P. 299-313.

2 Бичурин М.И. Магнитоэлектрические композиционные материалы на основе феррит-пьезоэлектриков. Перспективные материалы / М.И. Бичурин, В.М. Петров, Д.А. Филиппов, Г. Сринивасан, В.М. Лалетин. — 2004. — № 6. — С. 5–12.

3 Филиппов Д.А. Теория магнитоэлектрического эффекта в гетерогенных структурах на основе ферромагнетик-пьезоэлектрик / Д.А. Филиппов // ФТТ. — 2005. — Т. 47, № 6. — С. 1082–1084.

4 Hehl F., Obukhov, Y., Rivera, J. and Schmid, H. // Physics Letters A. — 2008. — No 372. — P. 1141-1148.

5 Tleukenov S.K. Phase and group velocities of electromagnetic waves in a monoclinic crystal / S.K. Tleukenov, Z.K. Zhalgasbekova, Yu.K. Sirenko // Telecommunication and Radio Engineering. — 2019. — Vol. 78(1). — P. 1-10.

6 Тлеукенов С.К. Групповая скорость и поток электромагнитной энергии в ромбических кристаллах / С.К. Тлеукенов, К.Н. Балабеков, З.К. Жалгасбекова // Вестн. Евраз. нац. ун-та им. Л.Н. Гумилева. Сер. Физика. Астрономия. — 2019. — № 1(126). — С. 90–98.

7 Tleukenov S.K. Indicatrices of phase and group velocities of electromagnetic waves in crystals with magnetoelectric effect / S.K. Tleukenov, Zh.N. Suierkulova // Telecommunications and Radio Engineering. — 2019. — Vol. 78(6). — P. 465-473.

8 Гантмахер Ф.Р. Теория матриц / Ф.Р. Гантмахер. — М.: Наука, 1988.

9 Смирнов В.И. Курс высшей математики / В.И. Смирнов. — М.: ГИТТЛ, 1953.

10 Tleukenova S.K. Angles of Refraction and Directions of Group Velocity Vectors of TE and TM Polarization Waves at the Interface between an Isotropic Medium and a Semi-Space with the Magnetoelectric Effect / S.K. Tleukenova, Zh.N. Suierkulova, V.G. Mozhaev // Bulletin of the Russian Academy of Sciences: Physics. — 2020. — Vol. 84, No. 2. — P. 206–209.

11 Тлеукенов С.К. Углы преломления и направления векторов групповых скоростей волн TE и TM поляризации на границе изотропной среды и полупространства с магнитоэлектрическим эффектом / С.К. Тлеукенов, Ж.Н. Суйеркулова, В.Г. Можаев // Изв. РАН. Сер. физ. — 2020. — Т. 84, № 2. — С. 261–265.

12 Tleukenov S.K. Laws of reflection and refraction of TE and TM polarization waves on the border of rhombic crystals / S.K. Tleukenov, K.N. Balabekov, Z.K. Zhalgasbekova // Bulletin of the University of Karaganda-Physics. — 2020. — No 1(97). — P. 70-81.

13 Займан Дж. Принципы теории твердого тела / Дж. Займан. — М.: Мир, 1974. — С. 30.

14 Tleukenov Sadriten. Characteristic matrix of a periodically inhomogeneous layer / Sadriten Tleukenov // Journal of Soviet Mathematics. — 1990. — No 50 (6). — P. 2058-2062.

С.К. Тлеукенов, Ж.Н. Суйеркулова, С.А. Нуркенов

Магнитэлектрлік әсері бар 4mm, 3m, 6mm кристалдық кластардағы TE және TM поляризация толқындарының жылдамдық индикатрисалары

Мақала магнитэлектрлік әсері бар 4mm, 3m, 6mm және т.б. кластарға жататын анизотропты орталарда электрмагниттік толқындардың TM және TM поляризациясының таралу заңдылықтарын теориялық зерттеуге арналған. Магнитэлектрлік қасиеттері бар біросьті кристалдың шекарасындағы TE және TM поляризациялық толқындарының фазалық және топтық жылдамдық векторларының бағыттары қарастырылған. Аналитикалық формада түскен толқынның толқындық векторының бағытына байланысты TE және TM толқындарының фазалық және топтық жылдамдықтарының бағыттарының мәндері көрсетілген. Алынған нәтижелердің магнитэлектрлік қасиеттері болмаған кезде біросьті кристалдар үшін салдары талқыланған. Бұл жұмыс қойылған есептерді шешуде матрицалық әдісті қолдануға негізделген. Оның негізінде бұрын изотропты серпімді ортадағы толқындық процестердің, кристалдардағы электрмагниттік толқындардың, магнитэлектрлік әсері бар пьезоэлектрлік және пьезомагниттік орталарда байланысқан серпімді және электрмагниттік толқындардың таралуының әртүрлі мәселелері қарастырылған. Біросьті кристалдар арқылы таралатын электрмагниттік толқындар үшін магнитэлектрлік әсер болған кезде толқындық вектордың, фазалық және топтық жылдамдықтардың параметрлері анықталды. Нәтижелер магнитэлектрлік әсер болмаған кезде біросьті кристалдар арқылы таралатын электрмагниттік толқындар үшін талданған. Жазықтықта таралатын толқындық векторлардың индикаторлары TE және TM поляризация толқындарының фазалық жылдамдығы шектеулі $(x0z)$. Рэлей теңдеуі негізінде топтық жылдамдық мәндері алынды. Электрмагниттік энергия ағындарының тығыздығы және олардың құрамдас бөліктері TE және TM толқындары үшін анықталған. Энергияның берілу жылдамдығы және оның бағыты айқындалған. Рэлей теңдеуі мен Умов-Пойнтинг векторынан алынған топтық жылдамдықтар мен бағыттар сәйкес келмейтіні көрсетілген.

Кілт сөздер: анизотропия, электрмагниттік толқындар, біросьті кристалдар, магнитэлектрлік әсер, фазалық және топтық жылдамдықтар, TE және TM поляризация толқындары, тығыздық векторы.

С.К. Тлеукенов, Ж.Н. Суйеркулова, С.А. Нуркенов

Индикатрисы скоростей волн TE и TM поляризации в кристаллических классах 4mm, 3m, 6mm с магнитоэлектрическим эффектом

Статья посвящена теоретическому изучению законов распространения электромагнитных волн TE и TM поляризации в анизотропных средах, относящихся к классам 4mm, 3m, 6mm и другим, обладающим магнитоэлектрическим эффектом. Рассмотрены направления векторов фазовой и групповой скоростей поляризационных волн TE и TM на границе одноосного кристалла с магнитоэлектрическими свойствами. В аналитической форме указаны значения направлений фазовой и групповой скоростей волн TE и TM в зависимости от направления волнового вектора падающей волны. Обсуждены последствия полученных результатов для одноосных кристаллов при отсутствии магнитоэлектрических свойств. Решение задач, поставленных в настоящей работе, основано на использовании матричного метода. На его основе ранее рассматривались различные проблемы волновых процессов в изотропной упругой среде, электромагнитных волн в кристаллах, распространения связанных упругих и электромагнитных волн в пьезоэлектрических и пьезомагнитных средах с магнитоэлектрическим эффектом. При наличии магнитоэлектрического эффекта для электромагнитных волн, распространяющихся через одноосные кристаллы, определяются параметры волнового вектора, фазовой и групповой скоростей. Полученные результаты проанализированы для электромагнитных волн, распространяющихся через одноосные кристаллы в отсутствие магнитоэлектрического эффекта. Индикатрисы волновых векторов, распространяющихся в плоскости, и фазовые скорости волн ТЕ и ТМ поляризации ограничены $(x0z)$. На основе уравнения Рэлея получены значения групповой скорости. Плотность потоков электромагнитной энергии и их составляющие определены для волн ТЕ и ТМ. Найдены скорость передачи энергии и ее направление. Показано, что групповые скорости и направления, полученные из уравнения Рэлея и вектора Умова-Пойнтинга, не совпадают.

Ключевые слова: анизотропия, электромагнитные волны, одноосные кристаллы, магнитоэлектрический эффект, фазовая и групповая скорости, волны поляризации ТЕ и ТМ, вектор плотности.

References

1 Rivera, J.P. (2009). A short review of the magnetoelectric effect and related experimental techniques on single phase ferroics. The European Physical Journal B, 71, 299-313.

2 Bichurin, M.I., Petrov, V.M., Filippov, D.A., Srinivasan, G., & Laletin, V.M. (2004). Magnitoelektricheskie kompozitsionnye materialy na osnove ferrit-pezoelektrikov. Perspektivnye materialy — Magnetoelectric composite materials based on ferrite-piezoelectric materials. *Promising Materials, 6,* 5–12 [in Russian].

3 Filippov, D.A. (2005). Teoriia magnitoelektricheskogo effekta v geterogennykh strukturakh na osnove ferromagnetic-pezoelektrik — Theory of the magnetoelectric effect in heterogeneous structures based on a ferromagnet-piezoelectric. *FTT, Vol. 47, 6,* 1082–1084 [in Russian].

4 Hehl F, Obukhov Y, Rivera J & Schmid H. (2008). Physics Letters A. 372, 1141-1148.

5 Tleukenov, S.K., Zhalgasbekova, Z.K., & Sirenko, Yu.K. (2019). Phase and group velocities of electromagnetic waves in a monoclinic crystal. *Telecommunication and Radio Engineering. 78(1),* 1-10.

6 Tleukenov, S.K., Balabekov, K.N., & Zhalgasbekova, Z.K. (2019). Gruppovaia skorost i potok elektromagnitnoi energii v rombicheskikh kristallakh [Group velocity and electromagnetic energy flux in rhombic crystals]. *Vestnik Evraziiskogo natsionalnogo universiteta imeni L.N. Gumileva. Seriia Fizika. Astronomiia — Bulletin of Eurasian National University named after L.N. Gumilyov. Series Physics. Astronomy, 1(126),* 90–98 [in Russian].

7 Tleukenov, S.K., & Suierkulova, Zh.N. (2019). Indicatrices of phase and group velocities of electromagnetic waves in crystals with magnetoelectric effect. *Telecommunications and Radio Engineering, 78(6),* 465-473.

8 Gantmakher, F.R. (1988). Teoriia matrits [Matrix theory]. Moscow: Nauka [in Russian].

9 Smirnov, V.I. (1953). Kurs vysshei matematiki [Higher Mathematics Course]. Moscow: GITTL [in Russian].

10 Tleukenova, S.K., Suierkulova, Zh.N., & Mozhaev, V.G. (2020). Angles of Refraction and Directions of Group Velocity Vectors of TE and TM Polarization Waves at the Interface between an Isotropic Medium and a Semi-Space with the Magnetoelectric Effect. *Bulletin of the Russian Academy of Sciences: Physics, Vol. 84, No. 2,* 206–209.

11 Tleukenov, S.K., Suierkulova, Zh.N., & Mozhaev, V.G. (2020). Ugly prelomleniia i napravleniia vektorov gruppovykh skorostei voln TE i TM poliarizatsii na granitse izotropnoi sredy i poluprostranstva s magnitoelektricheskim effektom [Angles of refraction and directions of vectors of group velocities of TE and TM waves of polarization at the boundary of an isotropic medium and a half-space with a magnetoelectric effect]. *Izvestiia RAN. Seriia fizicheskaia — Proceedings of the Russian Academy of Sciences. Physical series, 84(2),* 261–265 [in Russian].

12 Tleukenov, S.K., Balabekov, K.N., & Zhalgasbekova, Z.K. (2020). Laws of reflection and refraction of TE and TM polarization waves on the border of rhombic crystals. *Bulletin of the University of Karaganda-Physics. 1(97),* 70-81.

13 Zaiman, Dzh. (1974). Printsipy teorii tverdogo tela [Principles of solid state theory]. Moscow: Mir [in Russian].

14 Tleukenov Sadriten (1990). Characteristic matrix of a periodically inhomogeneous layer. *Journal of Soviet Mathematics 50 (6),* 2058-2062.

DOI 10.31489/2023PH1/31-41

UDC 621.3.01

S. Katsyv[1], V. Kukharchuk[1], V. Kucheruk[2], P. Kulakov[2], M. Gribov[3]

[1]*Vinnytsia National Technical University, Vinnytsia, Ukraine;*
[2]*Uman National University of Horticulture, Uman, Ukraine;*
Vinnytsia National Agrarian University, Vinnytsia, Ukraine;
[3]*National Academy of Internal Affairs, Kyiv, Ukraine.*
(E-mail: vladimir.kucheruk@gmail.com)

Nonstandard analysis in electrical engineering. The analysis of the direct current circles with ideal reactive elements.

The article proposes the use of ideas and methods of non-standard analysis in the field of theoretical electronics. The article shows that the analysis of DC circuits, including ideal inductances and capacitances, by standard methods of theoretical electrical engineering is too complicated or almost impossible. To solve this problem, it is proposed to extend the methods of non-standard analysis by the tasks of analyzing electrical circuits with ideal reactive elements. The authors have defined a class of non-standard electrotechnical problems aimed at the analysis of DC electrical circuits, including ideal reactive elements — ideal inductances and capacitances. It is shown that the solution of the selected class of problems by standard methods of theoretical electrical engineering is too difficult or almost impossible. It is proposed to extend the methods of non-standard analysis by the tasks of analyzing electrical circuits with ideal reactive elements. The obtained advantages of this approach are confirmed by examples of calculations of electrical circuits with inductances and capacitances, as well as magnetic circuits.

Keywords: infinitesimal number, infinitude, hyperreal number, unconventional number, ideal reactive element.

Introduction

While solving diverse scientific or technical problems the researcher occasionally faces the necessity of revealing such uncertainties as $\frac{0}{0}$ and $\frac{\infty}{\infty}$. Herewith the use of classical methods, for instance, the rules of Cauchy or L'Hôpital often causes certain difficulties.

It is curious that exactly the ideas of nonstandard analysis (i.e. the direct use of infinitesimal numbers) were the base, on which Leibnitz and Newton intuitively built the principles of differential and integral calculations. However, later in Cauchy's works and in the works of other mathematicians, infinitesimal numbers were "left out" [1-5]. Instead, in the basis of mathematic apparatus of differential and integral calculation numerical and functional sequences and limit correlations of values were laid. That increased the axiomatic rigor of mathematical apparatus, but unfortunately complicated the way of solving a certain kind of problems.

The revival of the ideas of nonstandard analysis took place in 1960-s, when A. Robinson suggested a new axiomatics of math analysis, which bases on the multitude of hyperreal numbers, that contains not only so called reference numbers (common numbers), but also the nonstandard numbers (infinitesimal numbers, infinitudes and their combinations with common numbers) [6-8]. Methods of nonstandard analysis are also being developed at the present time and are used in various fields of science [9-12]. In this article, we will consider the use of nonstandard analysis in electrical engineering. Of interest is the use of nonstandard analysis methods in the problems of identifying the internal parameters of electrical motors, which in many cases cannot be solved by traditional methods [13-18].

For direct current circles, we use diverse unified methods of calculation based on the Ohm's and Kirchhoff's laws. At the same time, there exists a certain kind of related problems, for which the direct use of these unified methods is practically impossible. This concerns the calculation of the direct current circles with ideal reactive elements. The complexity of the calculations in such circles is that on the direct current the induction resistance $\left(x_L = \omega L\right)$ tends to zero, and the ideal capacity $\left(x_C = \frac{1}{\omega C}\right)$ resistance tends to infinity.

Generally, such problems are solved with simultaneous use of the energy characteristics of inductances and capacities alongside with electrical engineering laws, which considerably complicates the analysis of such circuits, especially in complex schemes. That explains the topicality of the math apparatus of nonstandard analysis which will enable to use familiar unified methods for calculating such circles.

The next unit will review the main principles of non-standard analysis necessary for the solution of the above mentioned electrotechnical problems, this mathematic apparatus is considered in [19-20].

Basic principles of nonstandard analysis

Let R be an ordered set of real numbers. Number α will be called an infinitesimal number when and only when

$$\forall r \in R(\alpha < r). \tag{1}$$

The number $\beta = \frac{1}{\alpha}$ will be called infinitude. In this case, it may be transcribed as

$$\forall r \in R(\beta > r). \tag{2}$$

All algebraic operations (addition, subtraction, multiplication, division, exponentiation, etc.) and theorems (theorems of communication and association, etc.) may be applied to infinitesimal and infinitude numbers.

Infinitesimal numbers and infinitudes of diverse order will be distinguished as follows:

- $\alpha > \alpha^2 > \alpha^3 > \alpha^k$ — infinitesimal numbers of first, second, third, k-th order;
- $\beta < \beta^2 < \beta^3 < \beta^k$ — infinitudes of first, second, third, k-th order.

Together with real numbers $r \in R$ infinitesimal numbers and infinitudes make an ordered set of hyperreal numbers $*R$. Real numbers $r \in R$ are commonly called standard or Archimedean numbers unlike imaginary (non-Archimedean) numbers $*r \in *R$.

Each imaginary number has a standard part

$$*r = r \pm \alpha, \tag{3}$$

that is

$$r = st(*r), \tag{4}$$

in other words, a real number is a standard part of a certain imaginary number (obviously, there can be an infinite set of those).

Two real numbers a and b are called equal when and only when:

$$a - b = 0. \tag{5}$$

Two imaginary numbers $*a$ and $*b$ are called equivalent (or infinitely close to each other when and only when:

$$*a - *b \approx \alpha. \tag{6}$$

The marking “$\approx$” will stand for the equivalency of two imaginary numbers. For real numbers m and n we will denote certain correlations that appear from (1-6):

$$\frac{1}{\alpha^k} = \beta^k, \ \frac{m}{\alpha} = m\beta, \ \frac{m}{\alpha^k} = m\beta^k, \tag{7}$$

$$\frac{m\alpha}{n\alpha} = \frac{m}{n}, \ \frac{m\alpha}{n} = \frac{m}{n}\alpha, \ \frac{m}{n\alpha} = \frac{m}{n}\beta, \tag{8}$$

$$m\alpha + n \approx n, \ m\beta + n \approx m\beta, \ m\alpha^k + n \approx n, \ m\beta^k + n \approx m\beta^k, \tag{9}$$

$$\sin\alpha \approx \alpha, \ \cos\alpha \approx 1. \tag{10}$$

We will give a few examples of using these methods in a mathematic analysis. For instance, let us find the first derivative of the function $y = x^3$. For that purpose, we will input a substitution $dx = \alpha$.

$$\frac{dy}{dx}=\frac{(x+\alpha)^3-x^3}{\alpha}=\frac{x^3+3x^2\alpha+3x\alpha^2+\alpha^3-x^3}{\alpha}=3x^2+3x\alpha+\alpha^2\approx 3x^2. \quad (11)$$

For $y=\sin x$ we will get

$$\frac{dy}{dx}=\frac{\sin(x+\alpha)-\sin x}{\alpha}=\frac{\sin x\cdot\cos\alpha+\sin\alpha\cdot\cos x-\sin x}{\alpha}\approx$$
$$\approx\frac{\sin x\cdot 1+\alpha\cdot\cos x-\sin x}{\alpha}\approx\cos x. \quad (12)$$

Let $y=\cos x$. Then

$$\frac{dy}{dx}=\frac{\cos(x+\alpha)-\cos x}{\alpha}=\frac{\cos x\cdot\cos\alpha-\sin x\cdot\sin\alpha-\cos x}{\alpha}\approx$$
$$\approx\frac{\cos x\cdot 1-\sin x\cdot\alpha-\cos x}{\alpha}\approx-\sin x. \quad (13)$$

It is quite natural, that not only a multitude of real numbers might have such a nonstandard structure, but also the multitude of imaginary numbers can, i.e. the complex number plane.

Then, analogically to (9) we may transcribe

$$m\alpha+jn\approx jn,\ m\beta+jn\approx m\beta,\ m+jn\alpha\approx m,\ m+jn\beta\approx jn\beta. \quad (14)$$

Besides, the problems of classical analysis of transitive processes call for the direct use of the real number 0 and the infinite value ∞. That is why, we will try to formulate their nonstandard interpretation.

Real number 0 in the nonstandard analysis may be considered as infinitesimal number of infinite order, i.e. $0\approx\alpha^{\beta}$. That is why

$$\frac{0}{\alpha}\approx 0,\ 0\cdot\beta\approx 0,\ e^{-\beta\cdot 0}\approx 1,\ e^{-\alpha}\approx 1. \quad (15)$$

Infinite value ∞ in non-standard analysis may be introduced as infinitude of infinite order, i.e. $\infty\approx\beta^{\beta}$. That is why

$$\frac{\infty}{\beta}\approx\infty,\ \infty\cdot\alpha\approx\infty,\ e^{-\infty\cdot\alpha}\approx\alpha,\ e^{-\beta}\approx\alpha. \quad (16)$$

Before going on to use above given expressions for solving diverse applied problems, it is suffice to notice, that there are no general rules for parameter selection, which can be advisably equated to an infinitesimal (or infinitude) number. The researcher depending on the context of the peculiar problem makes this selection. Herewith, one must consider that in case of necessity to substitute for a few different options of one problem with infinitesimals, defining correlations between these numbers is quite an uneasy task to do and may require additional researches.

In the next subparagraph, we suggest considering the ways of using the methods of nonstandard analysis for analyzing the direct current circuits with ideal reactive elements.

Viewing the direct current circuit as a sinusoid alternating current circuit, the frequency of which equals to zero, a symbolic method may be used for solving such problems, given $\omega=\alpha$.

Let us consider the typical examples of such problems.

The analysis of direct current electrical circuits with ideal inductances.

Taking $\omega=\alpha$ for impedance of inductance it may be transcribed as follows:

$$\underline{Z}_L\approx j\alpha L. \quad (17)$$

Example 1. Determine the currents in inductances L_1, L_2 in the direct current circuit (Fig. 1).

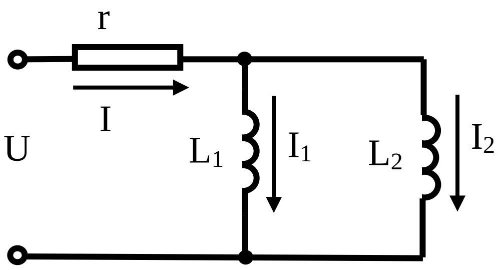

Figure 1. Direct current circuit

Scheme options: $U = 30$ V, $r = 10$ Ω, $L_1 = 0.2$ H, $L_2 = 0.1$ H. At first, it seems that the currents in inductances are the same $I_1 = I_2 = \frac{I}{2} = \frac{U}{2r} = 1.5$. As far as the resistances of these branches on the direct current amount to zero. However, let us try to solve this problem using infinitesimals.

The whole impedance of the circuit equals to

$$\underline{Z}_{in} \approx r + \frac{(j\alpha L_1)(j\alpha L_2)}{j\alpha L_1 + j\alpha L_2} = r + \frac{j^2\alpha^2 L_1 L_2}{j\alpha(L_1 + L_2)} = r + j\alpha\frac{L_1 L_2}{(L_1 + L_2)}, \tag{18}$$

and according to (14) $\underline{Z}_{in} \approx r$. Hence, $\underline{I} = \frac{U}{r} = 3$ and the inductance voltage is

$$\underline{U}_L = j\alpha\frac{L_1 L_2}{(L_1 + L_2)}\underline{I} = \frac{U}{r}j\alpha\frac{L_1 L_2}{(L_1 + L_2)}, \tag{19}$$

while the currents in the branches are:

$$\underline{I}_1 = \frac{\underline{U}_L}{j\alpha L_1} = \frac{UL_2}{(L_1 + L_2)r} = 1 \text{ A}, \ \underline{I}_2 = \frac{\underline{U}_L}{j\alpha L_2} = \frac{UL_1}{(L_1 + L_2)r} = 2 \text{ A}. \tag{20}$$

It shows that the total current I at the inlet to the circuit is split between inductances is no way the same, but inversely to their meanings.

Even more curious is the case, where in this circuit there is a magnetic coupling between both inductive coils.

Example 2. If both coils are switched on coordinately (Fig. 2), the system of equations according to Kirchhoff laws will look as follows:

$$\underline{I} - \underline{I}_1 - \underline{I}_2 = 0, \tag{21}$$

$$\underline{I}r + \underline{I}_1 j\alpha L_1 + \underline{I}_2 j\alpha M = U, \tag{22}$$

$$\underline{I}_1 j\alpha L_1 + \underline{I}_2 j\alpha M = \underline{I}_2 j\alpha L_2 + \underline{I}_1 j\alpha M. \tag{23}$$

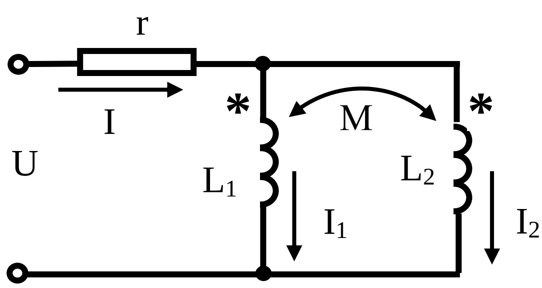

Figure 2. Circuit with magnetic coupling between both inductive coils

For the other equation of this system, we will carry out the equivalent conversions according to (10):

$$\underline{I}r + \underline{I}_1 j\alpha L_1 + \underline{I}_2 j\alpha M \approx \underline{I}r = U. \tag{24}$$

Hence $\underline{I} = \dfrac{U}{r} = 3$ A. In this way, we have obtained a new system of equations:

$$\frac{U}{r} - \underline{I}_1 - \underline{I}_2 = 0, \tag{25}$$

$$\underline{I}_1 j\alpha L_1 + \underline{I}_2 j\alpha M = \underline{I}_2 j\alpha L_2 + \underline{I}_1 j\alpha M. \tag{26}$$

Let us determine current $\underline{I}_1$ from the first equation and substitute it into the second equation:

$$\underline{I}_1 = \frac{U}{r} - \underline{I}_2, \tag{27}$$

$$\left(\frac{U}{r} - \underline{I}_2\right) j\alpha L_1 + \underline{I}_2 j\alpha M = \underline{I}_2 j\alpha L_2 + \left(\frac{U}{r} - \underline{I}_2\right) j\alpha M. \tag{28}$$

Hence,

$$\frac{U}{r} j\alpha L_1 - \underline{I}_2 j\alpha L_1 + \underline{I}_2 j\alpha M = \underline{I}_2 j\alpha L_2 + \frac{U}{r} j\alpha M - \underline{I}_2 j\alpha M, \tag{29}$$

$$\frac{U}{r}\left(j\alpha L_1 - j\alpha M\right) = \underline{I}_2\left(j\alpha L_1 + j\alpha L_2 - 2j\alpha M\right), \tag{30}$$

$$\underline{I}_2 = \frac{\frac{U}{r}\left(j\alpha L_1 - j\alpha M\right)}{\left(j\alpha L_1 + j\alpha L_2 - 2j\alpha M\right)} = \frac{U\left(L_1 - M\right)}{r\left(L_1 + L_2 - 2M\right)}, \tag{31}$$

$$\underline{I}_1 = \frac{U}{r} - \underline{I}_2 = \frac{U}{r} - \frac{U\left(L_1 - M\right)}{r\left(L_1 + L_2 - 2M\right)} = \frac{U\left(L_2 - M\right)}{r\left(L_1 + L_2 - 2M\right)}. \tag{32}$$

We will perform numerical calculations for three typical cases of correlation between self-inductance L_1, L_2 and mutual inductance M (values L_1, L_2 are the same as those in the previous example):

1. Let $M = 0.08$ H, i.e. $M < L_2$. Hence, $\underline{I}_1 = 0.429$ A, and $\underline{I}_2 = 2.571$ A. This case does not differ significantly from the previous example.
2. Let take $M = 0.1$ H, i.e. $M = L_2$. In this case, the whole current flows in the second coil ($\underline{I}_2 = 3$ A), while in the first one it disappears ($\underline{I}_1 = 0$ A).

The most curious is the third case $M = 0.14$ H, when $L_2 < M < \sqrt{L_1 L_2}$. Here we observe a very distinct so-called "false capacity effect", when the currents in each coil surpass the input current ($\underline{I}_1 = -6$ A, $\underline{I}_2 = 9$ A), and more to that, in the first coil the current changes its direction.

Suffice it to notice, that this problem is very hard to solve without methods of nonstandard analysis, and for the next problem it is almost impossible.

Example 3. In the direct current circuit (Fig. 3) determine the currents in all of the branches.

Scheme parameters: $U = 100$ V, $r = 10$ Ω, $L_1 = 0.2$ H, $L_2 = 0.15$ H, $L_3 = 0.1$ H, $L_4 = 0.05$ H, $L_5 = 0.025$ H.

Let us carry out this calculation with a loop current method.

By analogy to the previous examples, it is obvious that the input impedance of this circuit also equals to resistor impedance, i.e. $\underline{Z}_{in} \approx r$.

Hence, the loop current of the first loop is known:

$$\underline{I}_{11} = \frac{U}{r} = 10 \text{ A}, \tag{33}$$

and the equation system will look as follows

$$\underline{I}_{11}\underline{Z}_{21} + \underline{I}_{22}\underline{Z}_{22} + \underline{I}_{33}\underline{Z}_{23} = 0, \quad (34)$$

$$\underline{I}_{11}\underline{Z}_{31} + \underline{I}_{22}\underline{Z}_{32} + \underline{I}_{33}\underline{Z}_{33} = 0. \quad (35)$$

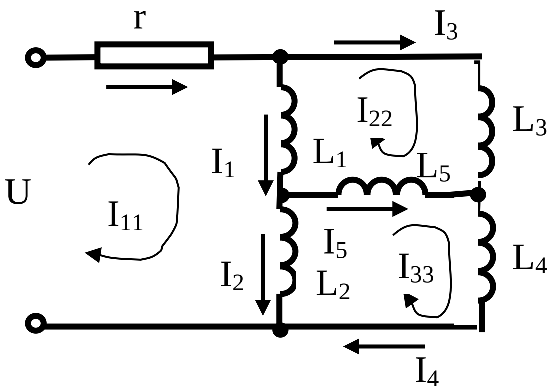

Figure 3. Circuit with detection of currents in all branches

Substituting expressions for the first loop current and as well as for loop and joint impedances, we will get

$$\frac{U}{r}(-j\alpha L_1) + \underline{I}_{22}(j\alpha L_1 + j\alpha L_3 + j\alpha L_5) + \underline{I}_{33}(-j\alpha L_5) = 0, \quad (36)$$

$$\frac{U}{r}(-j\alpha L_2) + \underline{I}_{22}(-j\alpha L_5) + \underline{I}_{33}(j\alpha L_2 + j\alpha L_4 + j\alpha L_5) = 0. \quad (37)$$

Let us define the third loop current from the first equation and substitute it into the second equation.

$$\underline{I}_{33} = \frac{\frac{U}{r}(-j\alpha L_1) + \underline{I}_{22}(j\alpha L_1 + j\alpha L_3 + j\alpha L_5)}{j\alpha L_5} =$$

$$= \frac{\underline{I}_{22}(L_1 + L_3 + L_5) - \frac{U}{r}L_1}{L_5} = \underline{I}_{22}\frac{L_1 + L_3 + L_5}{L_5} - \frac{UL_1}{rL_5}, \quad (38)$$

$$\frac{U}{r}(-j\alpha L_2) + \underline{I}_{22}(-j\alpha L_5) + \left(\underline{I}_{22}\frac{L_1 + L_3 + L_5}{L_5} - \frac{UL_1}{rL_5}\right)(j\alpha L_2 + j\alpha L_4 + j\alpha L_5) =$$

$$= \underline{I}_{22}\left[\frac{L_1 + L_3 + L_5}{L_5}(j\alpha L_2 + j\alpha L_4 + j\alpha L_5) - j\alpha L_5\right] - \frac{UL_1}{rL_5}(j\alpha L_2 + j\alpha L_4 + j\alpha L_5) - \frac{U}{r}j\alpha L_2 = 0 \quad (39)$$

Hence, we determine loop currents

$$\underline{I}_{22} = \frac{\frac{UL_1}{rL_5}(j\alpha L_2 + j\alpha L_4 + j\alpha L_5) + \frac{U}{r}j\alpha L_2}{\frac{L_1 + L_3 + L_5}{L_5}(j\alpha L_2 + j\alpha L_4 + j\alpha L_5) - j\alpha L_5} =$$

$$= \frac{\frac{UL_1}{rL_5}(L_2 + L_4 + L_5) + \frac{U}{r}L_2}{\frac{L_1 + L_3 + L_5}{L_5}(L_2 + L_4 + L_5) - L_5} = 6.724 \text{ A}, \quad (40)$$

$$\underline{I}_{33} = \frac{\frac{UL_1}{rL_5}\left(L_2 + L_4 + L_5\right) + \frac{U}{r}L_2}{\frac{L_1 + L_3 + L_5}{L_5}\left(L_2 + L_4 + L_5\right) - L_5}\frac{L_1 + L_3 + L_5}{L_5} - \frac{UL_1}{rL_5} = 7.414 \text{ A}. \quad (41)$$

Henceforward it is easy to determine currents in the branches:

$$\underline{I}_1 = \underline{I}_{11} - \underline{I}_{22} = 3.276 \text{ A}, \; \underline{I}_2 = \underline{I}_{11} - \underline{I}_{33} = 2.586 \text{ A}, \quad (42)$$

$$\underline{I}_3 = \underline{I}_{22} = 6.724 \text{ A}, \; \underline{I}_4 = \underline{I}_{33} = 7.414 \text{ A}, \; \underline{I}_5 = \underline{I}_{33} - \underline{I}_{22} = 0.69 \text{ A}. \quad (43)$$

Suffice it to note, that the usage of ideas of nonstandard analysis allows using any standard methods of electrical circuit calculation.

Let us now consider ideal capacity circuits.

Analysis of electrical direct current circuits of ideal capacities

It is obvious, in such cases for capacity complex impedance we may write down

$$\underline{Z}_C \approx \frac{1}{j\alpha C}. \quad (44)$$

Example 4. Define voltages on the capacities C_1, C_2 in the direct current circuit (Fig. 4).

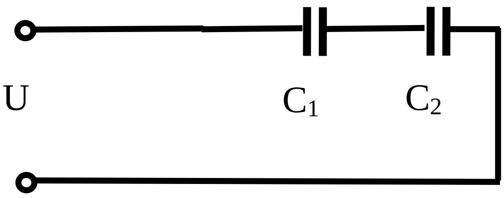

Figure 4. Circuit with capacitances

Let us consider this circuit as a sinusoidal alternating current circuit with $\omega = \alpha$ angular frequency.

Full circuit complex impedance is

$$\underline{Z}_{in} \approx \frac{1}{j\alpha C_1} + \frac{1}{j\alpha C_2} = \frac{j\alpha C_1 + j\alpha C_2}{\left(j\alpha C_1\right)\left(j\alpha C_2\right)} = \frac{C_1 + C_2}{j\alpha C_1 C_2}, \quad (45)$$

hence, the current flowing through it is

$$\underline{I} = \frac{U}{\underline{Z}_{in}} = \frac{Uj\alpha C_1 C_2}{C_1 + C_2}, \quad (46)$$

whence the voltages on capacities correspondently equate to

$$U_{C_1} = \underline{I}\frac{1}{j\alpha C_1} = \frac{UC_2}{C_1 + C_2}, \; U_{C_2} = \underline{I}\frac{1}{j\alpha C_2} = \frac{UC_1}{C_1 + C_2}. \quad (47)$$

Example 5. In direct current circuit (Fig. 5) define voltages on all capacities. Circuit parameters: $U = 100$ V, $C_1 = 200\,\mu$F, $C_2 = 150$ μF, $C_3 = 100$ μF, $C_4 = 50$ μF, $C_5 = 25$ μF. The given problem is conveniently solved by the method of node potentials, taking the node 4 as a primary one, that is $\varphi_4 = 0$. Since $\varphi_1 = U$, the problem will be reduced to the system of 2 equations.

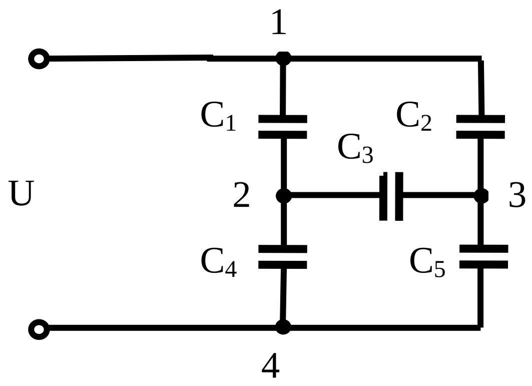

Figure 5. Circuit with five capacitors

Let us transcribe the system of equations

$$-\underline{\varphi}_1\underline{Y}_{21}+\underline{\varphi}_2\underline{Y}_{22}-\underline{\varphi}_3\underline{Y}_{23}=0, \quad (48)$$

$$-\underline{\varphi}_1\underline{Y}_{31}-\underline{\varphi}_2\underline{Y}_{32}+\underline{\varphi}_3\underline{Y}_{33}=0. \quad (49)$$

By substituting the expressions for first node potential as well as for the self- and mutual conductance, we will get

$$-U(j\alpha C_1)+\underline{\varphi}_2(j\alpha C_1+j\alpha C_4+j\alpha C_3)-\underline{\varphi}_3(j\alpha C_3)=0, \quad (50)$$

$$-U(j\alpha C_2)-\underline{\varphi}_2(j\alpha C_3)+\underline{\varphi}_3(j\alpha C_2+j\alpha C_3+j\alpha C_5)=0. \quad (51)$$

Let us determine the second node potential from the first equation and substitute it into the second one.

$$\underline{\varphi}_2=\frac{U(j\alpha C_1)+\underline{\varphi}_3(j\alpha C_3)}{j\alpha C_1+j\alpha C_4+j\alpha C_3}=\frac{UC_1+\underline{\varphi}_3C_3}{C_1+C_4+C_3}, \quad (52)$$

$$-U(j\alpha C_2)-\frac{UC_1+\underline{\varphi}_3C_3}{C_1+C_4+C_3}(j\alpha C_3)+\underline{\varphi}_3(j\alpha C_2+j\alpha C_3+j\alpha C_5)=$$

$$=-U(j\alpha C_2)-\frac{UC_1(j\alpha C_3)}{C_1+C_4+C_3}-\frac{\underline{\varphi}_3C_3}{C_1+C_4+C_3}(j\alpha C_3)+\underline{\varphi}_3(j\alpha C_2+j\alpha C_3+j\alpha C_5)=0\Leftrightarrow$$

$$\Leftrightarrow -U(C_2)-\frac{UC_1(C_3)}{C_1+C_4+C_3}-\frac{\underline{\varphi}_3C_3}{C_1+C_4+C_3}(C_3)+\underline{\varphi}_3(C_2+C_3+C_5)=0 \quad (53)$$

Hence, the potentials are:

$$\underline{\varphi}_3=\frac{UC_2+\dfrac{UC_1C_3}{C_1+C_4+C_3}}{C_2+C_3+C_5-\dfrac{C_3^2}{C_1+C_4+C_3}}=81.159\ \text{V}, \quad (54)$$

$$\underline{\varphi}_2=\frac{UC_1}{C_1+C_4+C_3}+\frac{UC_2+\dfrac{UC_1C_3}{C_1+C_4+C_3}}{C_2+C_3+C_5-\dfrac{C_3^2}{C_1+C_4+C_3}}\frac{C_3}{C_1+C_4+C_3}=84.058\ \text{V}. \quad (55)$$

Henceforward it is easy to find voltages in capacities:

$$U_{C_1}=\underline{\varphi}_1-\underline{\varphi}_2=18.841\ \text{V},\ U_{C_2}=\underline{\varphi}_1-\underline{\varphi}_3=15.942\ \text{V},\ U_{C_3}=\underline{\varphi}_3-\underline{\varphi}_2=2.899\ \text{V}, \quad (56)$$

$$U_{C_4}=\underline{\varphi}_2=81.159\ \text{V},\ U_{C_5}=\underline{\varphi}_3=84.058\ \text{V}. \quad (57)$$

Conclusions

1. The authors are the first to determine the class of nonstandard electrical engineering problems, aimed at analysing direct current electrical circuits, which include ideal reactive elements — ideal inductances and capacities. It is shown, that the solution of the highlighted class of problems through standard methods of theoretical electrical engineering is far too complex or almost impossible.

2. To solve the described problem it is proposed to extend the methods of nonstandard analysis with the problems of analysis of electrical circuits with ideal reactive elements. The advantages of this approach are proved by the examples of calculations of electrical circuits with inductances and capacities and as well of magnetic bound circuits.

3. With the aim of extending the sphere of usage of the methods of nonstandard analysis it is important to distinguish similar problems from diverse spheres of science and engineering, where differential calculation and extreme transitions are used and the solution of which with standard approaches is limited or impossible.

References

1 Donaldson J.A. The abstract Cauchy problem / J.A. Donaldson // Journal of Differential Equations. — 1977. — Vol. 25. — Iss. 3. — P. 400-409.

2 De Laubenfels R. Entire solutions of the abstract Cauchy problem / R. De Laubenfels // Semigroup Forum. — 1991. — Vol. 42. — P. 83–105.

3 Vedmitskyi Y.G. Newton binomial in the generalized Cauchy problem as exemplified by electrical systems / Y.G. Vedmitskyi, V.V. Kukharchuk, V.F. Hraniak, I.V. Vishtak, P. Kacejko, A. Abenov // Proc. SPIE 10808, Photonics Applications in Astronomy, Communications, Industry, and High Energy Physics Experiments. — 2018. — Vol. 108082M.

4 Zhen Wang. Uniqueness of generalized solution for the Cauchy problem of transportation equations / Wang Zhen, Ding Xiaqi // Acta Mathematica Scientia. — 1997. — Vol. 17. — Issue 3. — P. 341-352.

5 Sanchez-Ortiz. Cauchy Problem for a Stochastic Fractional Differential Equation with Caputo-Itô Derivative / Sanchez-Ortiz, Jorge, Omar U. Lopez-Cresencio, Francisco J. Ariza-Hernandez, P. Martin // Mathematics. — 2021. — V. 9. — P. 1-10.

6 Робинсон А. Введение в теорию моделей и математику алгебры / А. Робинсон. — М.: Наука, 1967. — 376 с.

7 Robinson A. Non-Standard Analysis / A. Robinson— Princeton: Princeton University Press. — 1996. — 308 p.

8 Jensen A. A computer oriented approach to “nonstandard analysis” / A. Jensen // Studies in Logic and the Foundations of Mathematics. — 1972. — Vol. 69. — P. 281-289.

9 Девис М. Прикладной нестандартный анализ / М. Девис; пер. с англ. — М.: Мир, 1980. — 240 с.

10 Гордон Е.И. Инфинитезимальный анализ / Е.И. Гордон, А.Г. Кусраев, С.С. Кутателадзе. — Новосибирск: Изд-во Ин-та математики, 2001. — 526 с.

11 Bell J. A Primer of Infinitesimal Analysis / J. Bell. — Cambridge University Press. — 1998. — 140 p.

12 Lutz R. Nonstandard Analysis. A Practical Guide with Applications / R. Lutz, M. Goze. — Berlin: Springer-Verlag. — 1981. — 261 p.

13 IEEE Standard Test Procedure for Polyphase Induction Motors and Generators. IEEE Std 112–2004 from 12th May 2004 (Revision of IEEE Std 112–1996). New York: American National Standard Institute.

14 Kucheruk V.Yu. Computer-measuring system of the induction motor’s dynamical torque-speed characteristics / V.Yu. Kucheruk, I.P. Kurytnik, Ye.Z. Oshanov, P.I. Kulakov, A.A. Semenov, D.Zh. Karabekova, A.K. Khassenov // Bulletin of the University of Karaganda-Physics. — 2019. — Vol. 2(94). — P. 92–100.

15 Hraniak V.F. Phase noncontact method and procedure for measurement of axial displacement of electric machine’s rotor / V.F. Hraniak, V.V. Kukharchuk, V.V. Bogachuk, Yu.G. Vedmitskyi // Proc. SPIE 10808, Photonics Applications in Astronomy, Communications, Industry, and High-Energy Physics Experiments. — 2018, Vol. 1080866.

16 Aree P. Analytical approach to determine speed-torque curve of induction motor from manufacturer data / P. Aree // Procedia Computer Science. — 2016. — Vol. 86. — p. 293–296.

17 Pfingsten G. Highly efficient approach to the simulation of variable-speed induction motor drives / G. Pfingsten, K. Hameyer // Science Measurement & Technology IET. — 2017. — Vol. 11. — P. 793–801.

18 Kojooyan-Jafari H. Parameter Estimation of Wound-Rotor Induction Motors from Transient Measurements / H. Kojooyan-Jafari, L. Monjo, F. Corcoles, J. Pedra // IEEE Transactions on Energy Conversion. — 2014. — Vol. 29. — P. 300–308.

19 Karpov Yu.O. Rozshyrennia oblasti zastosuvannia symvolnoho metodu otsinky elektrychnykh kil za dopomohoiu metodiv nestandartnoho analizu (chastyna 1) / Yu.O. Karpov, S.Sh. Katsyv, A.V. Kozlovskyi // Visnyk Inzhenernoi akademii Ukrainy. — 2013. — Vyp. 1. — S. 236-239.

20 Karpov Yu.O. Rozshyrennia oblasti zastosuvannia symvolnoho metodu otsiniuvannia elektrychnykh kil za dopomohoiu metodiv nestandartnoho analizu (chastyna 2) / Yu.O. Karpov, S.Sh. Katsyv, A.V. Kozlovskyi // Visnyk Inzhenernoi akademii Ukrainy. — 2013. — Vyp. 2. — S. 262-265.

С. Кацыв, В. Кухарчук, В. Кучерук, П. Кулаков, М. Грибов

Электртехникадағы стандарттыемес талдау. Идеал реактивті элементтері бар тұрақты ток тізбектерін талдау

Мақалада теориялық электроника саласындағы стандарттыемес талдау идеялары мен әдістерін қолдану ұсынылған. Идеалды индуктивтілік пен сыйымдылықты қамтитын тұрақты ток тізбектерін талдау теориялық электртехниканың стандартты әдістерімен тым күрделі немесе мүмкін емес екендігі көрсетілген. Бұл мәселені шешу үшін стандарттыемес талдау әдістерін идеалды реактивті элементтері бар электр тізбектерін талдау мәселелерімен кеңейту ұсынылған. Авторлар идеалды реактивті элементтерді — идеалды индуктивтілік пен сыйымдылықты қамтитын тұрақты токтың электр тізбектерін талдауға бағытталған стандартты емес электротехникалық есептер класын анықтады. Арнайы есептер класын теориялық электртехниканың стандартты әдістерімен шешу өте қиын немесе мүмкін емес екендігі көрсетілген. Стандартты емес талдау әдістерін идеалды реактивті элементтері бар электр тізбектерін талдау міндеттерімен кеңейту ұсынылды. Бұл тәсілдің алынған артықшылықтары индуктивтілігі мен сыйымдылығы бар электр тізбектерін, сондай-ақ магниттік өткізгіштерді есептеу мысалдарымен расталады.

Кілт сөздер: шексіз аз сан, шексіздік, гипернақты сан, дәстүрліемес сан, идеал реактивті элемент.

С. Кацыв, В. Кухарчук, В. Кучерук, П. Кулаков, М. Грибов

Нестандартный анализ в электротехнике. Анализ контуров постоянного тока с идеальными реактивными элементами

В статье предложено использование идей и методов нестандартного анализа в области теоретической электроники. Показано, что анализ цепей постоянного тока, включающих идеальные индуктивности и емкости, стандартными методами теоретической электротехники слишком сложен или почти невозможен. Для решения этой проблемы предложено расширить методы нестандартного анализа задачами анализа электрических цепей с идеальными реактивными элементами. Авторы определили класс нестандартных электротехнических задач, направленных на анализ электрических цепей постоянного тока, включающих в себя идеальные реактивные элементы — идеальные индуктивности и емкости. Показано, что решение выделенного класса задач стандартными методами теоретической электротехники слишком сложно или почти невозможно. Предложено расширить методы нестандартного анализа задачами анализа электрических цепей с идеальными реактивными элементами. Полученные преимущества такого подхода подтверждаются примерами расчетов электрических цепей с индуктивностями и емкостями, а также магнитопроводов.

Ключевые слова: бесконечно малое число, бесконечность, гипердействительное число, нетрадиционное число, идеальный реактивный элемент.

References

1 Donaldson, J.A. (1977). The abstract Cauchy problem. *Journal of Differential Equations, 25(3),* 400-409.

2 De Laubenfels, R. (1991) Entire solutions of the abstract Cauchy problem. *Semigroup Forum, 42,* 83–105.

3 Vedmitskyi, Y.G., Kukharchuk, V.V., Hraniak, V.F., Vishtak, I.V., Kacejko, P., & Abenov, A. (2018). Newton binomial in the generalized Cauchy problem as exemplified by electrical systems. *Proc. SPIE 10808, Photonics Applications in Astronamy, Communications, Industry, and High Energy Physics Experiments,* 108082M.

4 Zhen Wang, & Xiaqi Ding (1997). Uniqueness of generalized solution for the Cauchy problem of transportation equations. *Acta Mathematica Scientia. 17(3),* 341-352.

5 Sanchez-Ortiz, Jorge, Omar, U. Lopez-Cresencio, Francisco, J. Ariza-Hernandez, & Martin, P. (2021). Cauchy Problem for a Stochastic Fractional Differential Equation with Caputo-Itô Derivative. *Mathematics, 9,* 1-10.

6 Robinson, A. (1967). *Vvedenie v teoriiu modelei i matematiki algebry [Introduction into the theory of models and mathematics of algebra].* Moscow: Nauka [in Russian].

7 Robinson, A. (1996). Non-Standard Analysis. Princeton: Princeton University Press.

8 Jensen, A. (1972). A computer oriented approach to “nonstandard analysis, *Studies in Logic and the Foundations of Mathematics, 69,* 281-289.

9 Devis, M. (1980). *Prikladnoi nestandartnyi analiz [Applied non-standard analysis].* Moscow: Mir [in Russian].

10 Gordon, E.Y., Kusraev, A.G., & Kutateladze, S.S. (2001). Infinitezimalnyi analiz [Infinitesimal Analysis]. Novosibirsk: Izdatelstvo Instituta matematiki [in Russian].

11 Bell, J. (1998). A Primer of Infinitesimal Analysis. Cambridge University Press.

12 Lutz, R., & Goze, M. (1981). Nonstandard Analysis. A Practical Guide with Applications. Berlin: Springer-Verlag.

13 IEEE Standard Test Procedure for Polyphase Induction Motors and Generators (2004). IEEE Std 112–2004 from 12th May 2004 (Revision of IEEE Std 112–1996). New York: American National Standard Institute.

14 Kucheruk, V.Yu., Kurytnik, I.P., Oshanov, Ye.Z., Kulakov, P.I., Semenov, A.A., Karabekova, D.Zh., & Khassenov, A.K. (2019). Computer-measuring system of the induction motor's dynamical torque-speed characteristics. *Bulletin of the University of Karaganda-Physics, 2(94),* 92–100.

15 Hraniak, V.F., Kukharchuk, V.V., Bogachuk, V.V., & Vedmitskyi, Yu.G. (2018). Phase noncontact method and procedure for measurement of axial displacement of electric machine's rotor. *Proc. SPIE 10808, Photonics Applications in Astronomy, Communications, Industry, and High-Energy Physics Experiment*s, *1080866*.

16 Aree, P. (2016). Analytical approach to determine speed-torque curve of induction motor from manufacturer data. *Procedia Computer Science, 86,* 293–296.

17 Pfingsten, G., & Hameyer, K. (2017). Highly efficient approach to the simulation of variable-speed induction motor drives. *Science Measurement & Technology IET*, *11,* 793–801.

18 Kojooyan-Jafari, H., Monjo, L., Corcoles, F., & Pedra, J. (2014). Parameter Estimation of Wound-Rotor Induction Motors from Transient Measurements. *IEEE Transactions on Energy Conversion*, *29,* 300–308.

19 Karpov. Yu.O., Katsyv, S.Sh., & Kozlovskyi, A.V. (2013). Rozshyrennia oblasti zastosuvannia symvolnoho metodu otsinky elektrychnykh kil za dopomohoiu metodiv nestandartnoho analizu (chastyna 1) [Expanding the domain of applying a symbolic method of estimation of electric circuits through the methods of non-standard analysis (Part 1)]. *Visnyk Inzhenernoi akademii Ukrainy — Bulletin of the Engineering Academy of Ukraine*, *1,* 236-239 [in Ukrainian].

20 Karpov, Yu.O., Katsyv, S.Sh., & Kozlovskyi, A.V. (2013). Rozshyrennia oblasti zastosuvannia symvolnoho metodu otsiniuvannia elektrychnykh kil za dopomohoiu metodiv nestandartnoho analizu (chastyna 2) [Expanding the domain of applying a symbolic method of estimation of electric circuits through the methods of non-standard analysis (Part 2)]. *Visnyk Inzhenernoi akademii Ukrainy — Bulletin of the Engineering Academy of Ukraine*, *2,* 262-265 [in Ukrainian].

DOI 10.31489/2023PH1/42-48

UDC 621.548.2

A.Zh. Tleubergenova[1], N.K. Tanasheva[1], K.M. Shaimerdenova[1], N.K. Botpaev[1], L.L. Minkov [2], S.B. Kassiyev[1]

[1] *Karaganda University of the name of academician E.A. Buketov, Karaganda, Kazakhstan;*
[2] *National Research Tomsk State University, Tomsk, Russia*
(e-mail: shymkent.a7@mail.ru)

Investigation of Aerodynamic Characteristics of a Two-Bladed Sailing Wind Turbine

The article examines a prototype of a wind turbine with two blades. For experimental work, a mock-up of a sailing wind turbine consisting of two blades was developed. The material of the sail blades was selected according to elasticity and lightness, cheapness, roughness of the streamlined surfaces. The study shows the aerodynamic parameters acting on the blade. The air flow velocity varied from 3 to 12 m/s. The dependence of the lifting force and the frontal barrier on the air flow velocity was obtained by turning the blades of the wind turbine so that the angle of attack was α = 00, 150, 300, 450, 600. It is established that when the position of the blade's changes, the lifting force and the drag force decrease. With an increase in the angle of attack α > 00 leads to a decrease in the midsection of the wind wheel with respect to the air flow. On this basis, there is a decrease in aerodynamic forces. As the speed of the air treacle increases, the speed of rotation of the wind wheel also increases. However, during the experiment it was found that the location of the blades at different angles affects the numerical value of the rotational speed. According to the conducted experiments, several values were obtained. The analysis of the obtained values is carried out. A graph is constructed based on the dependence of the wind wheel rotation frequency on the wind speed with a change in the angle of attack. A wind turbine with blades with a variable angle of attack, which, turning, gradually become more parallel to the direction of the wind. Centrifugal forces regulate the inclination of the blades, and as a result, the speed of rotation of the wind wheel, and keep the wind generator at the nominal speed of rotation.

Keywords: lifting force, wind power plant, drag force, angle of attack, wind speed, rotational speed.

Introduction

The limited fuel reserves in the world by the end of the twentieth century led to a revival of interest in wind energy, which is almost endless.

It is important for Kazakhstan to develop environmentally friendly energy technologies to avoid environmental pollution caused by coal-fired power plants. In addition, the development of renewable energy sources diversifies the economic and energy sectors of the country, while improving the environment and human health. The climate in Kazakhstan is favorable for the construction of wind power plants due to the presence of wind corridors with a wind speed of more than 5 m/s, which is necessary for the operation of wind turbines.

The development of renewable energy in general gives Kazakhstan the opportunity to build a strong economy and meet its demand for energy consumption [1]. According to annual meteorological data, the average annual air flow velocity is 3-3.5 m/s, which varies from the terrain of the territory [2].

In this regard, the development and research of wind turbines that work efficiently and generate electricity at low wind speeds is relevant.

At low wind speeds from 2 m/s to 5 m/s, sailing wind turbines have an advantage in the form of starting the operation of the wind wheel and generating electric energy over traditional blade wind turbines.

Also, sailing wind turbines have increased efficiency compared to classical wind turbines [3] due to the so-called adjustment to the direction and strength of the wind. If conventional wind turbines have an efficiency of 30 %, then a sailing-type wind turbine gives all 80 %. Its efficiency exceeds the blade-type wind turbines by 2.3 times.

An important advantage is that the operating costs of sailing wind turbines are twice as low as those of conventional installations.

The original design of the wind wheel makes it possible to do without other weather- or wind-oriented devices [4-6].

Sailing aerodynamic surfaces are installed to the wind in such a way that they provide maximum resistance to the air flow, that is, they have high frontal or aerodynamic resistance. This position allows them to create maximum pressure on the surface and obtain, respectively, the maximum driving (aerodynamic) force [7].

To increase the strength of the sail blade, the authors of the patent for the invention [8] included wind turbines of wind intakes and wind deflectors in the design, which are made of sail fabric with the possibility of lifting and lowering it, in which part of the blade of the rotor blades from the inner rib is made whole, and the rest up to the outer rib is in the form of vertical blinds. However, the disadvantage of such a design is the bulkiness and complexity.

The novelty of the work is the addition of an adjustment mechanism to control the pitch of the blade rotation by changing the angle of attack when the wind increases.

The aim of the authors' work is to study the aerodynamic characteristics of a two-bladed sailing wind turbine. This goal is achieved by the following tasks:

- creating a layout of a two-bladed sailing wind turbine;
- conducting experiments in the T-1-M wind tunnel;
- determination of the drag force of the sail blades from the angle of attack at different wind speeds;
- determination of the lifting force of the sail blades from the angle of attack at different wind speeds;
- finding the rotation frequency of the wind power plant from the angle of attack at different wind speeds.

Experimental methodology

To create a real wind turbine design with sailing blades, a two-bladed sailing wind turbine was developed and created, where the blades are made of elastic, lightweight and durable material [9]. The material of the raincoat, having a high density, also has a large roughness of the streamlined surfaces. The elasticity and lightness of the raincoat material ensures the flexibility of the surface, which is well amenable to fluctuations in the air flow, which reduces its resistance. An estimated comparison of the resistance of a solid triangular plate of a similar area showed significantly greater resistance than that of a movable, self-regulating air flow form, triangular sail.

The wind wheel is fixed through bearings to the mast. The mast is made of 40 mm plastic pipes. The metal axis of rotation of the wind wheel and the metal frame of the blades are fixed to the bearings. The triangular shaped blade frame consists of two metal rods 22 cm and 13 cm long.

A sail cloth is fixed to the frames of the blades. The material of the sail consists of a raincoat fabric [10]. Raincoat is a fabric made of natural or synthetic material, which is impregnated with a special moisture–repellent substance. This substance protects the material from getting wet and helps to remove moisture. The material of this nature is convenient and necessary for use in rainy and snowy seasons.

Experimental studies were conducted at the Scientific Center “Alternative Energy” in the laboratory “Aerodynamic Measurements” of the Faculty of Physics and Technology of the Academician E.A. Buketov Karaganda University.

All experimental studies were carried out in the T-1-M wind tunnel. Drag forces and lift were measured on aerodynamic scales. The location of the sailing lines in the working part of the T-1-M wind tunnel is shown in Figure 1.

The flow rate was controlled using the wind tunnel control panel and varied from 3 m/s to 12 m/s.

When the wind increases, the adjustment mechanism controls the pitch of the blade rotation, changing the angle of attack. The rotation speed of the wind wheel will slow down and the wind turbine will have a stable output power and safe operation and maintenance. The wind wheel will never go beyond the permissible limits of rotation speed, even when faced with variable wind speed and strong storms.

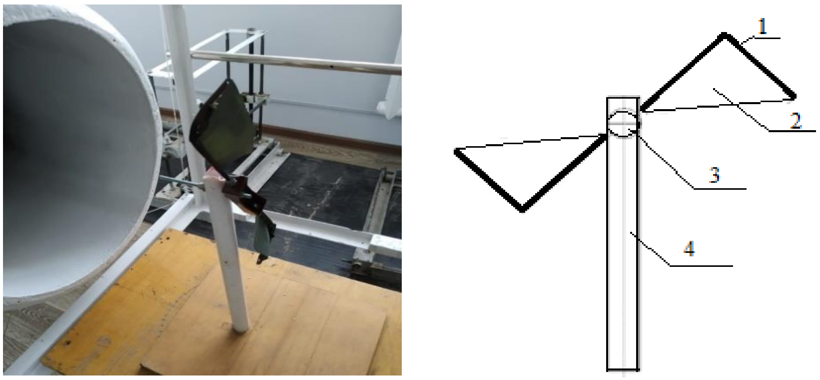

a) b)

1 — blade frame, 2 — blade material, 3 — wind wheel rotation axis, 4 — mast.

Figure 1. Location of the sail blade in the working part of the T-1-M wind tunnel (a), schematic diagram (b)

The wind wheel (Fig.1), driven by the thrust of the sail blades, experiences the action of several forces, of which the actual thrust force and the lifting force arising on the sails are useful. Another component is the drag force of the sail.

The novelty of the prototype is that the fabric is attached to an L-shaped base.

Based on laboratory studies, the sailing aerodynamic surfaces of the prototype showed maximum resistance to air flow, i.e. high frontal or aerodynamic drag.

When studying the effect of wind on a sail, a whole set of forces arises on it, including aerodynamic force. A rarefaction region appeared on the outside of the sail, where aerodynamic forces arise, the resultant of which R (Fig. 2) is almost perpendicular to the chord of the sail — the segment connecting the edges of the sail. The value of the force, as well as the point of application of the resultant, strongly depend on the angle at which the sail (its chord) is to the wind — this angle is called the angle of attack, as well as the bending of the sail (the potbellied was 5 cm), wind strength and how much the incoming wind flow is laminar, that is, without vortices and turbulence.

If we decompose the aerodynamic force into two components — parallel X and perpendicular to the wind Y, then we can estimate how much the sail will tend along with the wind and move perpendicular to the wind. In this case, the Y component is called the lifting force (because it is this force that causes the blade to rise when the blade is horizontal), and the X component is the drag force of the sail.

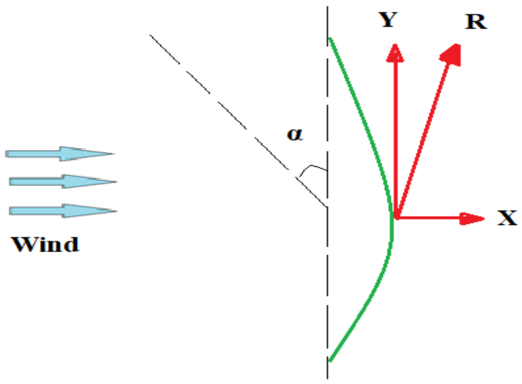

Figure 2. Distribution of forces on the surface of the sail blade

If we consider the movement of the wind engine in sharp directions to the wind, then the efficiency of the sail as a driving force depends on the same parameters as the efficiency of the blades when creating lift:

– surface area of the sail;

– the profile of its cross-section;

– the angle of the installation of the sail in relation to the incoming air flow (pennant wind) and wind speed;

– aerodynamic elongation and shape of the sail contour.

The blades of a wind turbine with a dynamically changing surface have a shape that allows you to get the maximum effect from the wind force at minimal cost. The choice of blade material also affects the aerodynamic parameters or the performance of the wind turbine.

Research results

The resulting aerodynamic force of the sail is formed by two main components: lifting force (F_y) and drag force (F_x). The lifting force (F_y) acts at right angles to the wind, and the drag force (F_x) acts downwind. As the wind speed increases, the drag force grows faster than the lifting force. Therefore, for different wind speeds, different forms of sails differ, which have optimal lift-to-drag ratios.

Figure 3 shows a graph of the dependence of the drag forces of the sail blades on the angle of attack at different wind speeds.

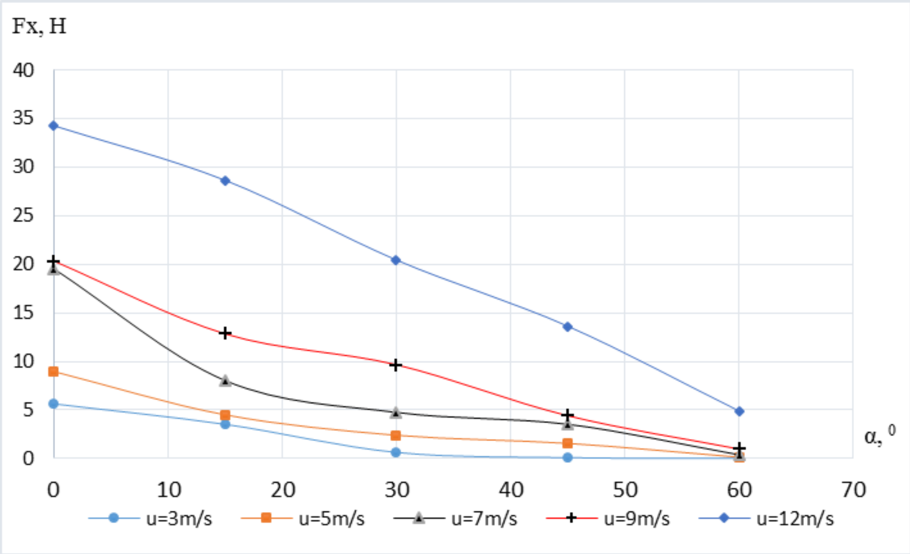

Figure 3. Graph of the dependence of the drag forces of the sail blades on the angle of attack at different wind speeds

The dependence of lift and drag on the angle of attack is crucial in determining the effectiveness of the sail blade.

As can be seen from the graph, a change in the drag force at the angle of attack α is obtained=0^0, 15^0, 30^0, 45^0, 60^0 in different wind speeds. When analyzing the quantitative values of the drag force, it was found that at 0 degrees with an increase in wind speed, the drag force value becomes higher. The maximum value of F_x = 34 N is at $\alpha = 0^0$ and 12 m/s.

Figure 4 shows a graph of the dependencies of the lifting force of the sail blades on the angle of attack at different wind speeds.

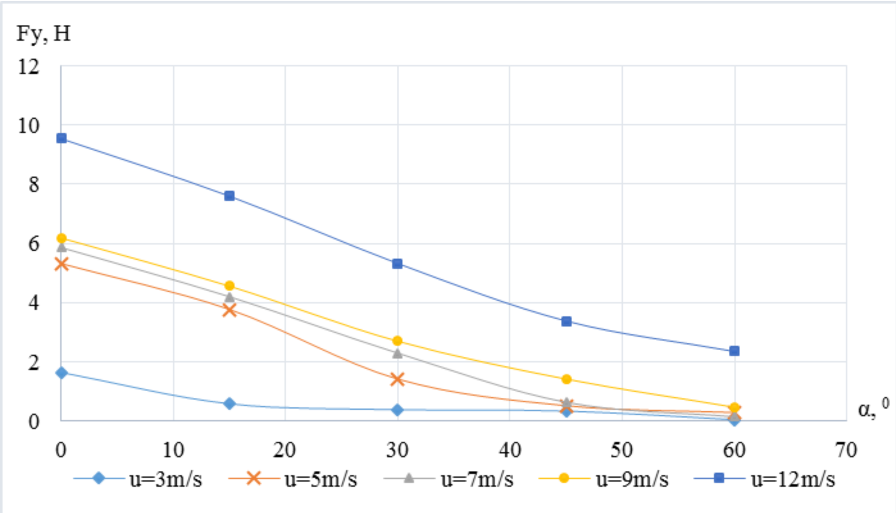

Figure 4. Graph of the dependence of the lifting force of the sail blades on the angle of attack at different wind speeds

Figure 5 shows a graph of the dependencies of the rotational speed of a prototype wind power plant on wind speed. It is shown how the value of the lifting force changes with an increase in wind speed and a change in the angle of attack. It is established that at the angle of attack α = 0 °, the maximum values of the lifting force are obtained. The measurement error is 1-2 %.

The lifting force is the result of an uneven distribution of air pressure on one side compared to the other side of the sail blade. Based on this, according to the Bernoulli principle, the sail has a lower air pressure on the front (leeward) side and more pressure on the rear (windward) side. With a minimum angle of attack, since the flow smoothly flows around the sail blades, there is a smooth transition from low pressure on the leeward part to higher pressures on the windward part.

It is necessary to pay attention that the sail blades with a high angle of attack have a very low pressure near the front, which is then followed by a sharp increase in pressure. In this case, the boundary layer cannot withstand such a rapid increase in pressure, as a result of which the flow is separated, and the flow is disrupted, which entails a decrease in the value of the lifting force.

From the obtained dependences (Fig. 3-4), the proportional dependence of the lifting force and the drag force of the blades on the angle of attack is visible.

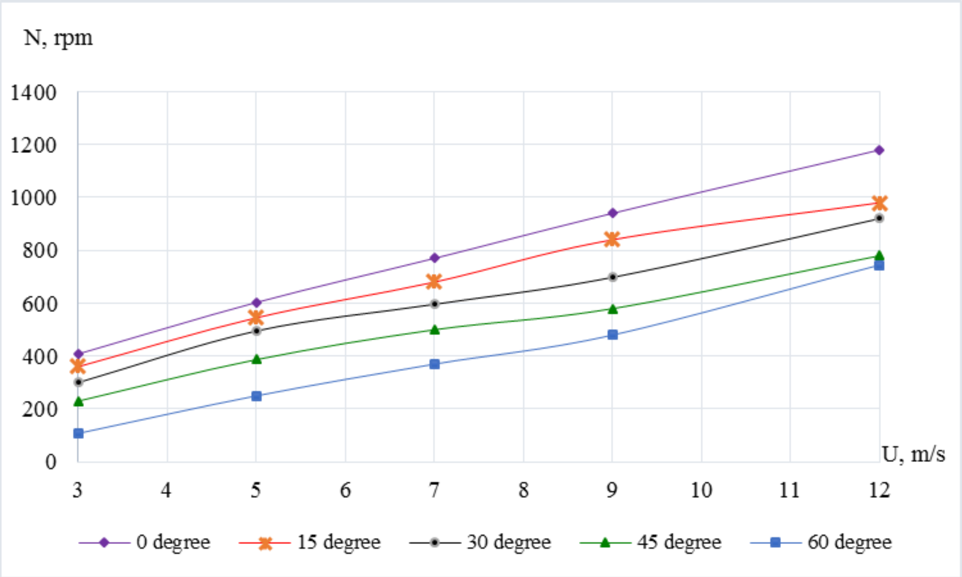

Figure 5. Dependence of the rotation frequency of the wind power plant on the angle of attack at different wind speeds

Figure 5 shows that an increase in wind speed leads to an almost linear increase in the number of revolutions of the wind wheel per minute. This is due to the fact that with an increase in the wind speed running into the wind wheel, the pressure force acting on the sail blades increases linearly. It is established that at an angle of attack of 0, the maximum aerodynamic quality of the wind wheel is realized. At a given angle of attack, maximum aerodynamic forces arise, which causes the wind wheel to rotate.

Conclusion

In the course of the study, the following optimal results were obtained:

- a graph of the dependences of the drag forces of the sailing blades on the angle of attack at different wind speeds, based on it is established that the maximum value of F_x = 34 N has at $\alpha = 0^0$ and 12 m/s. This fact is explained by the fact that with an increase in the deviation of the flow direction from the perpendicular to the plane of the blades, a restructuring of the turbulent air flow around the wind turbine occurs. In a turbulent flow, as a result of interaction with secondary flows created by the sail blades, pressure discharge zones appear, the volume of this discharge zone varies depending on the angle of attack of the air flow. As a result of the interaction of the pressure field created by the main flow and the discharge zone created by the secondary flow, we have a complex dependence, where the drag force with increasing flow velocity and angle of attack begins to decrease sharply. This is due to the turbulence of the flow, as a result of which turbulent vortices create additional aerodynamic drag;

- a graph of the dependencies of the lifting force of the sailing blades on the angle of attack at different wind speeds, based on which it is determined that at the angle of attack $\alpha = 0$ °, the maximum values of the lifting force are obtained, because at the minimum angle of attack, the flow smoothly flows around the sailing blades, there is a smooth transition from low pressure on the leeward part to higher pressures on the windward part;

- the dependence of the rotation frequency of the prototype wind power plant on the wind speed, at which it is established that, at an angle of attack of 0°, the maximum aerodynamic quality of the wind wheel is realized.

This research has been/was/is funded by the Science Committee of the Ministry of Education and Science of the Republic of Kazakhstan (Grant No. IRN AP14870066 project "Development and creation of an energy-efficient combined vertical-axis wind power plant using a gearless low-speed electric generator").

References

1 Потенциал ветровой энергии в Казахстане [Электронный ресурс]. — Режим доступа: https://www.eurasian-research.org/publication/potential-of-wind-energy-in-kazakhstan/? lang=ru/

2 Погода в стране Казахстан. — [Электронный ресурс]. — Режим доступа: http://weatherarchive.ru/Pogoda/Kazakhstan

3 Соколов С.Е. Электрические станции и подстанции. Ветровая и солнечная энергетика: учеб. пос. / С.Е. Соколов, И.С. Соколова. — Алматы: АУЭС, 2018. — 105 с.

4 Грибач Ю.С. Ветер — альтернативный источник энергии / Ю.С. Грибач, О.О. Егорычев, Е.В. Кургузова // Силовое и энергетическое оборудование. Автономные системы. — Т. 2. Вып. 1. — 2019. — С. 40–49.

5 Грозных В.А. Проблемы надежности электроснабжения от ветроэнергетических установок / В.А. Грозных // Главный энергетик. — 2017. — № 8. — С. 67–75.

6 Лукашин П.С. Методика решения задач аэроупругости для лопасти ветроустановки с использованием СПО / П.С. Лукашин, В.Г. Мельникова, С.В. Стрижак, Г.А. Щеглов // Тр. ИСП РАН. — 2017. — Т. 29. Вып. 6. — С. 253–270. DOI: 10.15514/ ISPRAS2017-29(6)-16.

7 Власов В.К. Ветродвигатели. Теория и практика / В.К. Власов. — М.: Техносфера, 2020. — 226 с.

8 Аманов Б.И. Патент РФ № 2664037 С2. Ветроэнергетическая установка вертикального типа / Б.И. Аманов. Опубл. 2018.

9 Tleubergenova A.Zh. Study of aerodynamic parameters of the sail blade / A.Zh. Tleubergenova, N.K. Tanasheva, K.M. Shaimerdenova, L.L. Minkov, A.N. Dyusembaeva, S.Zh. Uzbergenova // Bulletin of the University of Karaganda-Physics, 2022. — Vol. 1(105). — P. 58-65.

10 Tanasheva N.K. Investigation of the aerodynamic forces of a triangular wind turbine blade for the low wind speeds / N.K. Tanasheva, A.Zh. Tleubergenova, K.M. Shaimerdenova, L.L. Minkov, S.Zh. Uzbergenova // Eurasian physical technical journal, 2021. — Vol. 4(38). — P. 59–64.

А.Ж. Тлеубергенова, Н.К. Танашева, К.М. Шаймерденова, Н.К. Ботпаев,
Л.Л. Миньков, С.Б. Қасиев

Екіқалақшалы желкенді жел қондырғысының аэродинамикалық сипаттамаларын зерттеу

Мақалада екіқалақшалы желкенді жел қондырғысының тәжірибелік үлгісі зерттелген. Эксперименттік жұмыс жасау үшін желкенді екіқалақшадан тұратын жел қондырғысының макеті жасалды. Желкенді қалақшалардың материалы икемділігі мен жеңілдігі, арзандығы, тегістелген беттердің кедір-бұдырлығы бойынша таңдап алынды. Зерттеу барысында қалақшаға әсер ететін аэродинамикалық параметрлер көрсетілген. Ауа ағынының жылдамдығы 3-тен 12 м/с-қа дейін өзгерді. Шабуыл бұрышы $\alpha=0^0$, 15^0, 30^0, 45^0, 60^0 болатындай жел қондырғысының қалақшаларын бұра отырып, ауа ағынының жылдамдығына көтеру күші мен маңдайлық кедергі күшінің тәуелділігі алынды. Қалақшалар орналасу деңгейін өзгерткенде көтеру күші мен маңдайлық кедергі күшінің төмендейтіні анықталды. Шабуыл бұрышы өскен сайын $\alpha>0^0$ ауа ағынына қатысты жел доңғалағының мидель қимасының төмендеуіне алып келеді. Соның негізінде аэродинамикалық күштердің төмендеуі байқалады. Ауа ағынының жылдамдығы артқан сайын жел доңғалағының айналу жиілігі де артады. Алайда қалақшалардың әртүрлі бұрыш жасай орналасуы айналу жилігінің сандық мәніне әсер ететіндігі тәжірибе кезінде анықталды. Жасалған эксперименттер бойынша бірнеше мәндер алынды. Алынған мәндерге талдау жасалды. Шабуыл бұрышының өзгеруімен жел жылдамдығына жел доңғалағының айналу жиілігі тәуелділігі бойынша график тұрғызылды.

Кілт сөздер: көтеру күші, жел энергетикалық қондырғы, маңдайлық кедергі күші, шабуыл бұрышы, жел жылдамдығы, айналу жиілігі.

А.Ж. Тлеубергенова, Н.К. Танашева, К.М. Шаймерденова, Н.К. Ботпаев, Л.Л. Миньков, С.Б. Касиев

Исследование аэродинамических характеристик двухлопастной парусной ветроустановки

В статье исследован опытный образец ветроустановки с двумя лопастями. Для экспериментальной работы был разработан макет парусной ветроустановки, состоящей из двух лопастей. Материал парусных лопастей подбирался по эластичности и легкости, дешевизне, шероховатости обтекаемых поверхностей. В ходе исследования показаны аэродинамические параметры, действующие на лопасть. Скорость воздушного потока варьировалась от 3 до 12 м/с. Зависимость подъемной силы и лобовой преграды от скорости воздушного потока получали путем поворота лопастей ветродвигателя так, чтобы угол атаки составлял $\alpha = 0^0$; 15^0; 30^0; 45^0 и 60^0. Установлено, что при изменении положения лопастей уменьшаются подъемная сила и сила лобового сопротивления. При увеличении угла атаки $\alpha > 0^0$ наблюдается уменьшение мидельного сечения ветроколеса по отношению к воздушному потоку. На этой основе происходит снижение аэродинамических сил. По мере увеличения скорость воздушного потока и частота вращения ветроколеса возрастают. Однако во время эксперимента установлено, что расположение лопастей под разными углами влияет на численное значение частоты вращения. По указанным выше экспериментам было получено несколько значений. Проведен анализ полученных значений. Построен график по зависимости частоты вращения ветрового колеса от скорости ветра с изменением угла атаки. Ветроустановка с лопастями с изменяемым углом атаки, которые, поворачиваясь, постепенно становится всё более параллельнным к направлению ветра. Центробежные силы регулируют наклон лопастей и, как следствие, скорость вращения ветроколеса, и держат ветрогенератор при номинальной частоте вращения.

Ключевые слова: подъемная сила, ветроэнергетическая установка, сила лобового сопротивления, угол атаки, скорость ветра, частота вращения.

References

1 Potentsial vetrovoi energii v Kazakhstane [Wind energy potential in Kazakhstan]. (n.d.). base.garant.ru. Retrieved from https://www.eurasian-research.org/publication/potential-of-wind-energy-in-kazakhstan/? lang=ru/ [in Russian].

2 Pogoda v strane Kazakhstan [Weather in the country of Kazakhstan]. (n.d.). base.garant.ru. Retrieved from: http://weatherarchive.ru/Pogoda/Kazakhstan [in Russian].

3 Sokolov, S.E. & Sokolova, I.S. (2018). Elektricheskie stantsii i podstantsii. Vetrovaia i solnechnaia energetika [Electric stations and substations. Wind and solar energy]. Almaty: AUJeS [in Russian].

4 Gribach, Yu.S., Egorychev, O.O. & Kurguzova, E.V. (2019). Veter — alternativnyi istochnik energii. Silovoe i energeticheskoe oborudovanie. Avtonomnye sistemy [Wind is an alternative source of energy. Power and power equipment. Autonomous systems]. Moscow, 2, 1, 40–49 [in Russian].

5 Groznyh, V.A. (2017). Problemy nadezhnosti elektrosnabzheniia ot vetroenergeticheskikh ustanovok [Problems of reliability of power supply from wind power installations]. Glavnyi energetic [Chief Power Engineer]. 8, 67–75 [in Russian].

6 Lukashin, P.S., Melnikova, V.G., Strijhak, S.V., & Shcheglov, G.A. (2017). Metodika resheniia zadach aerouprugosti dlia lopasti vetroustanovki s ispolzovaniem SPO [The method of solving aeroelasticity problems for wind blade using open source software]. *Trudy ISP RAN — Proceedings ISP RAS,* 29, 6, 253–270. DOI: 10.15514/ISPRAS2017-29(6)-16 [in Russian].

7 Vlasov, V.K. (2020). Vetrodvigateli. Teoriia i praktika [Wind turbines. Theory and practice]. Moscow: Tekhnosfera [in Russian].

8 Amanov, B.I. (2018). Patent Rossiiskoi Federatsii № 2664037 C2. Vetroenergeticheskaia ustanovka vertikalnogo tipa [Patent of Russian Federation No. 2664037 C2. Vertical wind turbine] [in Russian].

9 Tleubergenova, A.Zh., Tanasheva, N.K., Shaimerdenova, K.M., Minkov, L.L., Dyusembaeva, A.N., & Uzbergenova, S.Zh. (2022). Study of aerodynamic parameters of the sail blade. *Bulletin of the University of Karaganda-Physics, 1(105),* 58-65.

10 Tanasheva, N.K., Tleubergenova, A.Zh., Shaimerdenova, K.M., Minkov, L.L., & Uzbergenova, S.Zh. (2021). Investigation of the aerodynamic forces of a triangular wind turbine blade for the low wind speeds. *Eurasian Physical Technical Journal, 4(38),* 59–64.

DOI 10.31489/2023PH1/49-58

UDC 533.15:536.25

V.N. Kossov[1], S.A. Krasikov[1], S.M. Belov[2], O.V. Fedorenko[2], M. Zhaneli[1]

[1]Abai Kazakh National Pedagogical University, Almaty, Kazakhstan;
[2] al-Farabi Kazakh National University, Almaty, Kazakhstan
(E-mail: kosov_vlad_nik@list.ru*)*

Comparative study of evolution of structured flows at boundary of the regime change "diffusion — concentration convection" in isothermal multicomponent mixing in gases by techniques of visual and numerical analysis

During isothermal multicomponent diffusion process, the number of effects appear that are not observed visually when mixed in binary mixtures. These include occurrence of convective instability with subsequent formation of structured flows. The feature of this type of mixing is that convection is realized under conditions of decrease in density of mixture with height. Flow visualization method allows to fix information about distribution of medium parameters by dynamics of structures in convective flows. Application of computer processing methods, as well as techniques of identifying images of thermophysical fields, allows to obtain quantitative information about convective flows. For an isothermal ternary gas mixture heliumargon-nitrogen, shadow images of structural formations formed in convective flows due to the instability of mechanical equilibrium are represented in this work. To carry out digital analysis of experimental shadow images, a simplified virtual model of the lower chamber of the diffusion cell was created. Based on digital analysis of visual images, quantitative characteristics related to estimation of the size of convective formations, period of their formation, and linear velocity of convection cells when moving through diffusion channel are presented. It has been established that the growing convective disturbances arising in the system cause a change in the characteristic scale of convective cells. The analysis of shadow images also showed that a vortex is formed in convective flows, which consists mainly of a component with the highest molecular weight. Comparison of visual images of experimental fields with simulation flows is implemented, on the basis of which composition of mixture components in convective structures is estimated. It is shown that the obtained value of the concentration of the heavy component in the vortex filament can be taken as the minimum.

Keywords: gas mixtures, diffusion, instability, convection, visualization, shadow image, digital technologies, numerical modeling.

Introduction

Convective instability in gases and liquids is occurred in many technological schemes, therefore its description appeared wide interest in experimental-practical and computational-theoretical plans. Natural gravitational convection caused by instability of mechanical equilibrium of the system is complex type of motion of continuous medium with different spatial and temporal scales [1, 2]. Most modern studies of systems in which Rayleigh-Benard convection and its analogues occur themselves are based on a system of equations of continuum dynamics, mass transfer and heat simplified within the Boussinesq approximation. This approach proved to be very productive, as it allows to identify spectrum of parameters that determine transition from stable state to an unstable one [3, 4]. Due to number of simplifications, approach presented in [1-4] does not fully consider dynamics of continuous medium in channel of given shape, as well as nonlinear spatial effects. Obviously, that with invention of powerful modern computers appears possibility to conduct computational experiments based on the numerical solution of equations used in mathematical model of physical phenomenon or process under study. However, question of correctness of comparative analysis of numerical results with reference experimental indicators raises. Moreover, such indicators can be not only direct and indirect experimental data, but also images of convective flow fields, which are the main source of information about distribution of medium parameters, configurations and dynamics of structures in the flow, current lines, turbulent vortices, etc. Panoramic visualization of convective flow field of medium is not only an important way to obtain information about structured flows in experimental studies of gas, liquid and plasma, but also provides benchmarking for testing software packages and algorithms in computational thermophysics [5].

Among wide variety of experimental visualization of convective flows in gaseous media, optical methods for studying transparent media based on the phenomenon of light deflection when it passes through inhomogeneities of density of transparent medium have become widespread [6]. As it is known, optical refractive index of medium *n* is equal to ratio of speed of light in medium to the speed of light in vacuum and is related to the local density of medium *ρ* by the Lorentz-Lorentz formula, which for gases has the form [5, 6]:

$$\frac{n-1}{\rho}=k, \tag{1}$$

where *k* is a constant value that has its characteristic value for particular gas.

If gas flow is inhomogeneous, in this case optical refractive index of medium in the studied flow area depends on coordinates (*x*, *y*, *z*). During flow area with variable density is illuminated, beam propagating parallel to the *z* axis and passing through inhomogeneity deviates from original direction of propagation by an angle *a*

$$\alpha=\int_0^L \frac{\partial}{\partial x}\ln n(x,y,z)\,dz\,. \tag{2}$$

Density changes are summed up in direction of the light beam in medium under study and thus integral value of density change is recorded. In shadow visualization of the gas flow field, change in illumination is proportional to the degree of change in density gradient of gas. In presence of strong density gradients in flow, additional deflections of beam occur on surface of convective formation, which is dark area from the side of incoming flow in the form of light field of varying intensity.

Until recently, images obtained in framework of approximation (1), (2) were mainly of qualitative nature. However, with advent of digital age, computer processing methods, image recognition analysis tools for thermophysical fields, numerical methods modeling the motion of continuous medium allow to obtain quantitative information about flows [7-9]. Therefore, investigate of dynamics of structured flows resulting from convective instability of isothermal triple gas mixtures by comparing visual and numerical methods seems relevant, since it allows to obtain new quantitative information about partial flows of components.

The objectives of the proposed study are:

1. Obtaining visual shadow images of convective formations caused by the instability of mechanical equilibrium in an isothermal ternary mixture of helium – argon – nitrogen at high pressures.

2. Estimation of the characteristic dimensions of convective structures, which mainly consisted of a component with the highest molecular weight, and the speed of their movement in a medium with a lower density.

3. Using the FlowSimulation software included in the SolidWorks package [9], to consider the possibility of numerical simulation of individual stages of the movement of a transient structured convective flow, within which it is possible to calculate the threshold values of the concentration of the heavy component in the convective structure in the lower flask of the diffusion cell (DC).

4. Comparison of the results of numerical simulation with quantitative characteristics obtained from the analysis of shadow visual images.

Optical experimental visualization of convective flows during isothermal mixing of triple gas mixtures

Experimental studies of multicomponent mixing in gas mixtures with significant difference in diffusion coefficients have shown that, under certain conditions, convective instability may occur in them, followed by appearance of structured flows [10, 11]. Further experimental [12-14] and computational-theoretical [15-17] studies have shown variety of thermophysical concentration flows at the boundary of “diffusion–convection” regime change. Feature of registered flows is that occur in gas systems under condition of decrease in the density of mixture with height, which is not typical for diffusion. In this regard, visual registration of dynamic features of convective flows occur particular importance, as it allows obtaining new experimental information.

Traditionally, multicomponent mixing in gas mixtures at elevated pressures is studied on devices implementing the two-column method [10, 12]. Methodology of experiment is detailed in the works [10, 12, 13], so necessary to pay attention only to the main stages of experimental study. The upper and lower flasks of diffusion cell (Fig. 1a) were filled with studied gas mixtures up to pressure of the experiment. Next channel connecting flasks was opened and at the same time, start time of the mixing process was fixed. At the completion of the experiment, channel closed, after registered time of mixing completion, and then conducted mixtures analysis from every flask by chromatography method. Experimental concentrations compared with numerical by Stefan-Maxwell equations values [18] by assuming diffusion process.

Diffusion cell (DC) was modified and experimental procedure was adjusted to obtaining visual information about dynamic processes in gas flows. In the modified diffusion cell in the lower and upper cameras windows made of quartz glass with diameter of 60 mm and a thickness of 20 mm were viewing (Fig. 1b). Windows allowed viewing almost inside part of the upper or lower cameras. Flasks were connected by diffusion channel with optical windows, which allowed visualization of convective structures inside channel (Fig. 1c). Parts of connecting channel exits by center of upper and lows of the flasks of diffusion cells (DC). This construction allowed possibility to observe mixing process not only medium of channel, and also at the end of the channel. Geometric parameters of DC are follows: volumes of the lower and upper flasks are 226.8 and 214.5 sm^3; cross–sectional area of the channel is 6.1×6.1 mm^2, and its length is 165.4 mm.

a) b) c)

Figure 1. Diffusion cell of the two-column method: a) Plan DC. 1, 3 — lower and upper flasks; 2 — a block with diffusion channel; 4, 5 — fitting [14]; b) DC with viewing windows;
c) Diffusion channel

To visualize convective flows, principle of the Schlieren system [6] was used, which consists in the fact that part of the light deflected when passing through inhomogeneity of gas density is delayed by the edge of knife installed in the focal plane of beam that passed through the area under study. As a result, change in illumination of the corresponding image areas is recorded. Changing illumination at point with density inhomogeneity is determined by magnitude of the beam deflection angle, focal length of the second lens and size of light source. When visualizing gas flow field by the Schlieren method, change in illumination is proportional to the gradient of gas density in area under study in the direction perpendicular to the knife edge. As a result, vortex structures and rarefaction areas are better visualized [5]. Optical scheme for obtaining shadow images is shown in Fig. 2 [14] and does not require additional explanations. Image was fixed to video camera by rotating the image 90° through prism not indicated in optical scheme (Fig. 2) and located after lens 11.

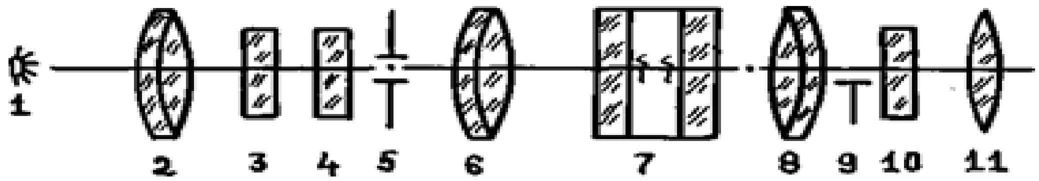

Figure 2. Optical scheme: 1 – light source; 2 – condenser lens; 3 – lightfilter; 4 – main protective glass lens; 5 – slit; 6 – main lens; 7 – camera of diffusion cell; 8 – receiving lens; 9 – knife; 10 — safety glass receiving lens; 11 – lens [14]

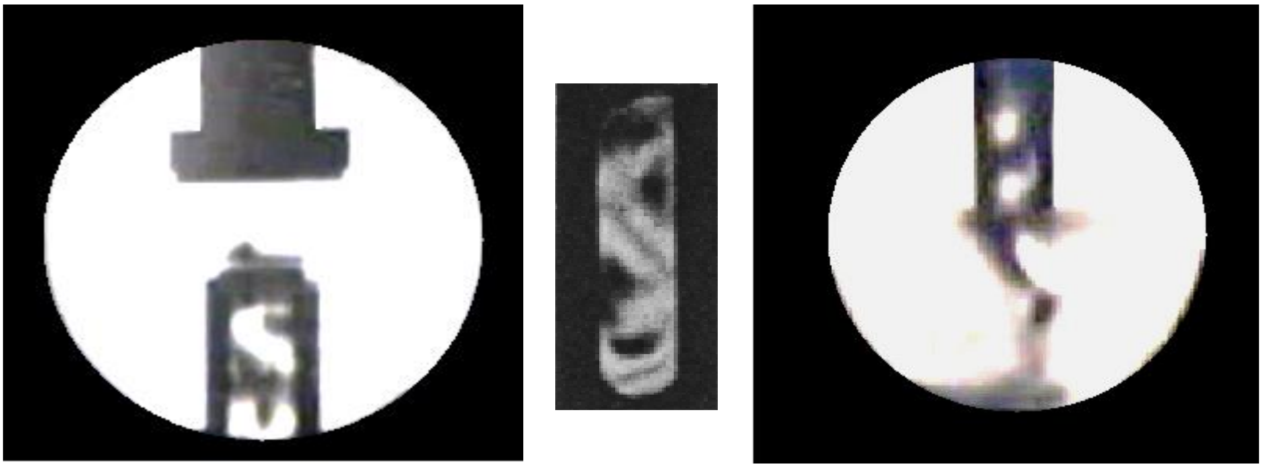

a) b) c)

Figure 3. Motion of vortex cord in the diffusion cell. System 0.5143 He + 0.4857 Ar — N_2, p = 2.54 MPa, T = 298.0 K: a) — section of diffusion channel in the upper camera; b) — middle of the diffusion channel; c) — section of diffusion channel in the lower camera

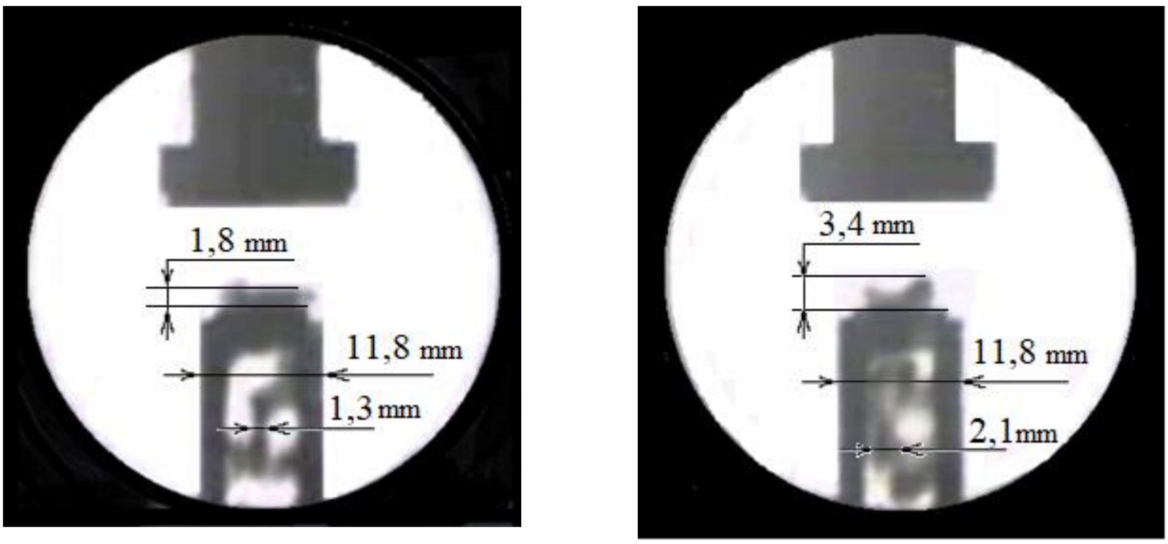

a) b)

Figure 4. Shadow images of gas mixture separation zone in the upper chamber of diffusion cell for system 0.5143 He + 0.4857 Ar — N_2 at p = 2.54 MPa, T = 298.0 K: a) Initial stage of the process; b) Mode of periodic formation of vortex structures

Shadow visualization of various mixing modes was implemented when studying the evolution of convective flows in an isothermal triple gas mixture of helium-argon-nitrogen, which arose at boundary of the regime change “diffusion — concentration gravitational convection”. Thermophysical parameters of transition and geometric characteristics of channel providing the kinetic transition from one state to another were calculated within the framework of theoretical analysis for convective stability of multicomponent gas mixture [15].

Figure 3 shows shadow images of vortex convective cords in different coordinates of the diffusion channel. Analysis of presented shadow patterns indicates that convective vortex is clearly recorded, mainly consisting of component with the highest molecular weight. A frame-by-frame analysis of visual images from the beginning of the diffusion process and the subsequent formation of convective flows makes it possible to estimate the time required to reach the front of the vortex filament from the cutoff of the diffusion channel (Fig. 3a) to the border of the lower flask window (Fig. 3c) in 1 s. This, according to rough estimates, is equivalent to a speed of 0.025 $m \cdot s^{-1}$.

Figure 4 shows shadow images of gas mixture separation zone at the initial stage of steady-state process (Fig. 4a) and after ~ 0.5 s. (Fig. 4b). At the initial stage, descending convective structured vortex flows are clearly recorded. The change in the characteristic scale of convective cells from 1.3 mm (Fig. 4a) to 2.1 mm (Fig. 4b) is associated with growing convective disturbances in the system. A visual study of the evolution of convective flows at the initial stage of mixing showed that the characteristic size of the vortex filament in the diffusion channel is in the range of 1.3–3.5 mm.

Verification of experimental shadow images of convective flows with computational simulations of shadow images

The introduction of digital technologies in the methods of analysis of thermophysical flows and the expansion of the possibilities of numerical modeling makes it possible to mutually supplement the data of experimental visualization of flows, to validate models and algorithms for numerical calculations [19]. Verification of the calculated and experimental images of the fields of concentrations, density, temperature, and other thermophysical characteristics of the combined complex gas-dynamic flow shows satisfactory agreement in detailing the results of the experiment and subsequent interpretation of the characteristic features of the observed effects [19-20].

Based on the approaches outlined in [19-20], there is an assumption that some features associated with the evolution of convective flows caused by the instability of the mechanical equilibrium of the mixture can be detailed using algorithms for the numerical solution of continuum equations included in the packages of applied calculation programs. In this work, such a calculation was carried out using the FlowSimulation program included in the SolidWorks package created for a simplified virtual model of the lower chamber of a diffusion cell [9, 21].

Within the framework of the FlowSimulation calculation program, heat and mass transfer in vertical rectangular channels is modeled using the Navier–Stokes equations, as well as relations describing the conservation of mass, momentum and energy in a given medium [9]. When modeling convective flows, effect of turbulence averaged over small time scale on the flow parameters is used, and large-scale time changes in components of gas dynamic flow parameters averaged over small time scale are considered by introducing the corresponding time derivatives [9]. As a result, equations have additional terms — Reynolds stresses, and to close this system of equations, the equations of transfer of kinetic energy of turbulence and its dissipation are used in the framework of the k-ε model of turbulence [22].

Comparison of the calculated simulation of convective formation with the experimentally observed shadow image is shown in Figure 5. When modeling movement process of front of structural formation in the lower flask, the concentration of the heaviest component of the mixture (argon) in the formed vortex structures with the following component concentrations at the outlet of the lower end of the diffusion channel was estimated: c_{Ar} = 0.92 and c_{He} = 0.08 mole fractions (Fig. 5a).

At lower values of argon, the implementation of the simulation flow was not observed. It can be considered that the obtained concentration value (c_{Ar} = 0.92 mole fractions) can be taken as a threshold value. In this case, it is obvious that the real value of the concentration of the heavy component in the vortex filament can be even higher. The velocity of movement of the imitation convective structure in the lower chamber of the diffusion cell is 0.027 $m \cdot s^{-1}$, which is in satisfactory agreement with the experimental values given in the previous section. In this regard, it can be assumed that for structured flows caused by the instability of the mechanical equilibrium of the mixture, the scales of inhomogeneities, sizes and dynamics of formations can be obtained in a simulation manner and compile quantitative information about the flows. It can be considered that the comparison of numerical and experimental images of the flow visualization leads to quantitative estimates that refine the models for describing the thermo-concentration distributions for a given thermophysical field.

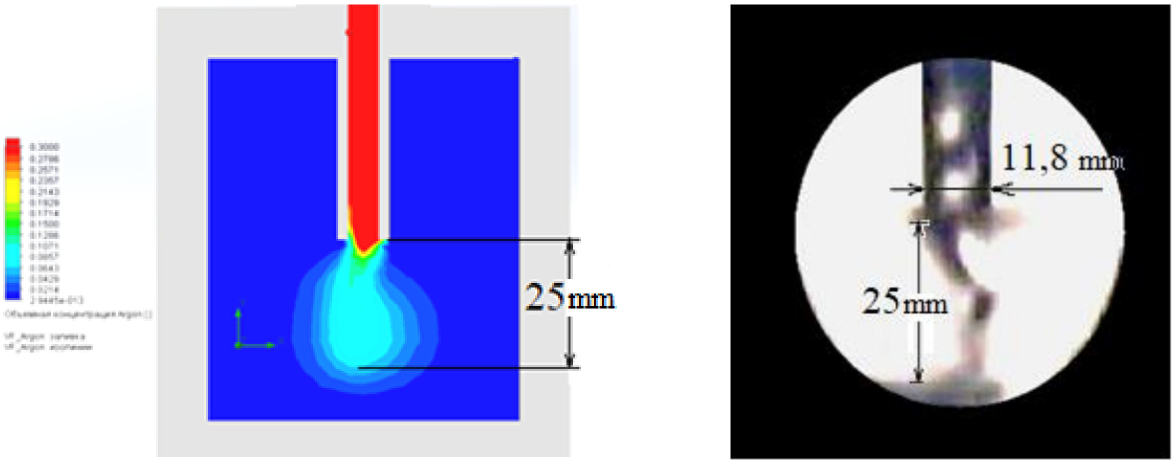

a) b)

Figure 5. Comparison of the movement of convective flow front in the initial stage of mixing caused by the mechanical equilibrium instability of the ternary system 0.5143 He + 0.4857 Ar — N_2 at p = 2.54 MPa, T = 298.0 K in the lower chamber of diffusion cell: a) Computational simulation of shadow images at c_{Ar} = 0.92, c_{He} = 0.08, t = 1.0 s; b) Shadow image of convective formation in the lower chamber of diffusion cell

Thus, analysis of images shown in Figures 3-5 allows to specify the mixing mechanism caused by instability of mechanical equilibrium in isothermal triple gas mixtures, provided that density of mixture decreases with the height of channel, which was formulated in [10, 11, 14, 15]. As it was shown in [23] under isothermal conditions due to the high mobility of helium molecules, its active penetration into nitrogen forms an increased argon content in the upper part of the channel, thereby forming an inversion layer in density, causing convective movement of the component with the highest molecular weight due to gravity. Active motion of the argon leads to convective displacement of nitrogen to upper chamber. Shadow images fix the dynamics of the separation process of argon and helium during their interaction with nitrogen in different coordinates of the diffusion channel (Figs. 3-4). Entry of convective flows, predominantly consisting of nitrogen into the upper camera, implements mixing mechanism similar an inversion layer formation. At the same time, the high diffusion mobility of helium ensures its priority penetration into the ascending nitrogen flows, thereby reducing its content in the local convective area and making shadow visualization invisible. Argon enrichment of convective formation with subsequent occurrence of hydrodynamic flow of component with the highest molecular weight leads to movement in vertical channel connecting flasks of the DC. In this case, counter (ascending and descending) convective flows are formed in the channel, i.e. a diametrically antisymmetric movement is observed (the channel is divided by a vertical plane passing through the axis into two parts, in one of which the gas rises, and in the other it falls). Counter flows differ in composition. The downstream contains more argon than the upstream, which is predominantly nitrogen. When moving due to transverse diffusion, the flows will exchange molecules of the light component (helium). The descending flow will be depleted in helium, which leads to an increase in the intensity of the convective flow. Process will continue until argon concentration exceeds certain critical value in the local areas near the cutoff in the upper part of diffusion channel. The resulting circulation of the gas mixture explains the continuity and sufficient duration of the process of convective separation in the case of diffusion instability, which was recorded in experiments [10, 11, 14].

Conclusions

Researches are conducted on the study of visual shadow images of structural formations that arose in convective flows due to the instability of the mechanical equilibrium of the isothermal triple gas mixture helium-argon-nitrogen showed:

1. Application of digital technologies for processing visual shadow images allows to obtain quantitative characteristics for estimating the size of convective formations, period of their formation, and linear velocity of convection cells when moving through diffusion channel.

2. Comparison of visual images of experimental fields with simulated flows obtained numerically provides an opportunity to evaluate quantitative characteristics associated with the composition of components in convective cells, their subsequent dynamics in a medium with different density.

3. The introduction of digital technologies in the methods of registration and analysis of visual images of convective flows makes it possible to verify numerical models of diffusion instability processes. Comparison of digital processing of the results of a physical experiment with the results of numerical simulation makes it possible to clarify the mechanism for the occurrence of convective instability during isothermal mixing in ternary gas mixtures, and to detail the types of vortex flows.

Acknowledgments

This research has been funded by the Science Committee of the Ministry of Education and Science of the Republic of Kazakhstan (grant number AP09259248).

References

1 Гершуни Г.З. Конвективная устойчивость несжимаемой жидкости / Г.З. Гершуни, Е.М. Жуховицкий. — М.: Наука, 1972. — 392 с.

2 Григорьев В.В. Численное моделирование двумерной конвекции Рэлея-Бенара / В.В. Григорьев, Р.Е. Захаров // Математические заметки СФВУ. — 2017. — Т. 24. № 1. — С. 87–98.

3 Lyubimova T.P. Onset of Soret-induced convection in a horizontal layer of ternary fluid with fixed vertical heat flux at the boundaries / T.P. Lyubimova, E.S. Sadilov, S.A. Prokopev // European. Physical Journal E. — 2017. — Vol. 40. — 15. DOI: 10.1140/epje/i2017-11505-9

4 Bejan A. Convection heat transfer / A. Bejan. — Hoboken, NJ, USA: John Wiley & Sons, 2013. — 685 p.

5 Знаменская И.А. Методы панорамной визуализации и цифрового анализа теплофизических полей: Обзор / И.А. Знаменская // Научная визуализация. — 2021. — Т. 13, № 3. — С. 125–158. DOI: 10.26583/sv.13.3.13.

6 Settls G.S. Schlieren and shadowgraph techniques. Visualizing phenomena in transparent media / G.S. Settls. — Berlin: Springer, 2006. — 376 p.

7 Brunton S.L. Machine Learning for Fluid Mechanics / S.L. Brunton, B.R. Noack, P. Koumoutsakos // Annual Review of Fluid Mechanics. — 2020. — Vol. 52. — P. 477–508. DOI: 10.1146/annurev-fluid-010719-060214.

8 Harel R. Complete deep computer-vision methodology for investigating hydrodynamic instabilities / R. Harel, M. Rusanovsky, Y. Fridman, A. Shimony, G. Oren // High Performance Computing. ISC High Performance 2020. Lecture Notes in Computer Science. — 2020. — Vol. 12321. — P. 61-80. DOI: 10.1007/978-3-030-59851-8_5.

9 Алямовский А.А. SolidWorks 2007/2008. Компьютерное моделирование в инженерной практике / А.А. Алямовский, А.А. Собачкин, Е.В. Одинцов, А.И. Харитонович, Н.Б. Пономарев. — СПб.: БХВ-Петербург, 2008. — 1040 с.

10 Жаврин Ю.И. Влияние давления на устойчивость диффузии в некоторых трехкомпонентных газовых смесях / Ю.И. Жаврин, Н.Д. Косов, С.М. Белов, С.Б. Тарасов // Журн. техн. физ. — 1984. — Т. 54, № 5. — С. 943–947.

11 Zhavrin Yu.I. Effect of the pressure on the type of mixing in a three-component gas mixture containing a component possessing the properties of a real gas / Yu.I. Zhavrin, V.N. Kosov, D.U. Kul’zhanov, K.K. Karataeva // Technical Physics Letters. — 2000. — Vol. 26, No. 13. — P. 1108-1109. DOI: 10.1134/1.1337269.

12 Dil'man V.V. Instability in unsteady-state evaporation of binary solutions into an inert gas / V.V. Dil'man, D.A. Lipatov, V.A. Lotkhov, V.A. Kaminskii // Theoretical Foundations of Chemical Engineering. — 2005. — Vol. 39, No. 6. — P. 566-572. DOI: 10.1007/s11236-005-0118-0.

13 Asembaeva M.K. Effect of the channel inclination angle on convective mixing caused by instability of mechanical equilibrium of ternary gas mixture at isothermal diffusion / M.K. Asembaeva, V.N. Kosov, S.A. Krasikov, O.V. Fedorenko // Technical Physics Letters 2019. — Vol. 45, No. 11. — P. 1071–1074. DOI: 10.1134/S1063785019110038.

14 Жаврин Ю.И. Экспериментальные методы исследования диффузии и концентрационной гравитационной конвекции, вызванной неустойчивостью механического равновесия в многокомпонентных газовых смесях / Ю.И. Жаврин, В.Н. Косов, Д.У. Кульжанов, О.В. Федоренко. — Алматы: Қазақ университеті, 2015. — 172 с.

15 Kosov V.N. Instability of mechanical equilibrium during diffusion in a three-component gas mixture in a vertical cylinder with a circular cross section / V.N. Kosov, Yu.I. Zhavrin, O.V. Fedorenko, V. Mukamedenkyzy // Technical Physics. — 2014. — Vol. 59, No. 4. — P. 482-486. DOI: 10.1134/S1063784214040161.

16 Aleksandrov O.E. Pressure dependence of the mixing rate for the free convection of a binary gas mixture in a two-flask apparatus / O.E. Aleksandrov, V.D. Seleznev // Technical Physics. — 2016. — Vol. 61, No. 7. — P. 982–986. DOI: 10.1134/S1063784216070033.

17 Dil'man V.V. Molecular turbulent evaporation in a gravitational field / V.V. Dil'man, V.A. Lotkhov // Theoretical Foundations of Chemical Engineering. — 2015. — Vol. 49, No. 1. — P. 102–106. DOI: 10.1134/S0040579515010017.

18 Bird B.R. Transport phenomenon / B.R. Bird, W.E. Stewart, E.V. Lightfoot. — N. Y.: John Wiley and Sons, Inc, 2002. — 914 p.

19 Емельянов В.Н. Визуализация данных физического и математического моделирования в газовой динамике / В.Н. Емельянов, К.Н. Волков. — М.: Физматлит, 2018. — 356 с.

20 Chetverushkin B.N. Numerical simulation of the interaction and evolution of discontinuities in a channel based on a compact form of quasi-gasdynamic equations / B.N. Chetverushkin, Y.V. Khankhasaeva, I.A. Znamenskaya, A.E. Lutsky // Mathematical models and computer simulations. — 2021. — Vol. 13, No. 1. — P. 26-36. DOI: 10.1134/S2070048221010075.

21 Алямовский А.А. SolidWorks Simulation. Инженерный анализ для профессионалов: задачи, методы, рекомендации / А.А. Алямовский. — М.: ДМК Пресс, 2015. — 562 с.

22 Черный С.Г. Численное моделирование пространственных турбулентных течений несжимаемой жидкости на основе k-ε моделей / С.Г. Черный, П.А. Шашкин, Ю.А. Грязин // Вычислительные технологии. — 1999. — Т. 4, № 2. — С. 74–94.

23 Kosov V.N. Inversion of the density gradient and the diffusion "gate" in isothermal mixing of gases / V.N. Kosov, Y.I. Zhavrin, V.D. Seleznev // Technical Physics. — 1998. — Vol. 43, No. 5. — P. 488–492. DOI: 10.1134/1.1259026.

В.Н. Косов, С.А. Красиков, С.М. Белов, О.В. Федоренко, М. Жанели

Көрінетін және сандық талдау құралдарымен газдардағы изотермиялық көпкомпонентті араластыру кезінде «диффузия — концентрациялық конвекция» режимдерінің өзгеру шекарасындағы құрылымдалған ағыстардың эволюциясын салыстырмалы зерттеу

Газдардағы изотермиялық көпкомпонентті диффузия кезінде бинарлы қоспалар араласқан кезде байқалмайтын бірқатар әсерлер орын алады. Бұған конвективті тұрақсыздықтың пайда болуы, содан кейін құрылымдық ағыстардың пайда болуы жатады. Араластырудың бұл түрінің ерекшелігі — конвекция қоспаның тығыздығының биіктігімен төмендеуі жағдайында жүзеге асырылады. Ағысты визуализациялау әдісі қоршаған орта параметрлерінің таралуы, конвективті ағындардағы құрылымдардың динамикасы туралы ақпаратты алуға мүмкіндік береді. Компьютерлік өңдеу әдістерін, сондай-ақ жылуфизикалық өрістердің кескінін анықтауға арналған құралдарды пайдалану конвективті ағындар туралы сандық ақпаратты алуға ықпал етеді. Мақалада «гелий-аргон-азот» изотермиялық үштік газ қоспасы үшін механикалық тепе-теңдіктің тұрақсыздығынан конвективтік ағындарда түзілетін құрылымдық түзілістердің көлеңкелі кескіндері берілген. Эксперименттік көлеңкелі кескіндердің сандық талдауын жүргізу үшін диффузиялық ұяшықтың төменгі камерасының жеңілдетілген виртуалды моделі жасалды. Көрнекі кескіндерді сандық талдау негізінде конвективті түзілімдердің мөлшерін, олардың пайда болу кезеңін, диффузиялық канал арқылы қозғалу кезінде конвекция ұяшықтарының сызықтық жылдамдығын бағалауға байланысты сандық сипаттамалар берілген. Конвективті құйытқулардың жүйеде өсуі конвективті ұяшықтың сипатты масштабының өзгеруіне әкелетіні анықталды. Сонымен қатар, көлеңкелі кескіндерді талдау конвективті ағыстарда ең үлкен молекулалық салмағы бар компоненттен тұратын құйын пайда болатындығын көрсетті. Эксперименттік өрістердің көрінетін кескіндерін имитациялық ағыстармен салыстыру жүргізілді, оның негізінде конвективті құрылымдардағы қоспа компоненттерінің құрамы бағаланды. Құйынды сымдағы ауыр компоненттің концентрациясының алынған мәні минималды ретінде қабылдануы мүмкін екендігі көрсетілген.

Кілт сөздер: газ қоспалары, диффузия, тұрақсыздық, конвекция, визуализация, көлеңкелі кескін, сандық технологиялар, сандық үлгілеу.

В.Н. Косов, С.А. Красиков, С.М. Белов, О.В. Федоренко, М. Жанели

Сравнительное исследование эволюции структурированных течений на границе смены режимов «диффузия–концентрационная конвекция» при изотермическом многокомпонентном смешении в газах средствами визуального и численного анализа

При изотермической многокомпонентной диффузии в газах проявляется ряд эффектов, которые не наблюдаются при смешении в бинарных смесях. К таковым можно отнести возникновение конвективной неустойчивости с последующим образованием структурированных течений.

Особенность такого типа смешения заключается в том, что конвекция реализуется при условиях уменьшения плотности смеси с высотой. Метод визуализации потоков позволяет фиксировать информацию о распределении параметров среды, динамике структур в конвективных потоках. Использование методов компьютерной обработки, а также средств идентификации изображений теплофизических полей способствует получению количественной информации о конвективных потоках. В статье для изотермической тройной газовой смеси «гелий–аргон–азот» представлены теневые изображения структурных формирований, образовавшихся в конвективных потоках, обусловленных неустойчивостью механического равновесия. Для осуществления цифрового анализа экспериментальных теневых изображений была создана упрощенная виртуальная модель нижней камеры диффузионной ячейки. На основе цифрового анализа визуальных изображений приведены количественные характеристики, связанные с оценкой размеров конвективных формирований, периода их образования, линейной скорости ячеек конвекции при движении по диффузионному каналу. Установлено, что возникающие в системе нарастающие конвективные возмущения обусловливают изменение характерного масштаба конвективных ячеек. Анализ теневых изображений также показал, что в конвективных потоках формируется вихрь, состоящий преимущественно из компонента с наибольшим молекулярным весом. Проведено сравнение визуальных изображений экспериментальных полей с имитационными течениями, на основе которого оценен состав компонентов смеси в конвективных структурах. Показано, что полученное значение концентрации тяжелого компонента в вихревом шнуре может быть принято как минимальное.

Ключевые слова: газовые смеси, диффузия, неустойчивость, конвекция, визуализация, теневое изображение, цифровые технологии, численное моделирование.

References

1 Gershuni, G.Z., & Zhukhovitsky, E.M. (1972). Konvektivnaia ustoichivost neszhimaemoi zhidkosti [*Convective stability of an incompressible fluid*]. Moscow: Nauka [in Russian].

2 Grigoriev, V.V, & Zhakharov, R.E. (2017). Chislennoe modelirovanie dvumernoi konvektsii Releia–Benara [Numerical modeling of the two-dimensional Rayleigh-Benard convection]. *Matematicheskie zametki SVFU — Mathematical Notes of NEFU, 24(1),* 87–98 [in Russian].

3 Lyubimova, T.P., Sadilov, E.S., & Prokopev, S.A. (2017). Onset of Soret-induced convection in a horizontal layer of ternary fluid with fixed vertical heat flux at the boundaries. *European Physical Journal E,* 40, 15.

4 Bejan, A. (2013). *Convection heat transfer*. Hoboken, NJ, USA: John Wiley & Sons.

5 Znamenskaya, I.A. (2021). Metody panoramnoi vizualizatsii i tsifrovogo analiza teplofizicheskikh polei. Obzor [Methods for panoramic visualization and digital analysis of thermophysical flow fields. A Review]. *Nauchnaia vizualizatsiia — Scientific Visualization, 13(3),* 125–158 [in Russian].

6 Settls, G.S. (2006). Schlieren and shadowgraph techniques. Visualizing phenomena in transparent media. Berlin: Springer.

7 Brunton, S.L., Noack, B.R., & Koumoutsakos P. (2020). Machine Learning for Fluid Mechanics. *Annual Review of Fluid Mechanics, 52,* 477–508.

8 Harel, R., Rusanovsky, M., Fridman, Y., Shimony, A., & Oren G. (2020). Complete deep computer-vision methodology for investigating hydrodynamic instabilities. *High Performance Computing. ISC High Performance 2020. Lecture Notes in Computer Science, 12321,* 61–80.

9 Alyamovsky, A.A., Sobachkin, A.A., Odintsov, E.V., Kharitonovich, A.I., & Ponomarev, N.B. (2008). Kompiuternoe modelirovanie v inzhenernoi praktike [Computer modeling in engineering practice]. Saint Petersburg: BHV-Petersburg [in Russian].

10 Zhavrin, Yu.I., Kosov, N.D., Belov, S.M., & Tarasov, S.B. (1984). Vliianie davleniia na ustoichivost diffuzii v nekotorykh trekhkomponentnykh gazovykh smesiakh [Influence of pressure on the stability of diffusion in some three-component gas mixtures]. *Zhurnal tekhnicheskoi fiziki — Journal of Technical Physics, 54(5),* 943–947 [in Russian].

11 Zhavrin, Yu.I., Kosov, V.N., Kul'zhanov, D.U., & Karataeva, K.K. (2000). Effect of the pressure on the type of mixing in a three-component gas mixture containing a component possessing the properties of a real gas. *Technical Physics Letters, 26(13),* 1108-1109.

12 Dil'man, V.V., Lipatov, D.A., Lotkhov, V.A., & Kaminskii, V.A. (2005). Instability in unsteady-state evaporation of binary solutions into an inert gas. *Theoretical Foundations of Chemical Engineering, 39(6),* 566–572.

13 Asembaeva, M.K., Kosov, V.N., Krasikov S.A., & Fedorenko O.V. (2019). Effect of the channel inclination angle on convective mixing caused by instability of mechanical equilibrium of ternary gas mixture at isothermal diffusion. *Technical Physics Letters, 45(11),* 1071–1074.

14 Zhavrin, Yu.I., Kossov, V.N., Kulzhanov, D.U., & Fedorenko, O.V. (2015). Eksperimentalnye metody issledovaniia diffuzii i kontsentratsionnoi gravitatsionnoi konvektsii, vyzvannoi neustoichivostiu mekhanicheskogo ravnovesiia v mnogokomponentnykh gazovykh smesiakh [*Experimental methods for studying diffusion and concentration gravitational convection caused by the instability of mechanical equilibrium in multicomponent gas mixtures*]. Almaty: Qazaq universiteti [in Russian].

15 Kosov, V.N., Zhavrin, Yu.I., Fedorenko, O.V., & Mukamedenkyzy, V. (2014). Instability of mechanical equilibrium during diffusion in a three-component gas mixture in a vertical cylinder with a circular cross section. *Technical Physics, 59(4),* 482-486.

16 Aleksandrov, O.E., & Seleznev, V.D. (2016). Pressure dependence of the mixing rate for the free convection of a binary gas mixture in a two-flask apparatus. *Technical Physics, 61(7),* 982–986.

17 Dil'man. V.V., & Lotkhov, V.A. (2015). Molecular turbulent evaporation in a gravitational field. *Theoretical Foundations of Chemical Engineering, 49(1),* 102–106.

18 Bird, B.R., Stewart, W.E., & Lightfoot, E.V. (2002). Transport phenomenon. New York: John Wiley and Sons, Inc.

19 Emelyanov, V.N., & Volkov, K.N. (2018). Vizualizatsiia dannykh fizicheskogo i matematicheskogo modelirovaniia v gazovoi dinamike [Visualization of physical and mathematical modeling data in gas dynamics]. Moscow: Fizmatlit [in Russian].

20 Chetverushkin, B.N., Khankhasaeva, Y.V., Znamenskaya, I.A., & Lutsky A.E. (2021). Numerical simulation of the interaction and evolution of discontinuities in a channel based on a compact form of quasi-gasdynamic equations. *Mathematical models and computer simulations, 13(1),* 26-36.

21 Alyamovsky, A.A. (2015). SolidWorks Simulation. Inzhenernyi analiz dlia professionalov: zadachi, metody, rekomendatsii [SolidWorks Simulation. Engineering analysis for professionals: tasks, methods, recommendations]. Moscow: DMK Press [in Russian].

22 Cherny, S.G., Shashkin, P.A., & Gryazin, Yu.A. (1999). Chislennoe modelirovanie prostranstvennykh turbulentnykh techenii neszhimaemoi zhidkosti na osnove k-ε modelei [Numerical modeling of spatial turbulent flows of an incompressible fluid based on *k-ε* models]. *Vychislitelnye tekhnologii — Computational technologies, 4(2),* 74–94 [in Russian].

23 Kosov, V.N., Zhavrin, Y.I., & Seleznev, V.D. (1998). Inversion of the density gradient and the diffusion "gate" in isothermal mixing of gases. *Technical Physics, 43(5),* 488–492.

DOI 10.31489/2023PH1/59-70

UDK 536.24

D.Y. Kurmanova[1], N. Zh. Jaichibekov[1*], A.G. Karpenko[2], K.N. Volkov[3]

[1]*Gumilyov Eurasian National University, Astana, Kazakhstan;*
[2]*Saint-Peterburg State University, Saint-Peterburg, Russia;*
[3]*Kingstone University, London, SW15 3DW, Great Britain*
*(*e-mail: jaich@mail.ru)*

Numerical modeling and calculation of heat transfer between heat carriers in heat exchangers

Heating of oil and oil products is widely used to reduce energy loss during transportation. An approach is being developed to determine the effective length of the heat exchanger and the temperature of the cold heat carrier at its outlet in the case of a strong dependence of oil viscosity on temperature. The oil of the Uzen field (Kazakhstan) is considered as a heated heat carrier, and water is considered as a heating component. The method of the average-logarithmic temperature difference, modified for the case of variable viscosity, and methods of computational fluid dynamics are used for calculations. The results of numerical calculations are compared with the data obtained on the basis of a theoretical approach at constant viscosity. When using a theoretical approach with constant or variable viscosity, the heat transfer coefficients to cold and hot heat carriers are found using criterion dependencies. In the case of variable oil viscosity, the transition of the laminar flow regime to the turbulent one is manifested, which has a significant effect on the effective length of the heat exchanger. To solve this problem comprehensively, a mathematical model of hydrodynamics and heat transfer of heat carriers has been developed and multiparametric numerical calculations have been performed using the "Ansys Fluent" software package.

Keywords: power engineering, heat transfer, heat carrier, viscosity, hydrodynamics, oil products, numerical modeling, laminar-turbulent transition.

Introduction

The change in the qualitative state of the raw material base leads to the development and involvement in the operation of oil fields with a high content of paraffins, resins, asphaltenes. The development of such fields requires the use of unconventional methods of oil production and its preparation for transportation. Light oil products (petroleum, kerosene) are easily transported through pipelines at any time of the year and operations with them do not cause any difficulties. Operations with dark oil products (fuel oil, lubricating oils) and crude oil cause significant difficulties due to the fact that dark oil products become more viscous when the air temperature decreases, and their transportation without heating becomes impossible. For pipeline transportation of oil and oil products, an approach based on the regulation of the rheological properties of oil is used, for example, by heating oil with its subsequent transportation through a pipeline with increased thermal insulation (hot oil pumping). In some cases, an increase in the viscosity of oil with a decrease in temperature leads to unacceptable stresses on the walls of the pipe and stops transportation.

Heat exchange processes are carried out in heat exchangers of various types and designs [1-5]. Various heat carriers are used for heating, for example, hot water or water vapor. Energy consumption is one of the important factors that has a significant impact on the design of the heat exchanger [6]. Shell-and-tube heat exchangers are used in the oil and gas industry, which provide good performance characteristics in a wide range of operating conditions, high reliability and low cost. To determine the efficiency of heat exchange processes, final temperatures and required operating parameters of heat carriers, a thermal calculation is carried out.

The composition of oil (in particular, the content of asphaltenes, resins, paraffins) has a significant effect on the dependence of viscosity on temperature [7, 8]. Empirical formulas describing the change in kinematic viscosity depending on temperature have the form of various functions (exponential, polynomial, power, etc.), which are characterized by the presence of coefficients depending on properties of the liquid. Constant coefficients are determined based on the values of the measured kinematic viscosities at experimental points. The generalized Lee–Kessler equation of state is used to calculate the thermodynamic parameters of oil, gas condensates and their fractions [9]. In [10], studies of the dependence of the kinematic viscosity of oil and oil mixtures on temperature were carried out, and existing formulas for calculating the kinematic viscosity of oil in main pipelines were analyzed.

The flow of liquid in the inter-tube space of the heat exchanger is complex and depends on many factors. Numerical simulation of heat transfer in heat exchange devices of various designs is carried out in [11, 12]. The results of numerical calculations are used to find optimal ways to intensify heat transfer processes [13-15]. The obtained results indicate a decrease in the influence of the viscosity of the pumped oil on the hydraulic characteristics of the pipeline when pumping in developed turbulent conditions.

In classical heat exchangers, a bundle of pipes for one heat carrier is placed inside the casing through which another heat carrier moves. In the design of helicoid heat exchangers, profiled tubes and screw profile ribs are used, with the help of which heat exchange conditions are improved. The tubes in such devices have a small diameter and thin walls (about 0.3 mm). In the case when the viscosity depends on temperature, the flow regime in such thin tubes can vary from laminar to turbulent.

In this paper, a mathematical model of a heat exchanger is developed that takes into account the laminar-turbulent transition. For simplicity, a “pipe-in-pipe” heat exchanger circuit with a thin and smooth inner tube is selected. A method for calculating a direct–flow type heat exchanger is given, in which the working fluid in the inner pipeline is oil (cold heat carrier), and in the outer pipe is water (hot heat carrier). Calculations are carried out for the model design of the heat exchanger both using a theoretical approach based on the method of Log-Mean Temperature Difference (LMTD) at constant and variable viscosity, and on the basis of Computational Fluid Dynamics (CFD). The data obtained within the framework of various approaches are compared with each other, which allow us to conclude about the accuracy of each of the approaches and the possibility of their application in practice.

Dependence of oil viscosity on temperature

The Uzen oil and gas field is located in the Mangistau region of Kazakhstan. Oil fields are located at a depth of 0.9–2.4 km. The density of oil is 844-874 kg/m3, viscosity — 3.4–8.15 $mPa \cdot s$, sulfur content — 0.16–2 %, paraffins 16-22 %, resins — 8-20 %.

In the literature, various dependences of viscosity on temperature are used. In the oil industry, the Walter formula is used to calculate the kinematic viscosity depending on temperature [10]

$$\lg[\lg(\nu + 0.8)] = a + b \lg T, \quad (1)$$

where a and b are empirical coefficients determined experimentally for a given fluid. The coefficients a and b in formula (1) are from the relations

$$a = \lg[\lg(\nu_1 + 0.8)] - b \lg T$$

$$b = \frac{\lg[\lg(\nu_1 + 0.8)] - \lg[\lg(\nu_2 + 0.8)]}{\lg T_1 - \lg T_2},$$

here ν_1 and ν_2 are the values of the kinematic viscosity of the liquid at temperatures T_1 and T_2.

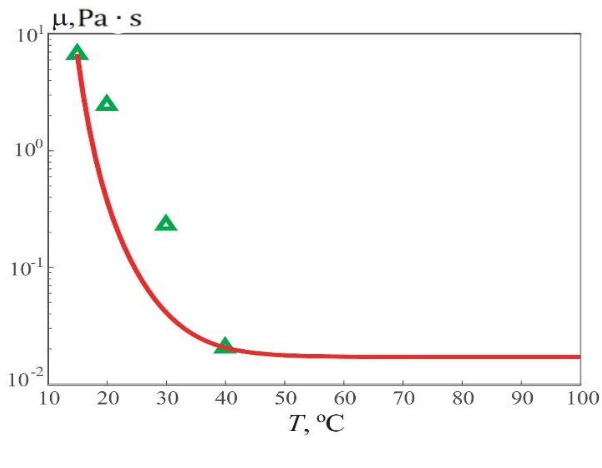

Figure 1. Dependence of the dynamic viscosity of the Uzen oil field on temperature. Triangular icons — experimental data [16], solid line — calculations according to the Walter formula

A comparison of the results of calculations using the Walter formula with experimental values of dynamic viscosity is shown in Figure 1 for the oil of the Uzen field. The temperature varies from 10 to 100 °C. The solid line corresponds to the dependence of viscosity on temperature obtained by the Walter formula (1), and the triangular icons correspond to the results of a physical experiment [16].

Calculation method for constant viscosity

To estimate the heat flows from a hot heat carrier to a cold one, a heat carrier model with a constant viscosity along the length is used, based on the use of an average logarithmic temperature difference. In a recuperative heat exchanger, two liquids with different temperatures move in a space separated by a solid wall (Fig. 2).

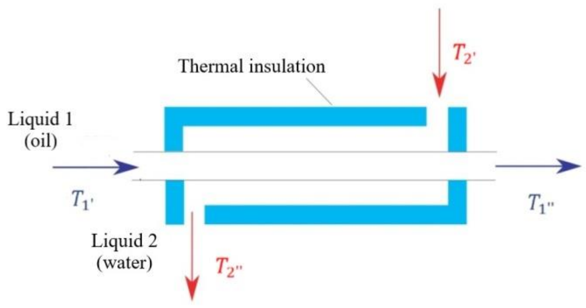

Figure 2. Diagram of a heat exchanger in which heat carriers move in the opposite direction

Thermal calculation is reduced to the joint solution of the equations of thermal balance and heat transfer. The heat balance equation has the form [21]

$$Q = G_1 c_{p1}(T_{1'} - T_{1''}) = G_2 c_{p2}(T_{2''} - T_{2'}) > 0\,, \tag{2}$$

here Q is the amount of heat transferred per unit of time from a hot heat carrier to a cold one, G is the mass flow rate of the heat carrier, c_p is the isobaric heat capacity, $T_{'}$ is the inlet temperature, $T_{''}$ is the outlet temperature. Index 1 corresponds to a hot heat carrier, and index 2 corresponds to a cold heat carrier. The heat transfer equation for a heat exchanger is represented as

$$Q = \bar{k} F \Delta\bar{T}\,, \tag{3}$$

where $\bar{k}$ is the average heat transfer coefficient, which is calculated at an average temperature $(T_{1'} + T_{1''})/2$ and $(T_{2'} + T_{2''})/2$, $\Delta\bar{T}$ is the average temperature difference. The average temperature difference is determined by the expression

$$\Delta\bar{T} = \frac{1}{F}\int_0^F \Delta T\, dF\,,$$

where F is the heat exchange surface area.

Using the notation $\Delta T = (T_1 - T_2)$, equations (2) and (3) in differential form will take the form

$$\frac{d(\Delta T)}{\Delta T} = -mk\,dF, \quad m = \left(\frac{1}{G_1 c_{p1}} \pm \frac{1}{G_2 c_{p2}}\right).$$

The plus sign is selected in the case of a direct–flow apparatus, and the minus sign is selected in the case of a counter-flow heat exchanger. The above equation is valid along the direction of movement of the hot heat carrier. Assuming that m and $\bar{k}$ are constant along the length of the apparatus and integrating from 0 to F and from $\Delta T'$ and ΔT, we obtain

$$\Delta T = \Delta T' \exp\left(-m\bar{k}F\right), \tag{4}$$

where $\Delta T'$ is the temperature difference at the inlet of the hot heat carrier. Along the heat exchange surface, the temperature pressure varies exponentially. By averaging the temperature head over the entire heat exchange surface, the average logarithmic temperature head is from the ratio

$$\Delta\overline{T} = \frac{\Delta T'' - \Delta T'}{\ln(\Delta T'' / \Delta T')}.$$

In the constructive calculation of heat exchange devices, the thermal performance Q is determined by equation (2). The heat exchange surface area F is found from the equation

$$F = \frac{Q}{\overline{k}\Delta\overline{T}}.$$

When calculating the heat exchange surface area, the task is reduced to calculating the average heat transfer coefficient and the average logarithmic temperature pressure. The length of the heat exchanger is calculated by the formula

$$L = \frac{F}{\pi n d},$$

where n is the number of inner tubes, d is their hydraulic diameter.

The temperature distributions along the heat exchange surface are expressed by the relations:

– direct-flow circuit

$$T_1(x) = T_{1'} - \Delta T' \frac{1 - \exp\left[-\overline{k} m F(x)\right]}{1 + (G_1 c_{p1}) / (G_2 c_{p2})}$$

$$T_2(x) = T_{2'} + \Delta T' \frac{1 - \exp\left[-\overline{k} m F(x)\right]}{1 + (G_2 c_{p2}) / (G_1 c_{p1})},$$

here $F(x)$ is the dependence of the heat exchange surface area on the length measured along the path of the hot heat carrier. In the case of a cylindrical surface, the heat exchange area is expressed in terms of length $F(x) = \Pi \cdot x$, where Π is the wetted perimeter of the heat exchange surface.

For the case of thin cylindrical walls, the relations for surface temperatures have the form

$$T_{w1} = \frac{\left(\frac{\alpha_1 F_1}{\alpha_2 F_2} + \frac{\alpha_1 F_1 \delta_w}{\lambda_w F_a}\right) T_1 + T_2}{1 + \frac{\alpha_1 F_1}{\alpha_2 F_2} + \frac{\alpha_1 F_1 \delta_w}{\lambda_w F_a}}$$

$$T_{w2} = \frac{\left(\frac{\alpha_2 F_2}{\alpha_1 F_1} + \frac{\alpha_2 F_2 \delta_w}{\lambda_w F_a}\right) T_2 + T_1}{1 + \frac{\alpha_2 F_2}{\alpha_1 F_1} + \frac{\alpha_2 F_2 \delta_w}{\lambda_w F_a}},$$

here $F_a = (F_1 + F_2)/2$, F_1 is the heat exchange area on the heat carrier side 1, F_2 is the heat exchange area on the heat carrier side 2, δ_w is the wall thickness, λ_w is the thermal conductivity coefficient of the wall, α is the heat transfer coefficient. The above relations for the wall temperature are implicit and require an iterative solution, since the heat transfer coefficient α depends on temperature.

For a single-layer cylindrical wall, the average heat transfer coefficient is calculated as follows

$$\overline{k} = \left(\frac{1}{\overline{\alpha}_1 d_1} + \frac{1}{2\lambda_w} \ln\frac{d_2}{d_1} + \frac{1}{\overline{\alpha}_2 d_2}\right)^{-1},$$

where $\overline{\alpha_1}$ is the average heat transfer coefficient to the cold heat carrier, $\overline{\alpha_2}$ is the average heat transfer coefficient to the hot heat carrier.

The Nusselt number depends on the flow mode (laminar or turbulent) and the heat exchange mode (heating or cooling). The average heat transfer coefficient is expressed in terms of the average length of the Nusselt number $\mathrm{Nu} = \overline{\alpha} d_g / \lambda$, where $d_g = 4F_g / \Pi$ is the effective hydraulic diameter, F_g is the area of the passage section of the channel, Π is the wetted perimeter, λ is the thermal conductivity of the liquid. During the flow in the pipe or during the longitudinal flow around the bundles of pipes, the Nusselt number is calculated using a semi-empirical dependence of the form

$$\mathrm{Nu} = \mathrm{Nu}\left(\mathrm{Re}, \mathrm{Pr}, \mathrm{Pr}_w, L / d_g\right),$$

where Pr is the Prandtl number of the liquid, Pr_w is the Prandtl number of the liquid calculated from the wall temperature. Similarity numbers are calculated from the average temperature of the heat carrier. The Reynolds number is determined by the ratio $\mathrm{Re} = \rho V d_g / \mu$, where V is the characteristic flow velocity, ρ is the density, and μ is the dynamic viscosity.

Calculation method for variable viscosity

In the case of a strong dependence of viscosity on temperature, the heat exchanger is divided into elementary sections along the length. At each site, an assumption is made about a small change in viscosity.

With a weak dependence of the viscosity of the heat carrier on the temperature, the average Reynolds number is based on the average temperature of the heat carrier. Such an assumption does not introduce significant errors in the calculation, since it practically does not affect the flow regime. In the case of a strong dependence of viscosity on temperature, as the heat carrier heats up, the flow mode changes from laminar to developed turbulent. In this case, the local heat transfer coefficient $\alpha(x)$ is calculated, and the relations for the local Nusselt number $Nu_x = \alpha(x) d_g / \lambda$, calculated from local similarity numbers are used

$$\mathrm{Nu}_x = \mathrm{Nu}\left(\mathrm{Re}_x, \mathrm{Pr}_x, \mathrm{Pr}_w, x / d_g\right).$$

The average value of the heat transfer coefficient is found by the formula

$$\overline{\alpha} = \frac{1}{L} \int_0^L \alpha(x) dx .$$

Local Nusselt numbers in laminar and turbulent flow regimes are found using the relations given in [17, 18]. To calculate the local Nusselt number in the laminar flow regime in the pipe, the ratio [18] is used

$$\mathrm{Nu}_x = 4.36 \left(1 + 0.032 \frac{d}{x} \mathrm{Re}_x \mathrm{Pr}_x^{5/6}\right)^{2/5} \left(\frac{\mathrm{Pr}_x}{\mathrm{Pr}_{x,w}}\right).$$

The above ratio is valid at $0.7 < \mathrm{Pr} < 103$. The expression for calculating the local Nusselt number for the turbulent flow regime in a pipe with an additional correction for the change in the Prandtl number has the form [17]

$$\mathrm{Nu}_x = 0.022 \mathrm{Re}_x^{0.8} \mathrm{Pr}_x^{0.43} \left(\frac{\mathrm{Pr}_x}{\mathrm{Pr}_{x,w}}\right)^{0.25} \varepsilon_l ,$$

where

$$\varepsilon_l = \begin{cases} 1, \ x/d \geq 15, \\ \dfrac{1.38}{\left(x/d\right)^{0.12}}, \ x/d < 15 \end{cases}.$$

For the annular channel in the turbulent flow regime, the ratio is used as for the flow in the pipe, but with its equivalent hydraulic diameter.

The heat balance equation for the elementary section in the direction of movement of the hot heat carrier is written as follows

$$\begin{aligned} &\frac{dQ_1}{dx} = G_1 c_{p1}(T_1)\frac{dT_1}{dx}, \frac{dQ_1}{dx} \le 0, \\ &\frac{dQ_2}{dx} = \pm G_2 c_{p2}(T_2)\frac{dT_2}{dx}, \frac{dQ_2}{dx} \ge 0, \quad (5) \\ &\frac{dQ_1}{dx} + \frac{dQ_2}{dx} = 0. \end{aligned}$$

Here dQ_1 is the loss of the amount of heat by the hot heat carrier, dQ_2 is the amount of heat acquired by the cold heat carrier, G is the mass flow of the heat carrier, c_p is the heat capacity, dT is the temperature change. The plus sign corresponds to a direct–flow circuit, and the minus sign corresponds to a counter-flow circuit. The heat transfer equation for an elementary section takes the form

$$\begin{aligned} &\frac{dQ_1}{dx} = k(T_1,T_2)(T_2 - T_1)\frac{dF}{dx}, \frac{dQ_1}{dx} \le 0, \\ &\frac{dQ_2}{dx} = k(T_1,T_2)(T_1 - T_2)\frac{dF}{dx}, \frac{dQ_2}{dx} \ge 0. \end{aligned} \quad (6)$$

Here k is the local heat transfer coefficient, dF/dx is the change in the heat exchange area, which remains constant for a heat exchanger made of straight pipes.

From equations (5) and (6) follows a closed system of equations with respect to the temperatures of heat carriers

$$\begin{aligned} &\frac{dT_1}{dx} = \frac{k(T_1,T_2)}{G_1 c_{p1}(T_1)}(T_2 - T_1)\frac{dF}{dx} \\ &\frac{dT_2}{dx} = \pm\frac{k(T_1,T_2)}{G_2 c_{p2}(T_2)}(T_1 - T_2)\frac{dF}{dx} \end{aligned} \quad (7)$$

Since $dF/dx = const$ and is known, the system of equations (7) is a system of ordinary differential equations with a nonlinear right-hand side. In the case of a direct-flow circuit (plus sign), the Cauchy problem is posed for system (7), and for a counter-current circuit (minus sign), the boundary value problem is solved. In this case, the integration is carried out up to the length L, which is unknown in advance.

The system of equations (7) is solved by the finite difference method on the interval $x \in [0, L]$. To stabilize the iterative process during the linearization of the system, the method of lower relaxation is used. The length of the integration interval L is unknown in advance. Newton's method is used to determine it. The local heat transfer coefficient is found using local heat transfer coefficients.

$$k = \left(\frac{1}{\alpha_1 d_1} + \frac{1}{2\lambda_w}\ln\frac{d_2}{d_1} + \frac{1}{\alpha_2 d_2}\right)^{-1},$$

where α_1 is the local heat transfer coefficient from the cold heat carrier to the wall, α_2 is the local heat transfer coefficient from the side of the hot heat carrier, λ_w is the thermal conductivity coefficient of the tube material.

Numerical simulation of heat transfer

The results of thermal calculations are compared with the data obtained by computational fluid dynamics methods. Oil is considered a Newtonian liquid with a constant density. Calculations are carried out using numerical solutions of Reynolds–Averaged Navier-Stokes equations (Reynolds–Averaged Navier-Stokes, RANS) for a viscous incompressible fluid closed using a turbulence model that takes into account the laminar-turbulent transition.

The SST $k-\omega$ turbulence model is designed for an effective combination of a reliable and accurate $k-\omega$ model in the wall region and a $k-\varepsilon$ model in free flow [19, 20]. To switch between models, a special function is used, which takes a single value in the wall area (the standard $k-\omega$ model is used) and a zero value away from the wall (the $k-\varepsilon$ model is used).

The model taking into account the laminar-turbulent transition (Local-Correlation Transition Model, $\gamma-\mathrm{Re}_{\theta t}$ transition model) is based on a combination of the SST equations of the $k-\omega$ turbulence model with two additional transfer equations for the intermittency parameter γ and the critical Reynolds number $\gamma-\mathrm{Re}_{\theta t}$, constructed from the thickness of the momentum loss [21, 22]. To simplify the model, the equation for $\gamma-\mathrm{Re}_{\theta t}$ is not considered, and in the equation for the intermittency parameter, an assumption is made about the smallness of convective terms [23].This approach leads to algebraic relations for finding the intermittency parameter.

To discretize the basic equations, the finite volume method on unstructured grids and the SIMPLE method are used [24]. The discretization of inviscid flows is carried out using the MUSCL scheme (Monotonic Upstream Schemes for Conservation Laws, monotonic counter–flow circuit for conservation laws), and viscous flows — a centered scheme of the 2nd order of accuracy. The MUSCL scheme makes it possible to increase the order of approximation by spatial variables without losing the monotony of the solution, satisfies the TVD (Total Variation Diminishing) condition and is a combination of centered finite differences of the 2nd order and a dissipative term, for switching between which a flow limiter built on the basis of characteristic variables serves. The geometric multigrid method is used to solve the system of difference equations [25].

The calculations use a grid consisting of 19461 cells, of which 500×24 cells are placed in an area filled with oil, 500×5 cells in an area made of steel, and 500×13 cells in an area filled with water. The mesh cells are thickened near the walls of the pipe so that $y+<2$, where $y+$ is a dimensionless wall coordinate.

Calculation results and discussion

The diagram of the direct-flow type heat exchanger is shown in Figure 3 (dimensions are given in millimeters). The *h* index corresponds to the hot medium (water), the *c* index corresponds to the cold medium (oil). The *i* and *o* indexes refer to the input and output cross-sections.

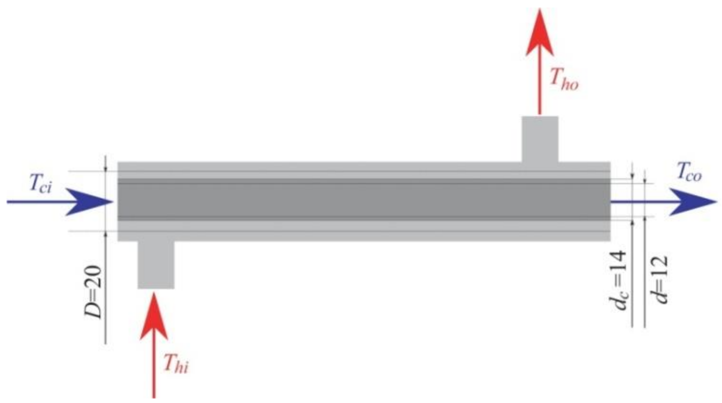

Figure 3. Diagram of a direct-flow type heat exchanger

To calculate the effective length of the heat exchanger and the temperature of the hot heat carrier at the outlet, the parameters given in Table 1 are set (the input and output temperatures of the cold heat carrier, the input temperature of the hot heat carrier, the speeds of both heat carriers, the flow rates of the hot and cold heat carrier, the geometric characteristics of the inner and outer tubes, as well as the physical properties of the tube material).

Table 1

Input data for thermal calculation

Parameter	Unit of measurement	Symbol	Quantity
Number of tubes	piece	n	1
Tube wall thickness	mm	δ_w	1
Inner diameter of the tubes	mm	d	12
Outer diameter of the tubes	mm	d_c	14
Inner diameter of the shell	mm	D	20
Temperature of the hot heat carrier at the inlet	K	T_{hi}	423
Consumption of hot heat carrier	кg/s	G_h	0.6386
The speed of the hot heat carrier	m/s	v_h	4
The temperature of the cold heat carrier at the inlet	K	T_{ci}	303
The temperature of the cold heat carrier at the outlet	K	T_{co}	328
Consumption of cold heat carrier	кg/s	G_c	0.3814
The speed of the cold heat carrier	m/s	v_c	4

To determine the temperature of the hot heat carrier at the outlet and the corresponding effective length of the heat exchanger, the heat balance equations are used. Solving the heat balance equations by the finite difference method, we obtain the distributions of the average mass temperatures of the heat carriers given in Table 2.

Table 2

Calculation results

Heat carrier model	With constant viscosity	With variable viscosity
Length, m	5.28	4.26
The temperature of the hot heat carrier at the outlet, K	416	416

The obtained results are compared with the numerical simulation data. Figure 4 shows the distribution of the average mass temperature of oil (cold heat carrier) along the length of the heat exchanger, obtained using the finite difference method and based on numerical modeling.

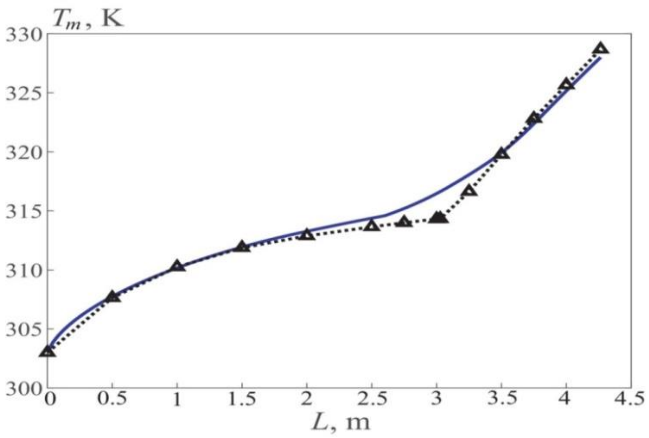

Figure 4. Distribution of the average mass temperature of oil along the length. The solid line corresponds to the results obtained on the basis of the theoretical approach, and the dotted line with triangular icons corresponds to the results of numerical calculations.

The average mass temperature of oil increases along the length due to heating from a heat source (hot heat carrier). The results of analytical and numerical calculations are in good agreement with each other.
The distributions of the average mass temperature of water (hot heat carrier) along the length, obtained on the basis of analytical and numerical calculations, are shown in Figure 5.

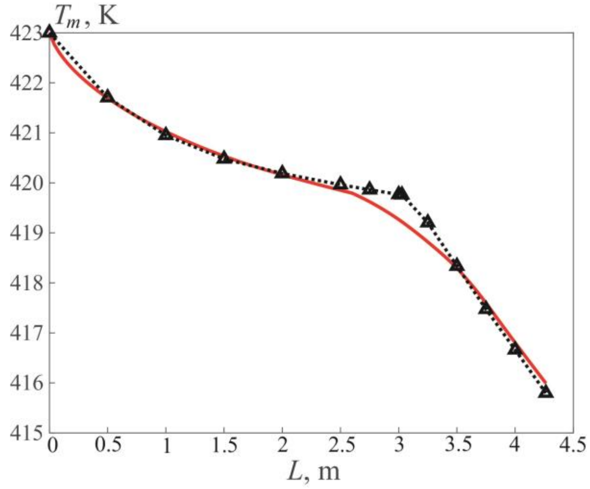

Figure 5. Distribution of the average mass temperature of water along the length. The solid line corresponds to the results obtained on the basis of the theoretical approach, and the dotted line with triangular icons corresponds to the results of numerical calculations.

Compared with the results shown in Figure 4, the average mass temperature of water decreases along the length of the pipe due to heat transfer from it to the cold heat carrier. It should also be noted that the results of calculations obtained on the basis of different approaches are well coordinated.

From the results shown in Figures 4 and 5, it is possible to notice characteristic changes in the curvature of the lines at a distance of about 2.5 m from the input section, where in both cases there are sharp changes in temperature gradients with corresponding signs. This transition occurs at the distance where the laminar flow regime turns into a turbulent one. Figure 6 shows a graph of the temperature distribution along the inner wall of the tube from the oil side. It can be seen that at the entrance the oil is cold and the wall cools down strongly from the oil side, then it warms up, heat exchange by thermal conductivity prevails here, then a laminar-turbulent transition occurs and heat transfer increases significantly and the wall temperature decreases.

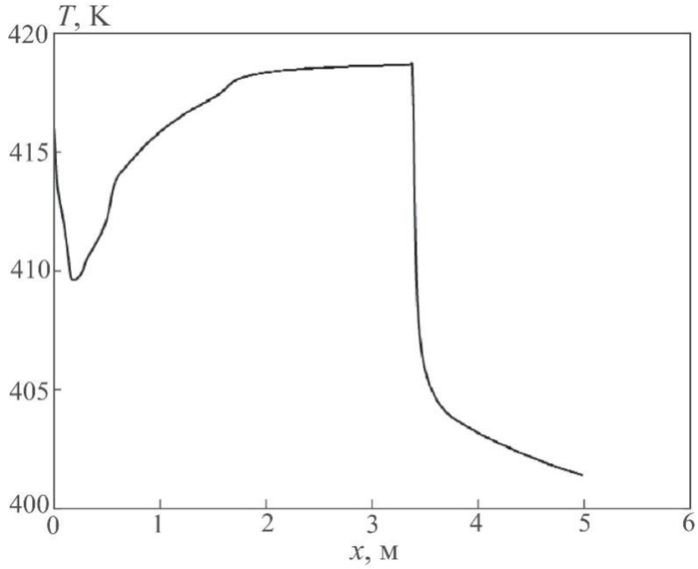

Figure 6. Temperature distribution along the tube wall from the oil side

Conclusion

Reducing the viscosity of oil by heating it is one of the ways to increase the energy efficiency of the process of pumping high-viscosity oil during production and transportation. Numerical modeling allows solving a number of issues related to increasing the efficiency of heat transfer, which remains one of the most important in the design of heat exchange devices in the oil and gas industry.

Thermal and numerical calculations were carried out to determine the length of the heat exchanger and the temperature of the cold heat carrier in the outlet section in the case of constant and variable oil viscosity. With variable viscosity of oil, the transition from laminar to turbulent mode is manifested, while with the analytical method of calculation for constant viscosity, this effect is not taken into account. The obtained results show that a model with a constant viscosity leads to an underestimation of the length of the heat exchanger by about 20 % compared to calculations that take into account the dependence of oil viscosity on temperature.

References

1 Fukai J. Convection heat transfer in a shell and tube heat exchanger using sheet fins for effective utilization of energy / J. Fukai, H. Mitani, K. Nakaso // International Journal of Heat and Mass Transfer. — 2015. — Vol. 82. — P. 581–587.

2 Wang Y. Characteristics of heat transfer for tube banks in crossflow and its relation with that in shell-and-tube heat exchangers / Y. Wang, X. Gu, Z. Jin, K. Wang // International Journal of Heat and Mass Transfer. — 2016. — Vol. 93. — P. 584–594.

3 Araavind S. CFD analysis of shell and tube heat exchanger for pre-heating of biodiesel / S. Araavind, A.S. Athreya // International Journal of Advance Research in Science and Engineering. — 2017. — Vol. 6, No. 7. — P. 687–693.

4 Abda A.A. Performance analysis of shell and tube heat exchanger: parametric study / A.A. Abda, M.Q. Kareema, S.Z. Najib // Case Studies in Thermal Engineering. — 2018. — Vol. 12. — P. 563–568.

5 Лычаков В.Д. Анализ теплоотдачи сборок оребренных теплообменных аппаратов / В.Д. Лычаков, М.Ю. Егоров, А.А. Щеглов, А.С. Сивоволов, А.С. Матяш, Б.Ф. Балунов // Теплоэнергетика. — 2022. — № 3. — С. 63–72.

6 Darbandi M. A new developed semi-full-scale approach to facilitate the CFD simulation of shell and tube heat exchangers / M. Darbandi, M.-S. Abdollahpour, M. Hasanpour-Matkolaei // Chemical Engineering Science. — 2021. — Vol. 245, No. 6. — P. 116836.

7 Bizhan K.G. Prediction of kinematic viscosity of oil fractions using artificial neural networks / K.G. Bizhan, R.D. Mohammad, P. Hossein // Iranian Journal of Oil and Gas Science and Technology. — 2014. — Vol. 3, No. 2. — P. 51–65.

8 Boda M.A. Analysis of kinematic viscosity for liquids by varying temperature / M.A. Boda, P.N. Bhasagi, A.S. Sawade, R.A. Andodgi // International Journal of Innovative Research in Science, Engineering and Technology. — 2015. — Vol. 4, No. 4. — P. 1951–1954.

9 Lee B.I. A generalized thermodynamic correlation based on three-parameter corresponding states / B.I. Lee, M.G. Kesler // AIChE Journal. — 1975. — Vol. 21, No. 3. — P. 510–527.

10 Аралов О.В. Исследование методов расчета кинематической вязкости нефти в магистральном нефтепроводе / О.В. Аралов, И.В. Буянов, А.С. Саванин, Е.И. Иорданский // Наука и технологии трубопроводного транспорта нефти и нефтепродуктов. — 2017. — Т. 7, № 5. — С. 97–105.

11 Yogesh S.S. Heat transfer and pressure drop characteristics of inclined elliptical fin tube heat exchanger of varying ellipticity ratio using CFD code / S.S. Yogesh, A.S. Selvaraj, D.K. Ravi, T.K.R. Rajagopal // International Journal of Heat and Mass Transfer. — 2018. — Vol. 119. — P. 26–39.

12 Chen K. Effects of non-uniform fin arrangement and size on the thermal response of avertical latent heat triple-tube heat exchanger / K. Chen, H.I. Mohammed, J.M. Mahdi, A. Rahbari, A. Cairns, P. Talebizadehsardari // Journal of Energy Storage. — 2022. — Vol. 45. — P. 103723.

13 Osley W.G. CFD investigation of heat transfer and flow patterns in tube side laminar flow and the potential for enhancement / W.G. Osley, P. Droegemueller, P. Ellerby // Chemical Engineering Transactions. — 2013. — Vol. 35. — P. 997–1002.

14 Karar O. Experimental and numerical investigation on convective heat transfer in actively heated bundle-pipe / O. Karar, S. Emani, S.M. Gounder, M.M. Myo Thant, H. Mukhtar, M. Sharifpur, M. Sadeghzadeh // Engineering Applications of Computational Fluid Mechanics. — 2021. — Vol. 15, No 1. — P. 848–864.

15 Rana S. CFD approach for the enhancement of thermal energy storage in phase change material charged heat exchanger / S. Rana, M. Zunaid, R. Kumar // Case Studies in Thermal Engineering. — 2022. — Vol. 33. — P. 101921.

16 Тугунов П.И. Типовые расчеты при проектировании и эксплуатации нефтебаз и нефтепроводов / П.И. Тугунов, В.Ф. Новоселов, А.А. Коршак, А.М. Шаммазов. — М.: Дизайн Полиграф Сервис, 2002. — 234 с.

17 Исаченко В.П. Теплопередача / В.П. Исаченко, В.А. Осипова, А.С. Сукомел. — М.: Энергия, 1965. — 488 с.

18 Михеев М.А. Основы теплопередачи / М.А. Михеев, И.М. Михеева. — М. Энергия, 1977. — 344 с.

19 Menter F.R. Two-equation eddy-viscosity turbulence models for engineering applications / F.R. Menter // AIAA Journal. — 1994. — Vol. 32, No. 8. — P. 1598–1605.

20 Menter F. Transition modelling based on local variables / F. Menter, T. Esch, S. Kubacki // Engineering Turbulence Modelling and Experiments. Elsevier, — 2002. — P. 555–564.

21 Langtry R.B. Correlation-based transition modeling for unstructured parallelized computational fluid dynamics codes / R.B. Langtry, F.R. Menter // AIAA Journal. — 2009. — Vol. 47, No. 12. — P. 2894–2906.

22 Coder J.G. Computational fluid dynamics compatible transition modeling using an amplification factor transport equation / J.G. Coder, M.D. Maughmer // AIAA Journal. — 2014. — Vol. 52, No. 11. — P. 2506–2512.

23 Menter F.R. A one-equation local correlation-based transition model / F.R. Menter, P.E. Smirnov, T. Liu, R. Avancha // Flow, Turbulence and Combustion. — 2015. — Vol. 95. — P. 583–619.

24 Volkov K. Numerical analysis of Navier–Stokes equations on unstructured meshes / K. Volkov // Handbook on Navier–Stokes Equations: Theory and Analysis. // D. Campos. Nova Science, 2016. — P. 365–442.

25 Volkov K. Multigrid and preconditioning techniques in CFD applications / K.Volkov // CFD Techniques and Thermo-Mechanics Applications // Z. Driss, B. Necib, H.-C. Zhang. Springer International Publishing, 2018. — P. 83–149.

Д.Е. Курманова, Н.Ж. Джайчибеков, А.Г. Карпенко, К.Н. Волков

Жылуалмасу аппараттарындағы жылутасымалдағыштар арасындағы жылуалмасуды сандық модельдеу және есептеу

Тасымалдау кезінде энергия шығынын азайту үшін мұнай мен мұнай өнімдерін жылыту кеңінен қолданылады. Мұнай тұтқырлығы температураға қатты тәуелді болған жағдайда жылуалмасу аппаратының тиімді ұзындығын және оның шығысындағы суық жылутасымалдағыштың температурасын анықтау тәсілі әзірленуде. Жылытылатын жылутасымалдағыш ретінде Өзен кен орнының мұнайы (Қазақстан), ал қыздырғыш компонент ретінде — су қарастырылады. Есептеулер үшін ауыспалы тұтқырлық жағдайында модификацияланған орташа логарифмдік температура айырмашылығының және есептеу сұйықтығының динамикасы әдістері қолданылады. Сандық есептеулердің нәтижелері тұрақты тұтқырлық кезінде теориялық тәсіл негізінде алынған мәліметтермен салыстырылады. Тұрақты немесе айнымалы тұтқырлығы бар теориялық тәсілді пайдаланған кезде суық және ыстық салқындатқыштарға жылу беру коэффициенттері критерийлік тәуелділіктерді пайдалана отырып анықталады. Мұнайдың ауыспалы тұтқырлығы жағдайында ламинарлық ток режимінің турбуленттілікке ауысуы байқалады, бұл жылуалмасу аппаратының тиімді ұзындығына айтарлықтай әсер етеді. Бұл мәселені кешенді шешу үшін гидродинамика мен жылутасымалдаушылардың жылуалмасуының математикалық моделі жасалған және «Ansys Fluent» бағдарламалық кешенінің көмегімен көп параметрлік сандық есептеулер жүргізілді.

Кілт сөздер: энергетика, жылуалмасу, жылутасымалдағыш, тұтқырлық, гидродинамика, мұнайөнімдері, сандық модельдеу, ламинарлы-турбулентті ауысу.

Д.Е. Курманова, Н.Ж. Джайчибеков, А.Г. Карпенко, К.Н. Волков

Численное моделирование и расчет теплообмена между теплоносителями в теплообменных аппаратах

Подогрев нефти и нефтепродуктов широко применяется для уменьшения энергопотерь при транспортировке. Разрабатывается подход к определению эффективной длины теплообменного аппарата и температуры холодного теплоносителя на его выходе в случае сильной зависимости вязкости нефти от температуры. В качестве нагреваемого теплоносителя рассматривается нефть Узеньского месторождения (Казахстан), а в качестве нагревающего компонента — вода. Для расчетов используются методы среднелогарифмической разницы температур, модифицированные для случая переменной вязкости, и вычислительной гидродинамики. Результаты численных расчетов сравниваются с данными, полученными на основе теоретического подхода при постоянной вязкости. При использовании теоретического подхода при постоянной или переменной вязкости коэффициенты теплоотдачи к холодному и горячему теплоносителям находятся с помощью критериальных зависимостей. В случае переменной вязкости нефти проявляется переход ламинарного режима течения в турбулентный, который оказывает существенное влияние на эффективную длину теплообменного аппарата. Для комплексного решения данной задачи разработана математическая модель гидродинамики и теплообмена теплоносителей и проведены многопараметрические численные расчеты с помощью программного комплекса «Ansys Fluent».

Ключевые слова: энергетика, теплообмен, теплоноситель, вязкость, гидродинамика, нефтепродукты, численное моделирование, ламинарно-турбулентный переход.

References

1 Fukai, J., Mitani, H., & Nakaso, K. (2015). Convection heat transfer in a shell and tube heat exchanger using sheet fins for effective utilization of energy. *International Journal of Heat and Mass Transfer, 82,* 581–587.

2 Wang, Y., Gu, X., Jin, Z., & Wang, K. (2016). Characteristics of heat transfer for tube banks in crossflow and its relation with that in shell-and-tube heat exchangers. *International Journal of Heat and Mass Transfer, 93,* 584–594.

3 Araavind, S., & Athreya, A.S. (2017). CFD analysis of shell and tube heat exchanger for pre-heating of biodiesel. *International Journal of Advance Research in Science and Engineering, 6(7),* 687–693.

4 Abda, A.A., Kareema, M.Q., & Najib, S.Z. (2018). Performance analysis of shell and tube heat exchanger: parametric study. *Case Studies in Thermal Engineering, 12,* 563–568.

5 Lychakov, V.D., Egorov, M.Y, Sheglov, A.A., Sivovolov, A.S., Matyash, A.S., & Balunov, B.F. (2022). Analiz teplootdachi sborok orebrennykh teploobmennykh apparatov [Analysis of heat transfer of finned heat exchanger assemblies] *Teploenegetika — Thermal power engineering, 3,* 63–72 [in Russian].

6 Darbandi, M., Abdollahpour, M.-S., & Hasanpour-Matkolaei, M. (2021). A new developed semi-full-scale approach to facilitate the CFD simulation of shell and tube heat exchangers. *Chemical Engineering Science, 245(6),* 116836.

7 Bizhan, K.G., Mohammad, R.D., & Hossein, P. (2014). Prediction of kinematic viscosity of oil fractions using artificial neural networks. *Iranian Journal of Oil and Gas Science and Technology, 3(2),* 51–65.

8 Boda, M.A., Bhasagi, P.N., Sawade, A.S., & Andodgi, R.A. (2015). Analysis of kinematic viscosity for liquids by varying temperature. *International Journal of Innovative Research in Science. Engineering and Technology, 4(4),* 1951–1954.

9 Lee, B.I., & Kesler, M.G. (1975). A generalized thermodynamic correlation based on three-parameter corresponding states. *AIChE Journal, 21(3),* 510–527.

10 Aralov, O.V., Buyanov, I.V., Savanin, A.S., & Iordanskii, E.I. (2017). Issledovanie metodov rascheta kinematicheskoi viazkosti nefti v magistralnom nefteprovode [Investigation of methods for calculating the kinematic viscosity of oil in a trunk pipeline]. *Nauka i tekhnologii truboprovodnogo transporta nefti i nefteproduktov — Science and technology of pipeline transportation of oil and petroleum products, 7(5),* 97–105 [in Russian].

11 Yogesh, S.S., Selvaraj, A.S., Ravi, D.K., & Rajagopal, T.K.R. (2018). Heat transfer and pressure drop characteristics of inclined elliptical fin tube heat exchanger of varying ellipticity ratio using CFD code. *International Journal of Heat and Mass Transfer, 119,* 26–39.

12 Chen, K., Mohammed, H.I., Mahdi, J.M., Rahbari, A., Cairns, A., & Talebizadehsardari, P. (2022). Effects of non-uniform fin arrangement and size on the thermal response of avertical latent heat triple-tube heat exchanger. *Journal of Energy Storage, 45,* 103723.

13 Osley, W.G., Droegemueller, P., & Ellerby, P. (2013). CFD investigation of heat transfer and flow patterns in tube side laminar flow and the potential for enhancement. *Chemical Engineering Transactions, 35,* 997–1002.

14 Karar, O., Emani, S., Gounder, S.M., Myo Thant, M.M., Mukhtar, H., Sharifpur, M., & Sadeghzadeh, M. (2021). Experimental and numerical investigation on convective heat transfer in actively heated bundle-pipe. *Engineering Applications of Computational Fluid Mechanics, 15(1),* 848–864.

15 Rana, S., Zunaid, M., & Kumar, R. (2022). CFD approach for the enhancement of thermal energy storage in phase change material charged heat exchanger. *Case Studies in Thermal Engineering, 33,* 101921.

16 Tugunov, P.I., Novoselov, V.F., Кorshak, A.A., & Shammazov, A.M. (2002). Tipovye raschety pri proektirovanii i ekspluatatsii neftebaz i nefteprovodov [Typical calculations in the design and operation of oil depots and pipelines]. Moscow: Dizain Poligraf Servis, 234 [in Russian].

17 Isachenko, V.P., Osipova, V.A., & Sukomel, A.S. (1965). Teploperedacha [Heat transfer]. Moscow: Energiia [in Russian].

18 Miheev, M.A., & Miheeva, I.M. (1977). Osnovy teploperedachi [Basics of heat transfer]. Moscow: Energiia [in Russian].

19 Menter, F.R. (1994). Two-equation eddy-viscosity turbulence models for engineering applications. *AIAA Journal, 32(8),* 1598–1605.

20 Menter, F., Esch, T., & Kubacki, S. (2002). Transition modelling based on local variables. *Engineering Turbulence Modelling and Experiments. Elsevier,* 555–564.

21 Langtry, R.B., & Menter, F.R. (2009). Correlation-based transition modeling for unstructured parallelized computational fluid dynamics codes. *AIAA Journal, 47(12),* 2894–2906.

22 Coder, J.G., & Maughmer, M.D. (2014). Computational fluid dynamics compatible transition modeling using an amplification factor transport equation. *AIAA Journal, 52(11),* 2506–2512.

23 Menter, F.R., Smirnov, P.E., Liu, T., & Avancha, R. (2015). A one-equation local correlation-based transition model. *Flow, Turbulence and Combustion, 95,* 583–619.

24 Volkov, K. (2016). Numerical analysis of Navier–Stokes equations on unstructured meshes. *Handbook on Navier–Stokes Equations: Theory and Analysis / D. Campos. Nova Science,* 365–442.

25 Volkov, K. (2018). Multigrid and preconditioning techniques in CFD applications. *CFD Techniques and Thermo-Mechanics Applications / Z. Driss, B. Necib, H.-C. Zhang. Springer International Publishing,* 83–149.

DOI 10.31489/2023PH1/71-79

UDK 620.179.14

A.E. Goldshteyn, Kh.Kh. Abakumov

National Research Tomsk Polytechnic University, Russia
(E-mail: algol@tpu.ru)

Mitigation of the effect of variations in the electrical conductivity of the material via two-frequency eddy current testing of the thickness of the electrically conductive wall under significantly varying influence parameters

The paper analyzes feasibility of the two-frequency eddy current method for measuring the thickness of an electrically conductive wall under significantly varying test and influence parameters of the test object — the lift-off between the eddy current probe and the test object surface, and the electrical conductivity of the material. An analytical solution was used to determine the dependence of the two-frequency signal of the surface eddy current probe on the influence parameters of the test object. The informative parameters used to simultaneously mitigate the effect of the two influence parameters were the amplitude of the added high-frequency voltage to determine the lift-off, the phase of the added low-frequency voltage to determine the wall thickness, and the phase of the added high-frequency voltage to suppress variations in the electrical conductivity of the material. The calculated dependences of the informative parameters on the test and influence parameters were analyzed. The use of nonlinear functions of the inverse transformation of the informative parameter into the test parameter was shown to efficiently mitigate the effect of variations in the lift-off on measurement results. A method to suppress variations in the electrical conductivity of the test object material is proposed. It implies the correction of the phase of the added low-frequency voltage by the correction value calculated from the parameters of the lift-off and wall thickness, and high-frequency phase variation caused by varying the electrical conductivity of the material.

Keywords: thickness measurement, surface eddy current probe, signal hodographs, stray parameters, suppression in eddy current testing.

Introduction

Eddy current non-destructive testing methods are widely used to test the electromagnetic and geometric parameters of multilayer electrically conductive products [1, 2].

Technical implementation of the eddy current method used to measure the wall thickness of light alloy drill pipes using a surface eddy current probe (ECP) is described in [3]. It is shown that along with the wall thickness parameter t, the main parameters of the test object that affect the ECP signal during measurement are variations in the lift-off h between the ECP and the surface of the test pipe and the electrical conductivity σ of the pipe material.

Significant variations in test and influence parameters complicate mitigation of the effect of these parameters on measurement results. The most effective solution to this problem is to use a multifrequency magnetic field [4–6]. For two-frequency eddy current testing, the excitation current frequencies are chosen so that the penetration depth of the magnetic field approximately equals half the wall thickness at high frequency f_1 and exceeds the wall thickness at low frequency f_2. In this case, the added high-frequency voltage of the eddy current probe depends on the lift-off h and material electrical conductivity σ, and the added low-frequency voltage depends on the lift-off h, material electrical conductivity σ and wall thickness t.

As shown in [7], conventional methods used to mitigate the effect of stray parameters (phase, amplitude, amplitude-phase) do not always yield the desired result, and the use of nonlinear functions of the inverse transformation of the informative parameter into the test parameter is far more efficient under the specified test conditions.

In [3], it was proposed to use nonlinear functions of the inverse transformation of the phase of the added low-frequency voltage into the test parameter to mitigate the lift-off effect, using the amplitude of the added high-frequency voltage to determine the lift-off values required for computation transformation. The study subject of this work is mitigation of the effect of variations in the electrical conductivity of the wall material on the results of measuring the electrically conductive wall thickness.

Methods and Materials

Figure 1 schematically shows the design of the surface ECP used in the study, which consists of the excitation winding w_{21}, measurement winding w_{21} and compensation winding w_{22}. The number of turns in the measurement and compensation windings is equal: $w_{21} = w_{22} = w_2$. An opposite connection of the measurement and compensation windings in the absence of the test object mutually compensates their initial electromotive force (EMF). Eddy currents generated in the electrically conductive test object located near the ECP cause a signal at the ECP output. The amplitude and phase (complex components) of the applied EMF generally depend on the amplitude and frequency of the excitation current, ECP design parameters, electromagnetic

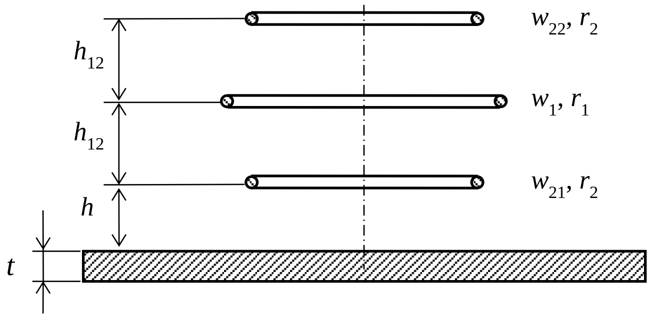

Figure 1. Surface ECP mounted over an electrically conductive plane wall

characteristics of the material and geometric parameters of the test object, and the position of the ECP relative to the test object.

A mathematical model of the interaction between the magnetic field of the eddy current probe and the test object can be created based on well-known analytical solutions proposed in [8, 9]. To simplify the model, it was assumed that the winding cross section is infinitely small, the radii of the excitation winding r_1 and these of the measurement and compensation windings r_2 are equal to the radii of their middle turns, and the test object is of flat shape. In their mathematical structure, the results of the interaction between the ECP and the electrically conductive object having a curved surface (pipe) are similar to mathematical expressions for a flat object, which are adjusted for their numerical values [8].

A plane wall made of a non-magnetic material with the electrical conductivity σ in the range of (14…20) MSm/m with a thickness t in the range of (5…12) mm was used as a test object. The distance between the ECP measuring winding and the test object surface h varied in the range of (0…12) mm.

For the mathematical model, the ECP design used parameters were as follows: excitation winding radius r_1 = 18 mm; radii of the measurement and compensation windings r_2 = 15 mm; the distance between the planes of the turns of the measurement and compensation windings located symmetrically with respect to the excitation winding 2 h_{12} = 22 mm.

With regard to the above, the excitation current frequencies were chosen equal to f_1 = 2500 Hz and f_2 = 125 Hz.

Results and Discussion

According to [8], based on the assumptions, the added relative voltage of the measurement winding can be calculated by the expression:

$$\dot{U}_{21}^{*} = j\frac{1}{F}\int_0^{\infty}\dot{\varphi}_{to}\exp\left(-\frac{h_{12}+2h}{\sqrt{r_1\,r_2}}x\right)\times J_1\left(\sqrt{\frac{r_1}{r_2}}x\right)\times J_1\left(\sqrt{\frac{r_2}{r_1}}x\right)\mathrm{d}x, \qquad (1)$$

where $j=\sqrt{-1}$ is the imaginary unit; J_1 is the Bessel function of the first kind and first order; x is the integration parameter; F is the value proportional to the mutual inductance of the measurement and excitation windings calculated by the expression:

$$F = \int_0^{\infty}\exp\left(-\frac{h_{12}}{\sqrt{r_1\,r_2}}x\right)\times J_1\left(\sqrt{\frac{r_1}{r_2}}x\right)\times J_1\left(\sqrt{\frac{r_2}{r_1}}x\right)\mathrm{d}x,$$

$\dot{\varphi}_{to}$ is the function of the test object, calculated for a non-magnetic material by the expression:

$$\dot{\varphi}_{to} = \frac{-j\beta^2 \,\mathrm{th}\left(t^* \sqrt{x^2 + j\beta^2}\right)}{(2x^2 + j\beta^2)\,\mathrm{th}\left(t^* \sqrt{x^2 + j\beta^2}\right) + 2x\sqrt{x^2 + j\beta^2}},$$

where $t^* = t / r_1$ is the relative wall thickness; $\beta = r_1\sqrt{\omega\sigma\mu_0}$ is the generalized parameter; ω is angular frequency of the excitation current; σ is electrical conductivity of the material; μ_0 is the magnetic constant.
The expression for calculating the relative input voltage of the compensation winding can be obtained from (1) by formal replacement of the value h_{12} by $3h_{12}$.
The resulting value of the added relative voltage of the measurement and compensation windings can be calculated as follows:

$$\dot{U}^*_{\text{add}} = \dot{U}^*_{21} - \dot{U}^*_{22}.$$

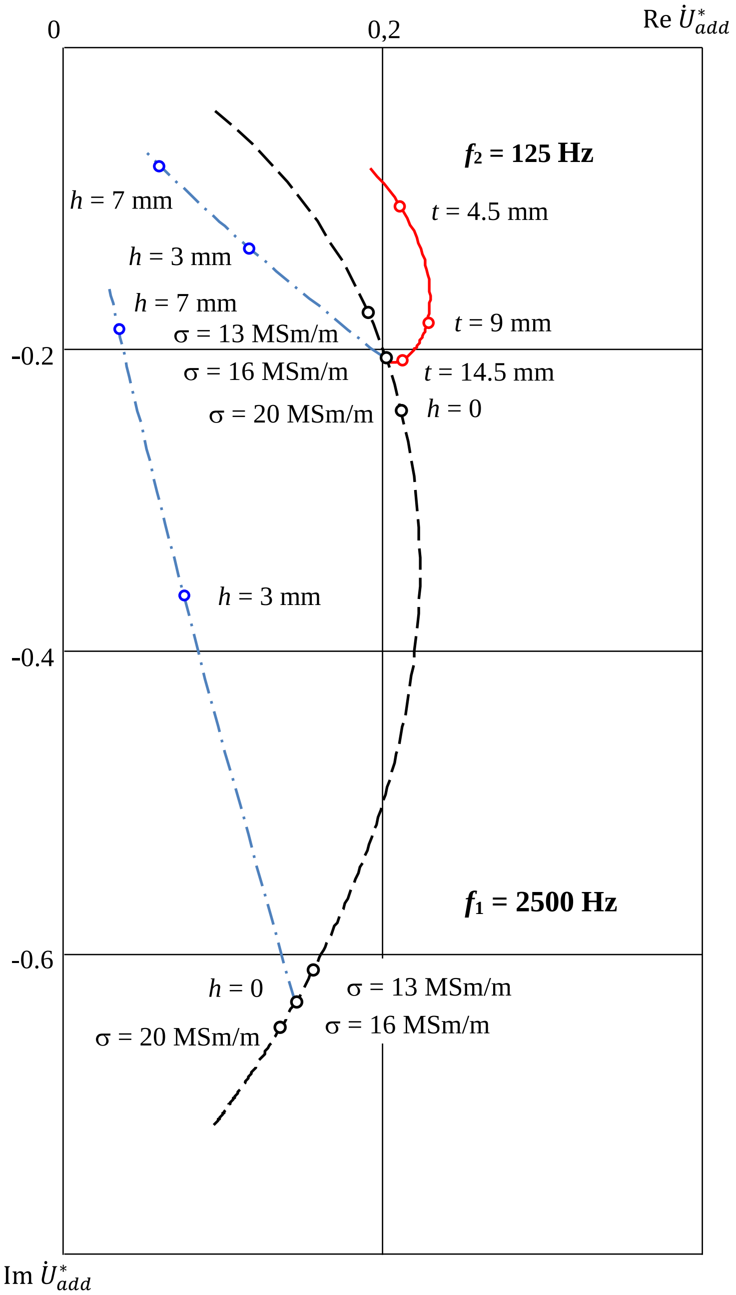

Figure 2. Hodographs of the relative added voltage of the surface ECT versus the variation in the electrical conductivity σ (— —), lift-off *h* (— · –) and thickness *t* (——)

Figure 2 shows hodographs of the added relative voltage of the surface ECP versus variations in electrical conductivity (dashed line), lift-off (dash-dotted lines), and thickness (solid line) calculated using the above analytical expressions for excitation current frequencies of 2500 Hz and 125 Hz.

The phase φ_2 of the added low-frequency voltage is typically used as an informative parameter of the added ECP voltage in two-frequency eddy current testing of the electrically conductive wall thickness *t*. The dependence pattern $\varphi_2(t)$ is monotonic. The analysis of the curves plotted in Figure 2 show that the value of the phase φ_2 depends, to some extent, on the lift-off *h*.

Figure 3 shows the dependence of the informative parameter of the added voltage φ_2 on the test parameter *t* for different values of the lift-off *h*.

The paper [3] proposes an algorithm for computation transformation of the values of the added voltage phase φ_2 and lift-off *h* into the value of the test parameter *t* using non-linear functions of the inverse transformation of the informative parameter into the test parameter. In this case, the electrical conductivity of the wall material was taken equal to a fixed value σ_0. In fact, the electrical conductivity σ of the material can vary in a wide range. Since σ significantly affects the added voltage phase φ_2, variations in the material electrical conductivity during measurement should be suppressed to minimize the measurement error of the test *t*.

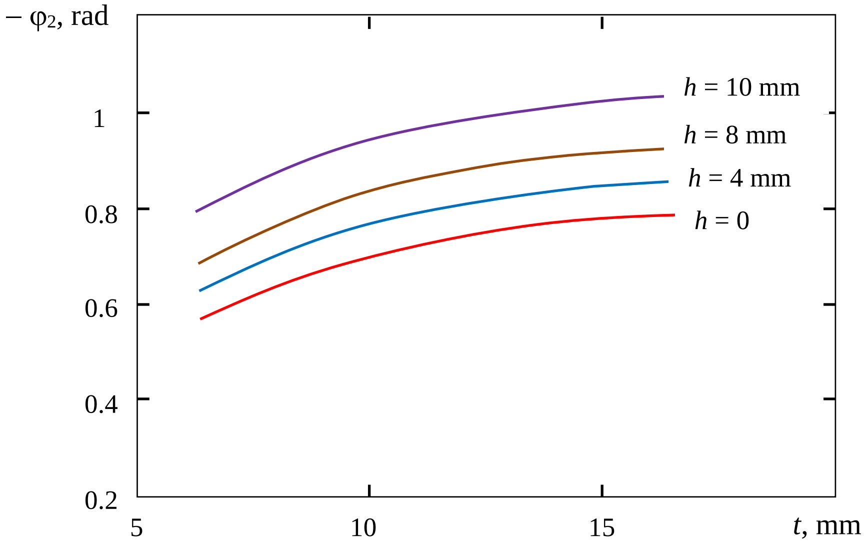

Figure 3. The informative parameter of the added voltage φ_2 versus the test parameter *t* for different lift-off values *h*

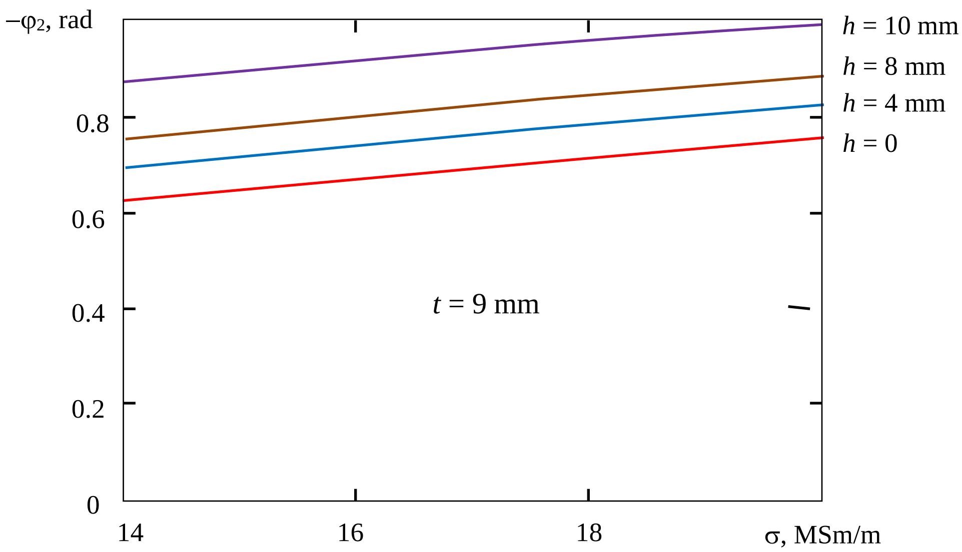

Figure 4. The added voltage phase φ_2 versus electrical conductivity σ for different lift-off values *h*

Figure 4 shows the dependence of the phase of the added low-frequency voltage φ_2 on the electrical conductivity of the material σ calculated using the above analytical expressions for different lift-off values *h* at fixed wall thickness *t* = 9 mm.

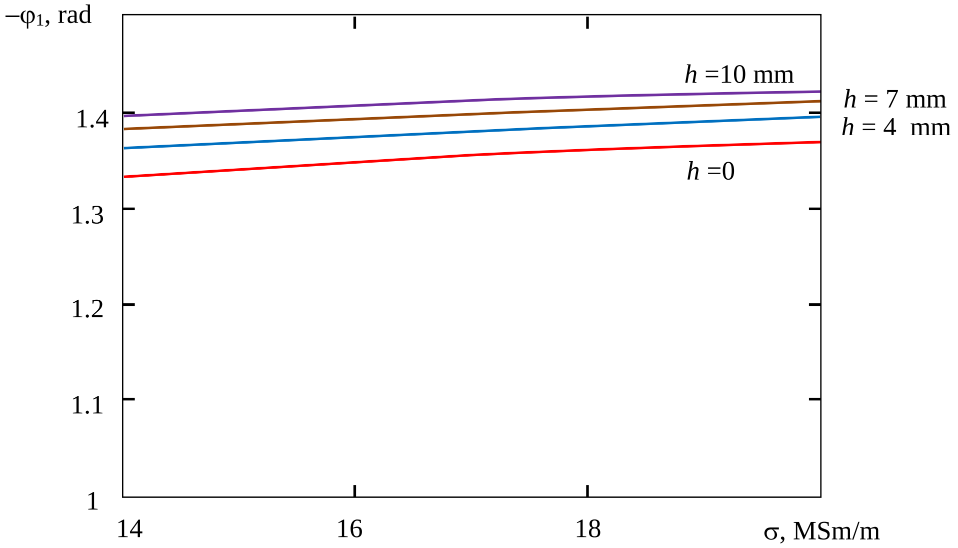

Figure 5. The added voltage phase φ_1 versus electrical conductivity σ for different lift-off values *h*

Figure 5 shows a similar dependence of the phase of the added high-frequency voltage φ_1 on the electrical conductivity σ for different lift-off values *h*.

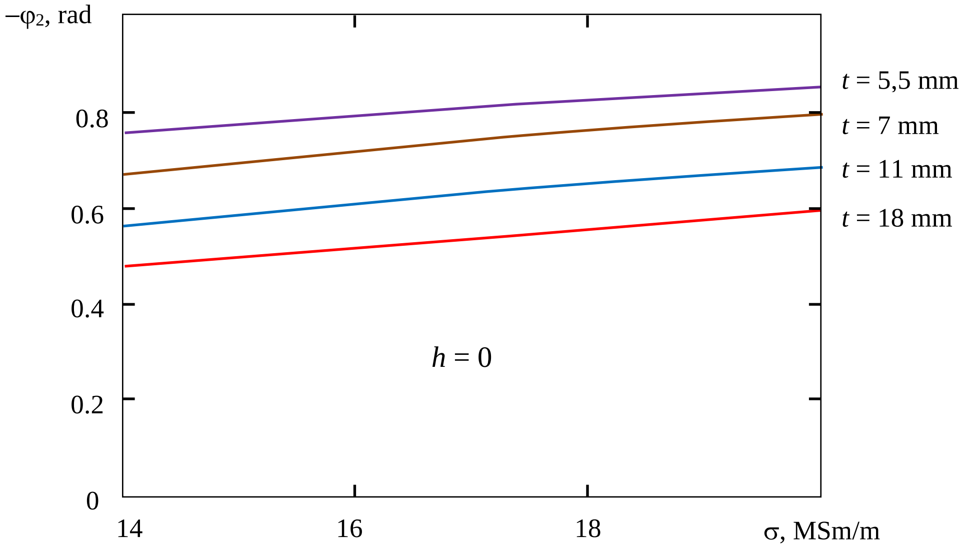

Figure 6. The added voltage phase φ_2 versus electrical conductivity σ for different thickness values *t*

Analysis of the dependencies presented in Figures 4 and 5 shos that both dependencies $\varphi_2(\sigma)$ and $\varphi_1(\sigma)$ are almost directly proportional. The dependences differ in a greater value of the proportionality constant in the first case, and in the dependence of the added low-frequency voltage phase φ_2 on the electrically conductive wall thickness *t* (Fig. 6). The added high-frequency voltage phase φ_1 virtually does not depend on the thickness *t*.

Based on the results of the analysis, a method was proposed for suppression of the variations in the electrical conductivity σ of the material to minimize the measurement error of the test parameter *t*.

The method is as follows. First, the added high-frequency voltage phase φ_{10} is determined at the measured lift-off *h* and the nominal electrical conductivity σ_0 using the dependence shown in Figure 5. For experimental determination of the conversion function, the value of the phase φ_{10} corresponds to the test samples.

After that, we calculate the phase difference $\Delta\varphi_1$ between the measured phase φ_1 of the added high-frequency voltage and its value φ_{10} at the nominal electrical conductivity σ_0:

$$\Delta\varphi_1 = \varphi_1 - \varphi_{10} \ .$$

Next, we determine the phase difference $\Delta\varphi_2$ between the measured phase value φ_2 of the added low-frequency voltage and its value φ_{20} at the nominal electrical conductivity σ_0.

The mathematical and physical modeling show that the phase difference $\Delta\varphi_2$ (due to the difference between the electrical conductivity σ of the test pipe material and its nominal value σ_0) is related to the phase difference $\Delta\varphi_1$ (due to the same reason) through the directly proportional dependence of the form

$$\Delta\varphi_2 = K\,\Delta\varphi_1 ,$$

where *K* is the factor.

K depends on the phases of the added voltages of low (φ_2) and high (φ_1) frequencies, with regard to the above proportional dependencies of the influence parameters for two fixed values of the electrical conductivity σ_1 and σ_2:

$$K = \frac{\varphi_2(\sigma_2, t, h) - \varphi_2(\sigma_1, t, h)}{\varphi_1(\sigma_2, t, h) - \varphi_1(\sigma_1, t, h)} \ .$$

K is the function of the electrically conductive wall thickness *t* and the lift-off *h*. The dependence pattern $K\,(t,\,h)$ is presented in Figure 7. Continuous lines indicate dependencies $K\,(t)$ for different lift-off values *h*.

With an acceptable degree of approximation, these dependencies can be described by polynomas of the first degree (dashed straight lines in Figure 7):

$$K(t,\,h) = a_0 + a_1\,t + a_2\,t\,h + a_3\,h \ ,$$

where a_0, a_1, a_2 and a_3 are the coefficients depending on the values of low f_2 and high f_1 frequencies and the structural parameters of the eddy current probe.

The previously calculated values of the lift-off *h* and the thickness *t* are used to find the multiplier *K*, which is necessary to calculate $\Delta\varphi_2$. Next, we calculate the corrected value of the added low-frequency voltage phase, which corresponds to the nominal electrical conductivity σ_0:

$$\varphi_{20} = \varphi_2 - \Delta\varphi_2 \, .$$

After that, a new corrected phase of the added low-frequency voltage φ_{20} is used to perform recalculation the thickness *t* using the dependence presented in Figure 3. The recalculated thickness *t* is used for consistent calculations of *K*, $\Delta\varphi_2$, φ_{20} and the thickness *t*. The described calculation cycle is repeated (2... 5) times, depending on the required accuracy. The thickness *t* calculated in the last cycle is taken as the final test parameter *t*.

Test samples of different wall thickness used for experimental verification of the results and evaluation of the effectiveness of the proposed method were similar to those used in [3]. The nominal electrical conductivity was 16 MSm/m. The electrical conductivity was changed through changing the sample temperature in the range of (–10…+80) °C. The measurement of the high-frequency voltage phase showed variation in the multiplier *K* used to correct the values of the low-frequency voltage phase in the range from 3.2 to 5.3.

Analysis of the obtained results showed that the method proposed for mitigation of the effect of variations in electrical conductivity minimizes this effect, and the measurement error of the wall thickness *t* in the range of (5...12) mm with the lift-off changing in the range of (2...12) mm does not exceed 5 %.

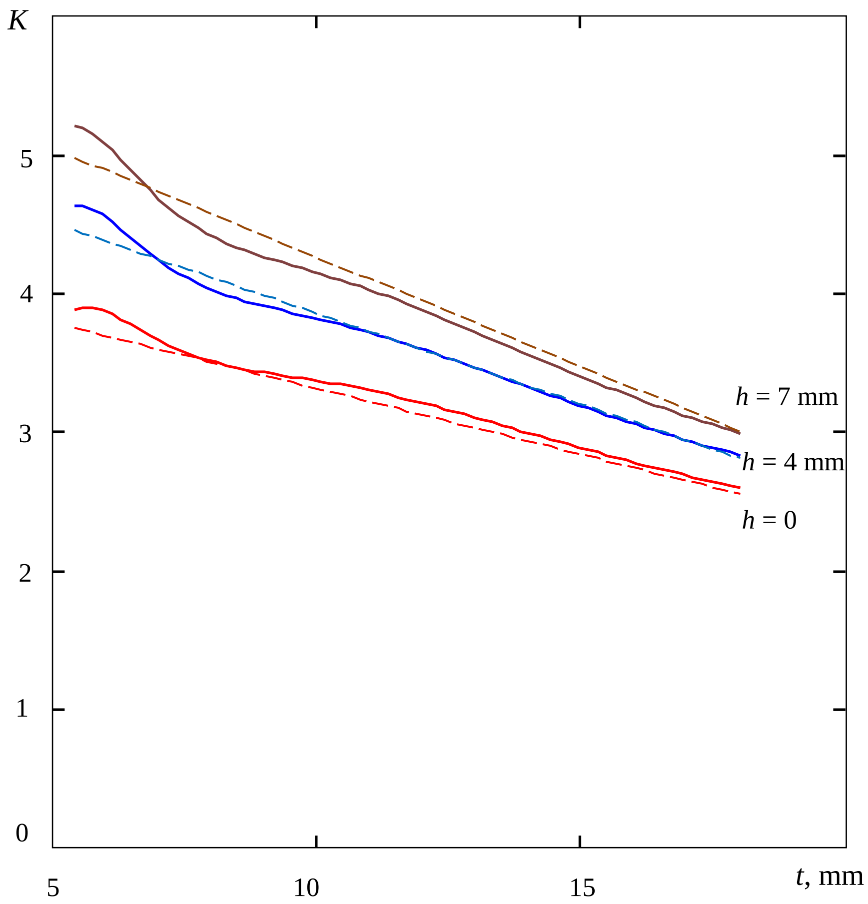

Figure 7. The factor *K* versus the wall thickness *t* and the lift-off *h*

Conclusions

The two-frequency eddy current method can be used for effective measurement of the thickness of a non-magnetic electrically conductive wall with significant variations in both test and influence parameters — the lift-off between the probe and the test object surface, and the electrical conductivity of the material. The method employs such informative parameters of the signal as the added high-frequency voltage amplitude for measuring the lift-off, added low-frequency voltage phase for measuring the wall thickness, and added high-frequency voltage phase for suppressing variations in material conductivity. To mitigate the lift-off effect, a method based on the use of nonlinear functions of the inverse transformation of the informative parameter into the test parameter has been proposed. The method proposed for suppressing variations in the electrical conductivity of the metal is based on correction of the added low-frequency voltage phase by the correction value determined by the values of the lift-off, and wall thickness, and variation in the high-frequency phase due to the changed electrical conductivity of the material. The effectiveness of the proposed methods has been evidenced by the results of mathematical and physical modeling.

References

1 Потапов А.И. Электромагнитные и магнитные методы неразрушающего контроля материалов и изделий / А.И. Потапов, В.А. Сясько, П.В. Соломенчук, А.Е. Ивкин, Д.Н. Чертов // Науч. справоч.-метод. пос.: [В 2-х т.]. — Т. 1:

Электромагнитные и магнитные методы контроля толщины покрытий и стенок изделий. — М.: Изд. дом «Спектр», 2014. — 480 с.

2 Бакунов А.С. Развитие вихретоковой толщинометрии защитных покрытий / А.С. Бакунов, В.А. Калошин // Контроль. Диагностика. — 2016. — № 1. — С. 27–31.

3 Goldshteyn A.E. The use of a two-frequency eddy current method for measuring the electrically conductive wall thickness under significant variations in the test parameter and the lift-off / A.E. Goldshteyn, Kh.Kh. Abakumov // Bulletin of the University of Karaganda-Physics. — 2022. — No. 2 (106). — P. 24–31.

4 Атавин В.Г. Измерение толщины электропроводящих покрытий с отстройкой от зазора и электропроводности основания / В.Г. Атавин, Р.Р. Исхужин, А.И. Терехов // Дефектоскопия. — 2016. — № 5. — С. 32–35.

5 Чернышев А.В. Многочастотный метод контроля для вихретоковой толщинометрии / А.В. Чернышев, И.Е. Загорский, В.И. Шарандо // Вестн. НАН Беларуси. Сер. физ.-техн. наук. — 2019. — Т. 64, № 1. — С. 118–126.

6 Егоров А.В. Вихретоковый контроль металлических материалов с помощью проекционных методов многомерного анализа данных / А.В. Егоров, В.В. Поляков // Дефектоскопия. — 2018. — № 5. — С. 55–62.

7 Тетерко А.Я. Метод многопараметровых вихретоковых измерений толщины, электропроводности материала и толщины диэлектрического покрытия элементов конструкций / А.Я. Тетерко, В.И. Гутник, Г.Г. Луценко, А.А. Тетерко // Техническая диагностика и неразрушающий контроль. — 2014. — № 3. — С. 55–60.

8 Неразрушающий контроль: Справоч. / под ред. В.В. Клюева: [В 7-и т.]. — Т. 2. — [В 2-х кн.]. — Кн. 1. Контроль герметичности. — Кн. 2. Вихретоковый контроль. — М.: Машиностроение, 2003. — 688 с.

9 Шубочкин А.Е. Развитие и современное состояние вихретокового метода неразрушающего контроля: моногр. / А.Е. Шубочкин. — М.: Изд. дом «Спектр», 2014. — 288 с.

А.Е. Гольдштейн, Х.Х. Абакумов

Әсер ететін параметрлердің елеулі өзгерістері жағдайында электр өткізгіш қабырғаның қалыңдығын бақылаудың екіжиілікті құйынды ток әдісін іске асыру кезінде материалдың электр өткізгіштігі өзгерістерінің әсерін анықтау

Бақылау объектісінің бақыланатын және әсер ететін параметрлері — құйынды ток түрлендіргіші мен бақылау объектісінің беті мен материалдың меншікті электр өткізгіштігі арасындағы алшақтықтың елеулі өзгерістері жағдайында электр өткізгіш қабырғаның қалыңдығын құйынды токпен бақылаудың екіжиілікті әдісінің қолданылуы зерттелді. Үстеме құйынды ток түрлендіргішінің екіжиілікті сигналының бақылау объектісінің әсер ететін параметрлеріне тәуелділігін анықтау үшін аналитикалық шешім қолданылды. Бақылау объектісінің екі әсер ететін параметрлерін бір мезгілде түзетуде ақпараттық параметрлер ретінде саңылауды анықтау үшін жоғары жиілікті қолданылатын кернеудің амплитудасын, қабырға қалыңдығын анықтау үшін төмен жиілікті қолданылатын кернеудің фазасын және материалдың меншікті электр өткізгіштігінің өзгеруінен қалпына келтіру үшін жоғары жиілікті қолданылатын кернеудің фазасын пайдалану ұсынылған. Ақпараттық параметрлердің мәндерінің бақыланатын және әсер ететін параметрлерге есептеу арқылы алынған тәуелділігі талданған. Ақпараттық параметрлердің мәндерін бақыланатын параметр мәніне кері түрлендірудің сызықтық емес функциялары саңылауының өзгеруін бақылау нәтижелеріне әсер етуден қалпына келтіру үшін пайдалану тиімділігі атап өтілген. Материалдың меншікті электр өткізгіштігінің өзгеруіне байланысты саңылау мәндерімен, қабырға қалыңдығымен және жоғары жиілікті фазаның өзгеруімен анықталатын түзету шамасына төмен жиілікті енгізілетін кернеудің фазасын түзетуге негізделген бақылау объектісінің металының меншікті электр өткізгіштігінің өзгеруінен түзету әдісі ұсынылды.

Кілт сөздер: қалыңдығын өлшеу, үстеме құйынды ток түрлендіргіші, сигнал годографтары, кедергі параметрлері, құйынды ток бақылауында түзету.

А.Е. Гольдштейн, Х.Х. Абакумов

Отстройка от влияния изменений электропроводности материала при реализации двухчастотного вихретокового метода контроля толщины электропроводящей стенки в условиях значительных изменений влияющих параметров

Исследована применимость двухчастотного метода вихретокового контроля толщины электропроводящей стенки в условиях значительных изменений как контролируемого, так и влияющих параметров объекта контроля — зазора между вихретоковым преобразователем и поверхностью объекта контроля и удельной электрической проводимости материала. Для определения зависимости двухчастотного сигнала накладного вихретокового преобразователя от влияющих параметров объекта контроля использовано аналитическое решение. Для одновременной отстройки от двух влияющих параметров объекта контроля предложено использовать в качестве информативных параметров амплитуду вносимого напряжения высокой частоты для определения зазора, фазу вносимого напряжения низкой частоты для определения толщины стенки и фазу вносимого напряжения высокой частоты для отстройки от изменения удельной электрической проводимости материала. Проанализированы полученные расчетным путем зависимости значений информативных параметров от контролируемого и влияющих параметров. Отмечена эффективность использования для отстройки от влияния на результаты контроля изменений зазора нелинейных функций обратного преобразования значений информативных параметров в значение контролируемого параметра. Предложен метод отстройки от изменения удельной электрической проводимости металла объекта контроля, основанный на коррекции фазы вносимого напряжения низкой частоты на величину поправки, определяемой значениями зазора, толщины стенки и изменением фазы высокой частоты, обусловленным изменением удельной электрической проводимости материала.

Ключевые слова: измерение толщины, накладной вихретоковый преобразователь, годографы сигнала, мешающие параметры, отстройка при вихретоковом контроле.

References

1 Potapov, A.I., Syasko, V.A., Solomenchuk, P.V., Ivkin, A.E., & Chertov, D.N. (2014). Elektromagnitnye i magnitnye metody nerazrushaiushchego kontrolia materialov i izdelii [Electromagnetic and magnetic methods of non-destructive testing of materials and products]. Nauchnoe spravochno-metodicheskoe posobie: [V 2-kh tomakh]. T. 1. Elektromagnitnye i magnitnye metody kontrolia tolshchiny pokrytii i stenok izdelii — Scientific reference manual in 2 volumes: V. 1: Electromagnetic and magnetic methods for controlling the thickness of coatings and walls of products. Moscow: Izdatelskii dom «Spektr» [in Russian].

2 Bakunov, A.S, & Kaloshin, V.A. (2016). Razvitie vikhretokovoi tolshchinometrii zashchitnykh pokrytii [Development of eddy current thickness measurement of protective coatings]. *Control. Diagnostics, 1,* 27–31 [in Russian].

3 Goldshteyn, A.E., & Abakumov, Kh.Kh. (2022). The use of a two-frequency eddy current method for measuring the electrically conductive wall thickness under significant variations in the test parameter and the lift-off. *Bulletin of the University of Karaganda-Physics, 2,* 106, 24–31.

4 Atavin, V.G., Iskhuzhin, R.R., & Terehov, A.I. (2016). Izmerenie tolshchiny elektroprovodiashchikh pokrytii s otstroikoi ot zazora i elektroprovodnosti osnovaniia [Measurement of the thickness of electrically conductive coatings with detuning from the gap and electrical conductivity of the base]. *Defectoscopy, 5,* 32–35 [in Russian].

5 Chernyshev, A.V., Sharando, V.I., & Zagorskij, I.E. (2019) Mnogochastotnyi metod kontrolia dlia vikhretokovoi tolshchinometrii [Multifrequency control method for eddy current thickness measurement]. *Bulletin of the National Academy of Sciences of Belarus. Series of physical and technical sciences, 64(1),* 118–126 [in Russian].

6 Egorov, A.V., Polyakov, V.V. (2018). Vikhretokovyi kontrol metallicheskikh materialov s pomoshiu proektsionnykh metodov mnogomernogo analiza dannykh [Eddy current testing of metallic materials using projection methods of multidimensional data analysis]. *Defectoscopy*, 5, 55–62 [in Russian].

7 Teterko, A.Ya., Gutnik, V.I., Lutsenko, G.G., & Teterko, A.A. (2014). Metod mnogoparametrovykh vikhretokovykh izmerenii tolshchiny elektroprovodnosti materiala i tolshchiny dielektricheskogo pokrytiia elementov konstruktsii [Method of multiparameter eddy current measurements of the thickness, electrical conductivity of the material and the thickness of the dielectric coating of structural elements]. *Tekhnicheskaiia diagnostika i nerazrushaiushchii control — Technical diagnostics and non-destructive testing, 3,* 55–60 [in Russian].

8 Klyuev, V.V. (Ed.). (2003). Nerazrushaiushchii kontrol: Spravochnik: [V 2-kh kn.]. Kn. 1. Kontrol germetichnosti. Kn. 2. Vikhretokovyi kontrol [Nondestructive Testing. Handbook. Tightness testing, 1. Eddy current testing, 2. (Vols 1–7; Vol. 2)]. Moscow: Mashinostroenie [in Russian].

9 Shubochkin, A.E. (2014). Razvitie i sovremennoe sostoianie vikhretokovogo metoda nerazrushaiushchego kontrolia [Development and current status of eddy current testing]. Moscow: Izdatelskii dom «Spektr» [in Russian].

DOI 10.31489/2023PH1/80-87

УДК 536.629.7

P.A. Kissabekova[1]*, D.Zh. Karabekova[1], A.K. Khassenov[1],
V.Yu. Kucheruk[2], A.S. Kudussov[1], Sh.S. Kyzdarbekova[1]

[1]*Karaganda University of the name of academician E.A. Buketov, Karaganda, Kazakhstan;*
[2]*Uman National University of Horticulture, Uman, Ukraine*
**e-mail: pika_1666@mail.ru*

Theoretical foundations of the construction of the operation of heat flow devices

Numerous studies show that non-destructive testing methods satisfy most of the requirements of technical diagnostics of heating networks and technological facilities. Methods of non-destructive testing are based on the observation and automated registration of the temperature state of processes. The developed device is designed to analyze the state of thermal insulation of underground pipelines. The development and research of devices for measuring heat flow requires mandatory consideration of the temperature field of the sensing element, i.e. solutions of the differential equation of thermal conductivity for a body of a certain shape under given boundary conditions. In general, the sensing elements are multi-layered: black coating, calorimetric load, heat-sensitive elements, alternating lacquer and adhesive layers, i.e., the sensing elements are heterogeneous, both in the direction perpendicular to the irradiated surface and in parallel. The heterogeneity in the first case is due to the multi-layering of the sensing element. The article describes solutions to the thermal conductivity equation describing the temperature field of a sensitive element in the form of a hemisphere and a spherical zone, due to the nonequivalence of heat losses during irradiation and calibration by electric current. Taking into account this systematic error makes it possible to increase the accuracy of measuring the energy parameters of radiation. These solutions of the equations formed the basis of the design of the device for measuring heat flow.

Keywords: heat flow, heat flow measuring device, sensing element, temperature field of the sensing element.

Introduction

Heat flow monitoring and measurement devices allow solving energy efficiency and energy saving issues by obtaining reliable data on the source of heat losses and quantitative values. In this regard, the development and creation of heat flow devices for heat supply systems are of particular interest. As the results of numerous studies of thermal insulation of underground heating networks show, the most effective is the method of non-destructive testing based on a comparison of calculated and experimental values of the temperature distribution on the ground surface over heating networks [1, 2].

Non-destructive testing methods use thermal energy coming from the object of control. A temperature anomaly of a fairly regular shape appears on the surface, which differs by several degrees from the average temperature of the detected surface and internal defects deviated from the norm, the presence of local overheating, etc [3].

The initial link of any measuring device or measuring system is the means of obtaining information about the measured value — thermoelectric battery converters. The thermoelectric converter is the primary temperature and heat flow measuring converter. As a thermoelectric battery converter, a sensitive element is used as part of the control and monitoring systems for technological processes. Thermoelectric battery converters, in which the sensing elements are made of metal wires, have received the greatest practical application [4-7].

Problem and research method

In the laboratory “Measurement of Thermal physical quantities” of the Department of engineering thermal physics named after professor Zh.S. Akylbayev of the faculty of physics and technology of academician E.A. Buketov Karaganda University has developed several modifications of heat flow devices based on a thermoelectric battery cell of a special design [8]. A distinctive design of heat flow devices is that it contains a thermoelectric battery converter and a receiving plate, additionally equipped with a thermoelectric refrigerator and a heating element [9]. The devices differ from each other in the shape and size of the sensing element, the number of thermocouples, etc.

To increase the speed and increase the accuracy of measuring the temperature gradient on the surface, we have developed a device for measuring heat flow [10]. A schematic representation of the device for measuring heat flow is shown in Figure 1.

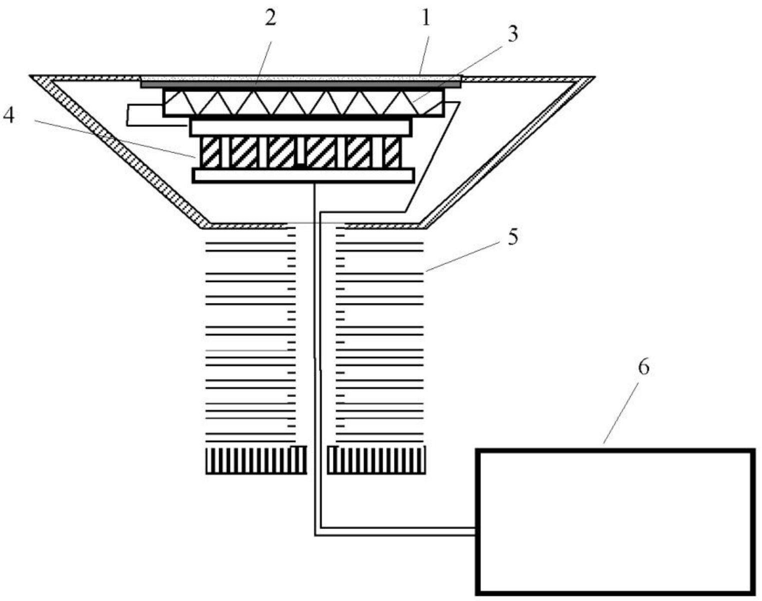

Fig. 1. Schematic representation of a device for measuring heat flow. 1 — insulation layer; 2 — heating element; 3 — thermoelectric battery converter of heat flow; 4 — thermoelectric refrigerator; 5 — radiator; 6 — measuring unit

The radiation flux from a real source incident on the sensitive element of the device has a spice-time heterogeneity, which should be reflected in the boundary conditions of the problem. It is also necessary to take into account the heat exchange of the sensor element with the environment, the device body, etc.

The operation of the device is based on the method of replacing the effect of radiation on the sensing element by the action of an electric current then the presence of a calibration winding should be taken into account in the differential equation of thermal conductivity. In general, the sensing element is multilayer, which means that its thermal physical parameters depend on the coordinates.

The tasks of radiant heating of the body can be replaced by tasks describing the effect of temperature fluctuations of the medium, i.e. the case of irradiation of the body can be considered as a special case of the effect on the body of temperature fluctuations of the adjacent medium. Therefore, it becomes necessary to consider the temperature field of a body of a certain shape placed in a medium with a variable temperature.

Consideration of the temperature field of the sensing element of the heat flow device allows us to obtain new methods for measuring the energy parameters of radiation, including calibration or calibration of the receiver and working formulas for calculating the desired values [11, 12].

Calculations and discussion

The temperature field of a sensing element in the form of a homogeneous spherical zone, a convex or concave surface that is irradiated, is considered. To absorb radiation, this surface is blackened, the non-irradiated surface of the spherical zone exchanges heat with the medium according to Newton's law. Internal heat sources are located between the convex and concave surfaces of the ball zone, creating a heat flow when calibrating the radiation receiver with an electric current.

The thermal conductivity equation for a homogeneous spherical zone has the following form:

$$\frac{1}{a}\frac{\partial T(\mathrm{r},\varphi,\mu,t)}{\partial t}=\frac{1}{r^2}\{\frac{\partial}{\partial r}\left[r^2\frac{\partial T(\mathrm{r},\varphi,\mu,t)}{\partial t}\right]+\frac{\partial}{\partial\mu}\left[\mu^2\frac{\partial T(\mathrm{r},\varphi,\mu,t)}{\partial t}\right]+ \\ +\frac{1}{1-\mu}\frac{\partial T^2(\mathrm{r},\varphi,\mu,t)}{\partial\varphi^2}\}+Q(\mathrm{r},\varphi,\mu,\mathrm{t}) \quad (1)$$

with variable range: $t > 0$; $R_1 < r < R_2$; $0 \le \varphi \le 2\pi$; $\mu_1 < \mu < \mu_2$; $\mu = \cos\theta$; $\theta_1 < \theta < \theta_2$; $\frac{\partial f}{\partial \theta} = \frac{\partial f}{\partial \mu}\frac{\partial \mu}{\partial \theta} = -\sin\theta \frac{\partial f}{\partial \mu}$; where φ and υ — orbital and azimuth angles; R_1 and R_2 — inner and outer radii of the ball zone; $Q(\mathrm{r}, \varphi, \mu, \mathrm{t})$ — the function associated with the power of internal sources $q_\upsilon(\mathrm{r}, \varphi, \mu, t)$ arising during calibration, the expression:

$$Q(\mathrm{r}, \varphi, \mu, \mathrm{t}) = \frac{q_\upsilon(\mathrm{r}, \varphi, \mu, t)}{\lambda}, \qquad (2)$$

where λ is the coefficient of thermal conductivity.

Equation (1) must satisfy the initial condition

$$\mathrm{T}(\mathrm{r}, \varphi, \mu, 0) = f(\mathrm{r}, \varphi, \mu). \qquad (3)$$

Boundary value conditions

$$\frac{\partial T(\mathrm{R}_1, \varphi, \mu, \mathrm{t})}{\partial r} = \frac{\alpha_1}{\lambda}\left[T(\mathrm{R}_1, \varphi, \mu, \mathrm{t}) - \mathrm{T}^*_{1c}(\varphi, \mu, \mathrm{t})\right] \qquad (4)$$

$$\frac{\partial T(\mathrm{R}_2, \varphi, \mu, \mathrm{t})}{\partial r} = -\frac{\alpha_1}{\lambda}\left[T(\mathrm{R}_2, \varphi, \mu, \mathrm{t}) - \mathrm{T}^*_{2c}(\varphi, \mu, \mathrm{t})\right] \qquad (5)$$

$$\frac{\partial T(\mathrm{r}, \varphi, \mu, \mathrm{t})}{\partial \mu} = 0 \qquad (6)$$

and the periodicity condition

$$T(\mathrm{r}, \varphi, \mu, \mathrm{t}) = \mathrm{T}(\mathrm{r}, \varphi + 2\pi, \mu, t), \qquad (7)$$

where α_1 and α_2 are the heat exchange coefficients of the inner and outer surfaces of the sensing element with the medium: $\mathrm{T}^*_{1c}(\varphi, \mu, \mathrm{t})$ and $\mathrm{T}^*_{2c}(\varphi, \mu, \mathrm{t})$ are the equivalent temperatures of the medium at the inner and outer surfaces.

We will replace the variable in this boundary problem:

$$z = \frac{\mu - \mu_1}{\mu_2 - \mu_1}, \qquad (7^*)$$

where: $z = 0$ at $\mu = \mu_1$, $z = 1$ at $\mu = \mu_2$ and $\mu = \mu_1 + \mathrm{z}(\mu_2 - \mu_1)$.

Then equation (1) will take the form:

$$\frac{1}{a}\frac{\partial T}{\partial t} = \frac{1}{r^2}\left\{\frac{\partial}{\partial r}\left[r^2\frac{\partial T}{\partial r}\right] + \frac{\partial}{\partial \mu}\left[(1-\mu^2)\frac{\partial T}{\partial \mu}\right] + \frac{1}{1-\mu^2}\frac{\partial T^2}{\partial \varphi^2}\right\} + Q \qquad (8)$$

with range of change of variables: $t > 0; \mathrm{R}_1 < r < R_2; 0 < \varphi < 2\pi; 0 < z < 1.$

Boundary conditions and periodicity conditions will write down respectively

$$T(\mathrm{r}, \varphi, \mathrm{z}, 0) = \mathrm{f}(\mathrm{r}, \varphi, \mathrm{z}) \qquad (9)$$

$$\frac{\partial T(\mathrm{R}_1, \varphi, \mathrm{z}, \mathrm{t})}{\partial r} = \frac{\alpha_1}{\lambda}\left[T(\mathrm{R}_1, \varphi, \mathrm{z}, \mathrm{t}) - \mathrm{T}^*_{1c}(\varphi, \mathrm{z}, \mathrm{t})\right] \qquad (10)$$

$$\frac{\partial T(\mathrm{R}_1, \varphi, 0, \mathrm{t})}{\partial r} = \frac{\alpha_1}{\lambda}\left[T(\mathrm{R}_1, \varphi, \mathrm{z}, \mathrm{t}) - \mathrm{T}^*_{1c}(\varphi, \mathrm{z}, \mathrm{t})\right] \qquad (11)$$

$$\frac{\partial T(\mathrm{R}_1, \varphi, 0, \mathrm{t})}{\partial \mathrm{z}} = 0 \qquad (12)$$

$$T(\mathrm{r}, \varphi, \mathrm{z}, \mathrm{t}) = \mathrm{T}(\mathrm{r}, \kappa + 2\pi, z, t). \qquad (13)$$

Apply successively to the boundary value problem (8)-(13) integral transformations of the form

$$T(\mathrm{r}, \mathrm{z}, \mathrm{t}) = \int_0^{2\pi} T(\mathrm{r}, \mathrm{z}, \mathrm{t}, \varphi)\,\Phi_n(\varphi)\,\mathrm{d}\varphi \qquad (14)$$

$$T(\mathrm{r,t}) = \int_0^1 T_n(\mathrm{r,z,t})\,\mathrm{K}_{2m}^{2n}(\mathrm{z})\,\mathrm{dz} \quad (15)$$

$$T_{nmk}(\mathrm{t}) = \int_R^{R_2} T_{nm}(\mathrm{r,t})\,\mathrm{R}_{km}(\beta_{km}\,\mathrm{r})\,\mathrm{r}^2\,dr \quad (16)$$

with conversion cores

$$\Phi_n = (\varphi) = \frac{1}{\sqrt{\pi}}\cos 2n\varphi \quad n = 0,1,2... \quad (17)$$

$$K_{2m}^{2n}(z) = \sqrt{\frac{4n+1}{2}\cdot\frac{(2\mathrm{n}-2\mathrm{m})!}{(2\mathrm{n}+2\mathrm{m})!}}P_{2m}^{2n}(\mathrm{t}) \quad n = 0,1,2... \quad m = 0,1,2... \quad (18)$$

$$R_{nm}(\beta_{km}\,\mathrm{r}) = \mathrm{c}_{1k}\,\frac{J_{m+\frac{1}{2}}(\beta_{km}\,\mathrm{r})}{\sqrt{r}} + c_{2k}\,\frac{N_{m+\frac{1}{2}}(\beta_{km}\,\mathrm{r})}{\sqrt{r}}\,v, \quad (19)$$

where $P_{2m}^{2n}(\mathrm{z})$ - associated Legendre polynomial

$$P_{2m}^{2n}(\mathrm{z}) = (1-\mathrm{z}^2)^{2n/2}\,\frac{d^{2n}}{dz^{2n}}P_{2m}(\mathrm{z}), \quad (20)$$

$P_{2m}(\mathrm{z})$ - Legendre polynomials of degree 2m; $J_{m+\frac{1}{2}}(\beta_{km}\,\mathrm{r})$ and $N_{m+\frac{1}{2}}(\beta_{km}\,\mathrm{r})$ - accordingly, the Bessel and Neumann function (m+½) of order; $C_{1к}$ and $C_{2к}$ are determined from the following system of equations:

$$\begin{gathered}-c_k\,\frac{J_{m+\frac{1}{2}}(\beta_{km}\,\mathrm{R}_1)}{2R_1^{3/2}} + c_{1k}\,\frac{J'_{m+\frac{1}{2}}(\beta_{km}\,\mathrm{R}_1)}{2R_1^{1/2}} - c_{1k}\,\frac{\alpha_1}{\lambda}\,\frac{J_{m+\frac{1}{2}}(\beta_{km}\,\mathrm{R}_1)}{2R_1^{1/2}} - \\ -c_{2k}\,\frac{N_{m+\frac{1}{2}}(\beta_{km}\,\mathrm{R}_1)}{2R_1^{3/2}} + c_{2k}\,\frac{N'_{m+\frac{1}{2}}(\beta_{km}\,\mathrm{R}_1)}{2R_1^{3/2}} - c_{2k}\,\frac{\alpha_1}{\lambda}\,\frac{N_{m+\frac{1}{2}}(\beta_{km}\,\mathrm{R}_1)}{2R_1^{1/2}} = 0\end{gathered} \quad (21)$$

$$\begin{gathered}-c_{1k}\,\frac{J_{m+\frac{1}{2}}(\beta_{km}\,\mathrm{R}_1)}{2R^{2/3}} + c_{1k}\,\frac{J'_{m+\frac{1}{2}}(\beta_{km}\,\mathrm{R}_1)}{R_1^{1/2}} - c_{1k}\,\frac{\alpha_2}{\lambda}\,\frac{J_{m+\frac{1}{2}}(\beta_{km}\,\mathrm{R}_1)}{R_1^{1/2}} - \\ -c_{2k}\,\frac{N_{m+\frac{1}{2}}(\beta_{km}\,\mathrm{R}_2)}{2R_1^{3/2}} + c_{2k}\,\frac{N'_{m+\frac{1}{2}}(\beta_{km}\,\mathrm{R}_1)}{R_2^{1/2}} - c_{2k}\,\frac{\alpha_2}{\lambda}\,\frac{N_{m+\frac{1}{2}}(\beta_{km}\,\mathrm{R}_1)}{R_2^{1/2}} = 0\end{gathered} \quad (22)$$

The eigenvalues are found from the equation:

$$\begin{gathered}\left[\frac{J_{m+\frac{1}{2}}(\beta_{km}\,\mathrm{R}_1)}{2R_1^{3/2}} + \frac{J'_{m+\frac{1}{2}}(\beta_{km}\,\mathrm{R}_1)}{R_2^{1/2}} - \frac{\alpha_1}{\lambda}\,\frac{J_{m+\frac{1}{2}}(\beta_{km}\,\mathrm{R}_1)}{R_1^{1/2}}\right]\times \\ \times\left[\frac{N_{m+\frac{1}{2}}(\beta_{km}\,\mathrm{R}_1)}{2R_2^{3/2}} + \frac{N'_{m+\frac{1}{2}}(\beta_{km}\,\mathrm{R}_1)}{R_2^{1/2}} + \frac{\alpha_1}{\lambda}\,\frac{N_{m+\frac{1}{2}}(\beta_{km}\,\mathrm{R}_1)}{R_1^{1/2}}\right] - \\ -\left[-\frac{N_{m+\frac{1}{2}}(\beta_{km}\,\mathrm{R}_1)}{2R_2^{3/2}} + \frac{N'_{m+\frac{1}{2}}(\beta_{km}\,\mathrm{R}_1)}{R_1^{1/2}} - \frac{\alpha_2}{\lambda}\,\frac{J_{m+\frac{1}{2}}(\beta_{km}\,\mathrm{R}_1)}{R_1^{1/2}}\right]\times \\ \times\left[-\frac{J_{m+\frac{1}{2}}(\beta_{km}\,\mathrm{R}_1)}{2R_2^{3/2}} + \frac{J'_{m+\frac{1}{2}}(\beta_{km}\,\mathrm{R}_1)}{R_1^{1/2}} + \frac{\alpha_2}{\lambda}\,\frac{J_{m+\frac{1}{2}}(\beta_{km}\,\mathrm{R}_1)}{R_2^{1/2}}\right] = 0\end{gathered} \quad (23)$$

The conversion formulas for the transformation (14)-(16) have the form:

$$T_n(\mathrm{r},\varphi,\mu,t)=\sum_{n=0}^{\infty}T_n(\mathrm{r},\mu,\mathrm{t})\,\Phi_n(\varphi) \tag{24}$$

$$T_{nm}(\mathrm{r},\mu,t)=\sum_{m=0}^{\infty}T_{nm}(\mathrm{r},\mathrm{t})\,\mathrm{K}_{2m}^{2n}(\mathrm{z}) \tag{25}$$

$$T_{nmk}(\mathrm{r},t)=\sum_{k=0}^{\infty}T_{nmk}(\mathrm{t})\,\mathrm{R}_{km}(\beta_{km}\,\mathrm{r}) \tag{26}$$

Then the solution of the boundary value problem (8)-(13) will be written as 24 and 25:

$$\begin{aligned}T(\mathrm{rt},\varphi,\mathrm{z},t)=&\sum_{n=0}^{\infty}\sum_{m=0}^{\infty}\sum_{k=0}^{\infty}\{\exp(-\alpha\beta_{km}^2\,\mathrm{t})\int_0^1\int_0^{2\pi}\int_{R_1}^{R_2}f(\mathrm{r},\varphi,\mathrm{z})\,\mathrm{r}^2\,\Phi_n(\varphi)K_{2m}^{2n}(\mathrm{z})\,\mathrm{R}_{km}(\beta_{km}\,\mathrm{r})\\&\mathrm{d}\varphi\,\mathrm{dzdr}+a\int_0^t[\int_0^1\int_0^{2\pi}\int_{R_1}^{R_2}Q(\mathrm{r},\varphi,\mathrm{z},\mathrm{t})r^2\Phi_n(\varphi)\,\mathrm{K}_{2m}^{2n}(\mathrm{z})\,\mathrm{R}_{km}(\beta_{nm}\,\mathrm{r})\,\mathrm{d}\varphi\,\mathrm{dzdr}+\frac{R_2^2\alpha_2}{\lambda}\times\\&\times\mathrm{R}_{km}(\beta_{nm}\,\mathrm{R}_2)\int_0^1\int_0^{2\pi}\int_{R_1}^{R_2}T_{2c}^*(\varphi,\mathrm{z},\tau)r^2\Phi_n(\varphi)\,\mathrm{K}_{2m}^{2n}(\mathrm{z})\,\mathrm{R}_{km}(\beta_{nm}\,\mathrm{r})\,\mathrm{d}\varphi\,\mathrm{dzdr}+\frac{R_1^2\alpha_1}{\lambda}\times\\&\times\mathrm{R}_{km}(\beta_{nm}\,\mathrm{R}_1)\int_0^1\int_0^{2\pi}\int_{R_1}^{R_2}T_{1c}^*(\varphi,\mathrm{z},\tau)r^2\,\mathrm{K}_{2m}^{2n}(\mathrm{z})\Phi(\varphi)\,\mathrm{R}_{km}(\beta_{nm}\,\mathrm{r})\,\mathrm{d}\varphi\,\mathrm{dzdr}]\exp[\,-\mathrm{a}\,\beta_{km}^2\times\\&\times(\mathrm{t}-\tau)]\,\mathrm{d}\tau\}\Phi_n(\varphi)\,\mathrm{K}_{2m}^{2n}(\mathrm{z})\,\mathrm{R}_{km}(\beta_{nm}\,\mathrm{r})\end{aligned} \tag{27}$$

The heat release in the sensor element of the device is caused by its heating during calibration by electric current and during absorption of incident radiation. The function in solution (27) is related to the power of internal sources arising during calibration, according to formula (2) by the following expression:

$$Q(\mathrm{r},\varphi,\mathrm{z},\mathrm{t})=\frac{q_\upsilon(\mathrm{r},\varphi,\mathrm{z},\mathrm{t})}{\lambda}. \tag{28}$$

The equivalent temperature of the medium is related to the local hemispherical irradiance by the expression:

$$T_c^*(\varphi,\mathrm{z},\mathrm{t})=\mathrm{T}_c(\varphi,\mathrm{z},\mathrm{t})+\frac{\eta E(\varphi,\mathrm{z},\mathrm{t})}{\alpha}. \tag{29}$$

For excess temperature $\theta(\mathrm{r},\varphi,\mathrm{z},\mathrm{t})=\mathrm{T}(\mathrm{r},\varphi,\mathrm{z},\mathrm{t})-\mathrm{T}_c(\varphi,\mathrm{z},\mathrm{t})$ at $T_c(\varphi,\mathrm{z},\mathrm{t})=f(\mathrm{r},\varphi,\mathrm{z})$, taking into account (28) and (29), expression (27) will take the following form:

$$\begin{aligned}\theta(\mathrm{r},\varphi,\mathrm{z},t)=&\sum_{n=0}^{\infty}\sum_{m=0}^{\infty}\sum_{k=0}^{\infty}\frac{a}{\lambda}\{\int_0^t\int_0^{\pi}\int_{R_1}^{R_2}\mathrm{q}_\upsilon(\mathrm{r},\varphi,\mathrm{z},\tau)\,\mathrm{r}^2\,\Phi_n(\varphi)K_{2m}^{2n}(\mathrm{z})\,\mathrm{R}_{km}(\beta_{nm}\,\mathrm{r})\times\\&\times\mathrm{d}\varphi\,\mathrm{dzdr}+\eta R_2^2\,\mathrm{R}_{km}(\beta_{nm}\,\mathrm{R}_2)\int_0^1\int_0^{2\pi}\int_{R_1}^{R_2}\mathrm{E}_2(\varphi,\mathrm{z},\tau)r^2\Phi_n(\varphi)\,\mathrm{K}_{2m}^{2n}(\mathrm{z})\,\mathrm{R}_{km}(\beta_{nm}\,\mathrm{r})\times\\&\times\mathrm{d}\varphi\,\mathrm{dzdr}+\eta R_1^2\,\mathrm{R}_{km}(\beta_{nm}\,\mathrm{R}_2)\int_0^1\int_0^{2\pi}\int_{R_1}^{R_2}\mathrm{E}_1(\varphi,\mathrm{z},\tau)r^2\Phi_n(\varphi)\,\mathrm{K}_{2m}^{2n}(\mathrm{z})\,\mathrm{R}_{km}(\beta_{km}\,\mathrm{r})\times\\&\mathrm{d}\varphi\,\mathrm{dzdr}]\exp[\,-\mathrm{a}\,\beta_{km}^2(\mathrm{t}-\tau)]\,\mathrm{d}\tau\}\Phi_n(\varphi)\,\mathrm{K}_{2m}^{2n}(\mathrm{z})\,\mathrm{R}_{km}(\beta_{nm}\,\mathrm{r})\end{aligned} \tag{30}$$

where $E_1(\varphi,\mathrm{z},\mathrm{t})$ and $E_2(\varphi,\mathrm{z},\mathrm{t})$ - local hemispherical irradiances of concave and convex surfaces of the spherical zone.

Expression (30) is applicable for both convex and concave sensing elements. In this case, one of the terms containing $E_1(\varphi,\mathrm{z},\mathrm{t})$ or $E_2(\varphi,\mathrm{z},\mathrm{t})$ will be zero.

To obtain an expression that can be used in solving practical problems, we restrict ourselves to the first term of the series in expression (30), i.e. we set $n = m = k = 0$. Then the kernels of the corresponding integral transformations will take the following form based on expressions (17)-(19):

$$\Phi_0(\varphi) = \frac{1}{\sqrt{\pi}} \tag{31}$$

$$R_{20}^{20}(z) = \sqrt{\frac{1}{2}} \tag{32}$$

$$R_{00}(\beta_{00}\,\mathrm{r}) = \frac{1}{r}\sqrt{\frac{2}{\pi\beta_{00}}}(\mathrm{c}_{10}\sin\beta_{00}\,\mathrm{r} - \mathrm{c}_{20}\cos\beta_{00}\,\mathrm{r}) \tag{33}$$

The expression (31) in this case after the transition from $zk\mu$ in accordance with the formula (7*) can be written separately for heating with electric current and radiation:

$$\theta_э(\mathrm{r},\mathrm{t}) = \frac{a(\mathrm{c}_{10}\sin\beta_{00}\,\mathrm{r} - \mathrm{c}_{20}\sin\beta_{00}\,\mathrm{r})}{\lambda\pi^2\beta_{00}\,\mathrm{r}(\mu_1-\mu_2)}\int_0^t \exp\left[-a\beta_{00}^2(\mathrm{t}-\tau)\right]\times \int_0^{2\pi}\int_{\mu_1}^{\mu_2}\int_{R_1}^{R_2} q_\upsilon(\mathrm{r},\varphi,\mu,\tau)\,\mathrm{r}(\mathrm{c}_{10}\sin\beta_{00}\,\mathrm{r} - \mathrm{c}_{20}\cos\beta_{00}\,\mathrm{r})\,\mathrm{d}\varphi d\mu d\tau \tag{34}$$

$$\theta_{n1}(\mathrm{r},\mathrm{t}) = \frac{\sqrt{2}\eta R_1(\mathrm{c}_{10}\sin\beta_{00}R_1 - \mathrm{c}_{20}\cos\beta_{00}\,\mathrm{R}_1)(\mathrm{c}_{10}\sin\beta_{00}\,\mathrm{r} - \mathrm{c}_{20}\cos\beta_{00}\,\mathrm{r})}{\lambda\pi^{5/2}\beta_{00}^{3/2}r(\mu_2-\mu_1)}\times \times\int_0^t \exp\left[-a\beta_{00}^2(\mathrm{t}-\tau)\right]\int_0^{2\pi}\int_{\mu_1}^{\mu_2}\int_{R_1}^{R_2} E_1(\varphi,\mu,\tau)\,\mathrm{r}(\mathrm{c}_{10}\sin\beta_{00}\,\mathrm{r} - \mathrm{c}_{20}\cos\beta_{00}\,\mathrm{r})\,\mathrm{d}\varphi d\mu drd\tau \tag{35}$$

$$\theta_{n2}(\mathrm{r},\mathrm{t}) = \frac{\sqrt{2}\eta_a R_2(\mathrm{c}_{10}\sin\beta_{00}R_2 - \mathrm{c}_{20}\cos\beta_{00}\,\mathrm{R}_2)(\mathrm{c}_{10}\sin\beta_{00}\,\mathrm{r} - \mathrm{c}_{20}\cos\beta_{00}\,\mathrm{r})}{\lambda\pi^{5/2}\beta_{00}^{3/2}r(\mu_2-\mu_1)}\times \times\int_0^t \exp\left[-a\beta_{00}^2(\mathrm{t}-\tau)\right]\int_0^{2\pi}\int_{\mu_1}^{\mu_2}\int_{R_1}^{R_2} E_{12}(\varphi,\mu,\tau)\,\mathrm{r}(\mathrm{c}_{10}\sin\beta_{00}\,\mathrm{r} - \mathrm{c}_{20}\cos\beta_{00}\,\mathrm{r})\,\mathrm{d}\varphi d\mu drd\tau \tag{36}$$

where $Q_{n1}(\mathrm{r},\mathrm{t})$ and $Q_{n2}(\mathrm{r},\mathrm{t})$ — excessive temperatures of the sensing element in the form of a spherical zone during irradiation of concave and convex surfaces.

Thus, in the first approximation, consideration of a complex model of a multilayer sensor element of the receiver can be replaced by consideration of a simpler model of a homogeneous sensor element of the appropriate shape. This simplification makes it possible to obtain working formulas for determining the energy parameters of radiation from considering the temperature field of the sensing element.

Conclusion

The solution of the thermal conductivity equation describing the temperature field of the sensing element in the form of a hemisphere and a spherical zone, due to the nonequivalence of heat losses during irradiation and calibration by electric current, is obtained. Taking into account this systematic error makes it possible to increase the accuracy of measuring the energy parameters of radiation. These solutions of the equations formed the basis of the designs of devices for measuring heat flow.

The developed heat flow device of a given shape allows you to pinpoint and diagnose in advance the condition of pipes of heating networks, search for places of coolant leakage, without opening pipelines and stopping their operation.

References

1 Геращенко О.А. Основы теплометрии / О.А. Геращенко. — Киев: Наук. думка, 1984. — 192 с.

2 Геращенко О.А. Температурные измерения / О.А. Геращенко, А.Н. Гордов, А.К. Еремина и др. — Киев: Наук. думка, 1989. — 412 с.

3 Vankov Y. Hydraulic Modes of Heat Supply Systems Under Weather Control by Automated Individual Heat Points Lecture Notes in Electrical Engineering this link is disabled / Y. Vankov, E. Izmaylova, S. Gilfanov // 729 LNEE. — 2021. — C. 293–305.

4 Ewing J. A direct-measurement thin-film heat flux sensor array / J. Ewing, A. Gifford, D. Hubble, P. Vlachos, A. Wicks // Measurement Science and Technology. — 2010. — № 21. — P. 26-32. DOI:10.1088/0957-0233/21/10/105201

5 Blackwell B. A technique for uncertainty analysis for inverse heat conduction problems / B. Blackwell, J.V. Beck // Int. J. Heat Mass Transfer. — 2010. — Vol. 53. — P. 753-759.

6 Atherton J.J. Thermal characterization of μL volumes using a thin film thermocouple based sensor / J.J. Atherton, M.C. Rosamond, S. Johnstone, D.A. Zeze // Sensors and actuators A: Physical. — 2011. — Vol. 166/1. — P. 34-39.

7 Saidi A. Heat flux sensor with minimal impact on boundary conditions / A. Saidi, J. Kim // Experimental Thermal and Fluid Science. — 2004. — № 28. — P. 903-908.

8 Nussupbekov B.R. Heat flow meter / B.R. Nussupbekov, D.Zh. Karabekova, A.K. Khassennov, U.B. Nussupbekov, O.B. Aukeev // Patent of the RK. — 2017. — № 1588.

9 Karabekova D.Zh. Analysis of the Insulation State of Underground Pipelines in the Heating Network / D.Zh. Karabekova, P.A. Kissabekova, B.R. Nussupbekov, A.K. Khassenov // Thermal Engineering. — 2021. — № 68(10). — P. 802–805.

10 Karabekova D.Zh. A device for measuring heat flow / D.Zh. Karabekova, P.A. Kissabekova, A.K. Khassenov, Sh. Azatbek // Patent of the RK. — 2021. — № 6393.

11 Kuritnyk I.P. Theoretical foundations of the operation of heat flow meters for the diagnosis of technological processes / I.P. Kuritnyk, B.R. Nussupbekov, D.Zh. Karabekova, A.K. Khassennov // Bulletin of the University of Karaganda-Physics. — 2017. — № 1(85). — P. 55-59.

12 Nussupbekov B.R. Thermal Methods and Non-Destructive Testing Instrumentation / B.R. Nussupbekov, D.Zh. Karabekova, A.K. Khassennov // Measurement Techniques. — 2016. — Vol. 59. — № 6. — P. 644–648.

П.А. Кисабекова, Д.Ж. Карабекова, А.К. Хасенов, В.Ю. Кучерук, А.С. Кудусов, Ш.С. Кыздарбекова

Жылу ағыны құрылғыларының жұмысын құрудың теориялық негіздері

Көптеген зерттеулер жылу желілері мен технологиялық объектілерді техникалық диагностикалаудың барлық талаптарын бұзбайтын бақылау әдістері қанағаттандыратынын көрсетеді. Бұзбайтын бақылау әдістері процестердің температуралық күйін бақылауға және автоматтандырылған тіркеуге негізделген. Әзірленген құрылғы жерасты құбырларының жылу оқшаулау күйін талдауға арналған. Жылу ағынын өлшеуге арналған аспаптарды әзірлеу және зерттеу сезімтал элементтің температура өрісін міндетті түрде қарастыруды талап етеді, яғни берілген шеттік жағдайларда белгілі бір пішіндегі дене үшін жылу өткізгіштіктің дифференциалдық теңдеуін шешуді талап етеді. Жалпы жағдайда сезімтал элементтер көп қабатты: қарамен жабылған жабын, калориметриялық жүктеме, термосезгіш элементтер, лак және желіммен қабатталған ауыспалы қабаттар. Яғни, сезімтал элементтер сәулеленген бетке перпендикуляр бағытта да, параллель бағытта да біртекті емес. Бірінші жағдайда біртекті еместігі сезімтал элементтің көпқабаттылығымен байланысты. Мақалада сәулелену және электр тогын калибрлеу кезінде жылу шығынының эквиваленттілігіне байланысты жарты шар және шар аймағы түріндегі сезімтал элементтің температура өрісін сипаттайтын жылу өткізгіштік теңдеуінің шешімдері сипатталған. Осы жүйелі қателікті есепке алу сәулеленудің энергетикалық параметрлерін өлшеу дәлдігін арттыруға мүмкіндік береді. Теңдеулердің бұл шешімдері жылу ағынын өлшеуге арналған құралдың құрылымына негіз болды.

Кілт сөздер: жылу ағыны, жылу ағынын өлшеуге арналған құрылғы, сезімтал элемент, сезімтал элементтің температура өрісі.

П.А. Кисабекова, Д.Ж. Карабекова, А.К. Хасенов, В.Ю. Кучерук,
А.С. Кудусов, Ш.С. Кыздарбекова

Теоретические основы построения работы приборов теплового потока

Многочисленные исследования показывают, что наиболее всем требованиям технической диагностики тепловых сетей и технологических объектов удовлетворяют методы неразрушающего контроля. Методы неразрушающего контроля основаны на наблюдении и автоматизированной регистрации за температурным состоянием процессов. Разработанный прибор предназначен для анализа состояния тепловой изоляции подземных трубопроводов. Разработка и исследование приборов для измерения теплового потока требуют обязательного рассмотрения температурного поля чувствительного элемента, то есть решения дифференциального уравнения теплопроводности для тела определенной формы при заданных краевых условиях. В общем случае чувствительные элементы многослойны: черное покрытие, калориметрическая нагрузка, термочувствительные элементы, чередующиеся лаковые и клеевые прослойки. То есть чувствительные элементы неоднородны, как в направлении, перпендикулярном облучаемой поверхности, так и в параллельном. Неоднородность в первом случае обусловлена многослойностью чувствительного элемента. В статье описано решение уравнения теплопроводности, описывающее температурное поле чувствительного элемента в форме полусферы и шаровой зоны, обусловленное неэквивалентностью тепловых потерь при облучении и калибровке электрическим током. Учёт данной систематической погрешности позволяет повысить точность измерения энергетических параметров излучения. Данные решения уравнения легли в основу конструкций прибора для измерения теплового потока.

Ключевые слова: тепловой поток, прибор для измерения теплового потока, чувствительный элемент, температурное поле чувствительного элемента.

References

1 Gerashchenko, O.A. (1984). Osnovy teplometrii [Fundamentals of thermometry]. Kiev: Naukova Dumka [in Russian].

2 Gerashchenko, O.A., Gordov, A.N., & Eremina, A.K. (1989). Temperaturnye izmereniia [Temperature measurements]. Kiev: Naukova Dumka [in Russian].

3 Vankov, Y., Izmaylova, E., & Gilfanov, S. (2021). Hydraulic Modes of Heat Supply Systems Under Weather Control by Automated Individual Heat Points Lecture Notes in Electrical Engineering this link is disabled. *729 LNEE*, 293–305.

4 Ewing, J., Gifford, A., Hubble, D., Vlachos, P., & Wicks, A. (2010). A direct-measurement thin-film heat flux sensor array. *Measurement Science and Technology, 21*, 26-32. DOI:10.1088/0957-0233/21/10/105201

5 Blackwell, B., & Beck, J.V. (2010). A technique for uncertainty analysis for inverse heat conduction problems. *Int. J. Heat Mass Transfer, 53*, 753-759.

6 Atherton, J.J., Rosamond, M.C., Johnstone, S., & Zeze, D.A. (2011). Thermal characterization of μL volumes using a thin film thermocouple based sensor. *Sensors and actuators A: Physical, 166/1*, 34-39.

7 Saidi, A., & Kim, J. (2004). Heat flux sensor with minimal impact on boundary conditions. *Experimental Thermal and Fluid Science, 28*, 903-908.

8 Nussupbekov, B.R., Karabekova, D.Zh., Khassennov, A.K., Nussupbekov, U.B., & Aukeev, O.B. (2017). Heat flow meter. *Patent of the RK № 1588*.

9 Karabekova, D.Zh., Kissabekova, P.A., Nussupbekov, B.R., & Khassenov, A.K. (2021). Analysis of the Insulation State of Underground Pipelines in the Heating Network. *Thermal Engineering, 68(10)*, 802–805.

10 Karabekova, D.Zh., Kissabekova, P.A., Khassenov, A.K., & Azatbek Sh. (2021). A device for measuring heat flow. *Patent of the RK № 6393*.

11 Kuritnyk, I.P., Nussupbekov, B.R., Karabekova, D.Zh., & Khassennov, A.K. (2017). Theoretical foundations of the operation of heat flow meters for the diagnosis of technological processes. *Bulletin of the University of Karaganda-Physics, 1(85)*, 55-59.

12 Nussupbekov, B.R., Karabekova, D.Zh., & Khassennov, A.K. (2016). Thermal Methods and Non-Destructive Testing Instrumentation. *Measurement Techniques, 59(6)*, 644–648.

АВТОРЛАР ТУРАЛЫ МӘЛІМЕТТЕР
СВЕДЕНИЯ ОБ АВТОРАХ
INFORMATION ABOUT AUTHORS

Abakumov, Kh.Kh. — PhD student, National Research Tomsk Polytechnic University, Tomsk, Russia, hha1@tpu.ru.

Aimukhanov, A. — Candidate of Physical and Mathematical Sciences, Associate professor, Professor of the Department of Radiophysics and Electronics, Leading Researcher, Karaganda University of the name of academician E.A. Buketov, Scientific Center for Nanotechnology and Functional Nanomaterials, Karaganda, Kazakhstan; e-mail: a_k_aitbek@mail.ru

Alexeev, A. — Candidate of Physical and Mathematical Sciences, Leading Researcher of Kazan Federal University, Kazan, Russia; e-mail: alalrus@gmail.ru

Alikhaidarova, E. — Junior Research Fellow, Institute of Molecular Nanophotonics, Karaganda University of the name of academician E.A. Buketov, Kazakhstan.

Belov, S.M. — Candidate of Physical and Mathematical Sciences, Al-Farabi Kazakh National University, Almaty, Kazakhstan.

Botpaev, N.K. — Engineer of Karaganda University of the name of academician E.A. Buketov, Kazakhstan

Fedorenko, O.V. — Candidate of Physical and Mathematical Sciences, Al-Farabi Kazakh National University, Almaty, Kazakhstan; e-mail: fedor23.04@mail.ru.

Goldsteyn, A.E. (contact person) — Doctor of Technical Sciences, Professor, National Research Tomsk Polytechnic University, Tomsk, Russia, algol@tpu.ru.

Gribov, M.L. — Doctor of Law, Professor, Professor of the Department of Investigative Activities of the National Academy of Internal Affairs, Ukraine, e-mail: griboff007@gmail.com

Ibrayev, N. — Doctor of Physics and Mathematical Sciences, Professor, Director of the Institute of Molecular Nanophotonics, Karaganda University of the name of academician E.A. Buketov, Kazakhstan.

Ilyassov, B. — PhD, Associate professor of Department of Intelligent Systems and Cyber Security, Astana IT University, Kazakhstan; e-mail: baurdinho@mail.ru

Jaichichekov, N. Zh. (contact person) — Doctor of Physical and Mathematical sciences, Professor, Gumilyov Eurasian National University, Astana, Kazakhstan; e-mail:jaich@mail.ru

Karabekova, D.Zh. — PhD, Associate professor, Karaganda University of the name of academician E.A. Buketov, Kazakhstan, e-mail: karabekova71@mail.ru

Karpenko, A.G. — Candidate of Physical and Mathematical sciences, Associate professor, Saint-Peterburg State University, St. Petersburg, Russia; e-mail: aspera.2003.ru@mail.ru

Kassiyev, S.B. — 1 st year Master student of Karaganda University of the name of academician E.A. Buketov, Kazakhstan, e-mail: kassiyev_s@mail.ru

Katsyv, S.S. — Candidate of Technical Sciences, Associate professor, Associate professor of the Department of Computerized Electromechanical Systems and Complexes, Vinnitsa National Technical University, Ukraine, e-mail: katsyvsam@ukr.net

Khassenov, A.K. — PhD, Associate professor, Karaganda University of the name of academician E.A. Buketov, Kazakhstan, e-mail: ayanbergen@mail.ru

Kissabekova, P.A. — Master of Pedagogical Sciences, Karaganda University of the name of academician E.A. Buketov, Kazakhstan, e-mail: pika_1666@mail.ru

Kyzdarbekova, Sh.S. — Senior Lecturer of the Department of Engineering Thermal Physics named after Professor Zh.S. Akylbaev, e-mail: sholp.01@mail.ru

Kossov, V.N. (contact person) — Doctor of Physical and Mathematical Sciences, Professor, Corresponding member of the National Academy of Sciences of the Republic of Kazakhstan, Academician of the National Academy of Sciences of the High School of RK, Head of the Physics Department, Abai Kazakh National Pedagogical University, Almaty, Kazakhstan; e-mail: kosov_vlad_nik@list.ru.

Krasikov, S.A. – Candidate of Technical Sciences, Leading Research Scientist, Abai Kazakh National Pedagogical University, Almaty, Kazakhstan; e-mail: sa.krassikov@mail.ru.

Kucheruk, V.Y. — Doctor of Technical Sciences, Professor, Professor of the Department of Information Technologies of the Uman National University of Horticulture, Professor of the Department of Computer Science and Economic Cybernetics of the Vinnitsa National Agrarian University, Ukraine, e-mail: vladimir.kucheruk@gmail.com

Kudussov, A.S. — Associate professor, Candidate of Physical and Mathematical Sciences, Karaganda University of the name of academician E.A. Buketov, Kazakhstan, e-mail: akudusov@mail.ru

Kukharchuk, V.V. (contact person) — Doctor of Technical Sciences, Professor, Professor of the Department of Computerized Electromechanical Systems and Complexes, Vinnitsa National Technical University, Ukraine, e-mail: BKuch@ukr.net

Kulakov, P.I. — Doctor of Technical Sciences, Professor, Professor of the Department of Information Technologies of the Uman National University of Horticulture, Ukraine, e-mail: kulakovpi@gmail.com

Kurmanova, D.Y. — 3rd-year doctoral student, Gumilyov Eurasian National University, Astana, Kazakhstan; e-mail: dikonya89_29@mail.ru

Minkov, L.L. — Doctor of Physical and Mathematical Sciences, Professor of the National Research Tomsk State University, Tomsk, Russia

Nurkenov, S.A. — Candidate of Physical and Mathematical Sciences, Associate professor of the Department of Technical Physics, Eurasian National University named after L.N. Gumilyov, Astana International University, Astana, Kazakhstan.

Rozhkova, X. (contact person) — Master of Technical Science, Lecturer of the Department of Radiophysics and Electronics, Researcher, Karaganda University of the name of academician E.A. Buketov, Scientific Center for Nanotechnology and Functional Nanomaterials, Karaganda, Kazakhstan; e-mail: ksusharogovaya@mail.ru.

Seliverstova, E. — Senior Research Fellow, PhD, Institute of Molecular Nanophotonics, Karaganda University of the name of academician E.A. Buketov, Kazakhstan.

Shaimerdenova, K.M. — Professor of Karaganda University of the name of academician E.A. Buketov, Kazakhstan.

Suierkulova, Zh.N. — Doctoral student of the specialty “6D072300-Technical Physics”, Eurasian National University named after L.N. Gumilyov, Astana, Kazakhstan.

Tanasheva, N.K. — PhD, Associate professor of Karaganda University of the name of academician E.A. Buketov, Kazakhstan.

Tleubergenova A.Zh. (contact person) — PhD 2 nd year doctoral student of Karaganda University of the name of academician E.A. Buketov, Kazakhstan, e-mail: shymkent.a7@mail.ru.

Tleukenov S.K. — The main author, Doctor of Physical and Mathematical Sciences, Professor of the Department of Technical Physics, Eurasian National University named after L.N. Gumilyov, Astana, Kazakhstan.

Tussupvekova A. — PhD, Associate professor of the Department of Radiophysics and Electronics, Karaganda University of the name of academician E.A. Buketov, Kazakhstan; e-mail: aintus@mail.ru.

Volkov, K.N. — Doctor of Physical and Mathematical sciences, Senior Lecturer, Kingstone University, London, Great Britain; e-mail:dsci@mail.ru.

Zeinidenov, A. — PhD, Associate professor, Dean of the Physics and Technology Faculty, Head of Scientific Center for Nanotechnology and Functional Nanomaterials, Karaganda University of the name of academician E.A. Buketov, Karaganda, Kazakhstan; e-mail: asyl-zeinidenov@mail.ru.

Zhakanova, A. — Master of Technical science, Junior Researcher of Scientific Center for Nanotechnology and Functional Nanomaterials, Karaganda University of the name of academician E.A. Buketov, Kazakhstan; e-mail: zhakanova0@mail.ru

Zhaneli, M. — PhD student, Abai Kazakh National Pedagogical University, Almaty, Kazakhstan.